

POLITÉCNICO DE LEIRIA

ESCOLA SUPERIOR DE TECNOLOGIA E GESTÃO

Automotive 4D Radar Imaging with 360° Field of View

Samuel Viegas Reigota de Jesus

Master dissertation performed under the guidance of
Prof. Dr. Rafael Ferreira da Silva Caldeirinha
and Dr. João Ricardo Vitorino Reis,
professors at Escola Superior de Tecnologia e Gestão,
Instituto Politécnico de Leiria

Leiria, November 21, 2024

Abstract

Radio Detection And Ranging (Radar) technology has been around for many decades. Initially developed for military purposes, radar technology has now grown into a larger set of applications. It is used in aviation, to detect other aircrafts and give accurate altitude readings, in marine navigation, to prevent collision with other ships and monitor ship movements in busy waters, in weather forecast, to monitor precipitation and wind, in factories, to enable manufacturing robots to perceive their environment and navigate/position themselves according to it, and even in health care, to monitor breathing and blood pressure, to name a few. In recent years, improvements in integrated circuitry and Radio Frequency (RF) electronics have made radar-on-chip possible, significantly reducing production costs and therefore enabling a wider adoption of radar technology, now commonly used in many civil applications. In the automotive industry for instance, Millimeter Wave (mmWave) radar sensors are being implemented in everyday vehicles for purposes such as Collision Warning System (CWS), Blind Spot Detection (BSD), Autonomous Cruise Control (ACC), Parking Assistance Systems (PAS) and many more, thus being integrated in systems such as Advanced Driver Assistance Systems (ADAS) and Autonomous Driving Systems (ADS). These systems comprise a suite of electronic automotive technologies designed to assist drivers in various driving scenarios, enhance safety, and improve the overall driving experience by providing real-time data through a combination of software algorithms and sensors, including cameras, ultrasonic sensors, Light Detection And Ranging (Lidar) and radar. Using real-time data from each component, ADAS and ADS can perceive the environment, plan a response, and control the vehicle's mechanical systems to execute the intended action. As the market pushes for higher levels of vehicle autonomy, both ADAS and ADS are becoming increasingly more complex and sophisticated, requiring improvements in radar technology to meet the evolving demands of these advanced systems.

Therefore, this dissertation presents the work on the development of a 4 Dimensions (4D) Multiple-Input-Multiple-Output (MIMO) automotive imaging radar with a 360° Field-of-View (FoV). After a brief description of the proposed architecture, using three mmWave 4D imaging radar sensors (AWR1843BOOST) by Texas Instruments (TI), disposed in a equilateral triangular prism shape, this dissertation presents the first results on the implementation of a real-time and high resolution radar sensor with a 360° FoV. To conclude the performance evaluation of the presented 360° radar, experimental results obtained in a controlled environment, i.e. inside an anechoic chamber, are presented to validate the proposed concept. A mmWave Compact Antenna Test Range (CATR) anechoic chamber was also designed and built in order to properly calibrate the radar. Successful target detection is achieved by multi-point point-cloud. The proposed radar architecture may be seen as an opportunity to augment and improve ADAS and ADS.

Keywords: 4D imaging radar, mmWave, ADAS, ADS, automotive, field-of-view, mapping, anechoic chamber.

Resumo

A tecnologia radar existe há várias décadas. Inicialmente desenvolvida para fins militares, a tecnologia radar expandiu-se para um vasto conjunto de aplicações. É utilizado na aviação, para a deteção de outras aeronaves e realizar medições de altitude com precisão, na náutica, para prevenção contra a colisão com outras embarcações e monitorizar a movimentação de embarcações em zonas de muito movimento, na meteorologia, para monitorização da precipitação e ventos, em fábricas, para que robôs de produção possam compreender o ambiente em seu redor e movimentar/posicionar-se de acordo com o mesmo, e até mesmo na área da saúde, para medir a tensão arterial e a respiração, entre outras. Recentemente, avanços nos circuitos integrados e eletrónica RF tornaram possível o radar-on-chip, que por sua vez tornou os custos de produção mais baixos, permitindo assim que a tecnologia radar se expandisse ainda mais, sendo agora utilizada em várias aplicações de uso civil. Na indústria automóvel por exemplo, sensores radar de onda milimétrica (mmWave) estão a ser implementados em veículos de uso diário para aplicações como aviso de colisão (CWS), deteção em zonas de sombra (BSD), controlo de cruzeiro adaptativo (ACC), assistência ao estacionamento (PAS), entre outros, sendo assim integrado em sistemas avançados de assistência ao condutor (ADAS) e de condução autónoma (ADS). Estes sistemas abrangem um conjunto de tecnologias para aplicações automóvel projetadas com o intuito de dar assistência aos condutores em vários cenários de condução, aumentar a segurança e melhorar a experiência de condução, ao fornecer dados em tempo real através da combinação de algoritmos e do uso de sensores, tais como câmeras, sensores ultrasons, lidar e radar. Ao utilizar esses dados em tempo real, os sistemas ADAS e ADS conseguem ter uma perceção do ambiente, planear uma resposta e controlar os sistemas mecânicos do veículo para executar a ação pretendida. Com a pressão do mercado para aumentar o nível de autonomia dos veículos, os sistemas ADAS e ADS estão a tornar-se mais complexos e sofisticados, o que significa que a tecnologia radar tem de ser aperfeiçoada para satisfazer as exigências desses sistemas.

Para esse fim, esta dissertação apresenta um radar MIMO 4D para aplicações automóvel com um campo de visão de 360°. Após uma breve descrição da arquitetura proposta, onde são utilizados 3 radares de onda milimétrica (AWR1843BOOST) da TI, dispostos numa estrutura triangular equilateral, esta dissertação apresenta os primeiros resultados da implementação de um sensor radar de alta resolução em tempo real com um campo de visão de 360°. Para concluir a avaliação do desempenho do radar 360°, resultados experimentais obtidos em ambiente controlado, numa câmara anecoica, são apresentados de forma a validar o conceito proposto. Uma câmara anecoica compacta (CATR) para ondas milimétricas foi também projetada e construída de forma a calibrar o radar. A deteção de alvos é bem sucedida e é visualizada através de uma núvem de multi pontos. A arquitetura de radar proposta pode ser vista como uma oportunidade para melhorar os sistemas ADAS e ADS.

Acknowledgement

First and foremost, I would like to thank Escola Superior de Tecnologia e Gestão from Instituto Politécnico de Leiria (ESTG-IPL) and Instituto de Telecomunicações - Delegação de Leiria (IT-Leiria) for providing the facilities, equipment and tools that were essential for the development of this work. I would also like to thank PAC - Portugal Autocluster for the Future, INOV.AM and ESTG-IPL for the research grant and for funding this project.

I would like to thank my advisors, Professor Rafael Caldeirinha and Professor João Reis, for all of their help and disposition and for guiding me throughout this work. Also, to all of the members of the Antennas and Propagation research group at Instituto de Telecomunicações - Delegação de Leiria, for providing a healthy work environment and for assisting me whenever I needed.

A special thanks to my parents, grandparents and brother for all of their help and support throughout my academic life, and for being there when I needed the most. Also, to my girlfriend, who always had something nice to say on those rough days of writing and for keeping me focused on the conclusion of this work.

Contents

List of Figures **xi**

List of Tables **xv**

Acronyms **xvii**

1 Introduction **1**
1.1 Motivation . . . 1
1.2 Objectives . . . 2
1.3 Document Structure . . . 2

2 Automotive Radar Systems **5**
2.1 History . . . 5
2.2 Frequency Bands and Types of Operation . . . 7
2.3 State-of-the-Art Market Solutions . . . 10
2.3.1 Radar-on-Chip . . . 10
2.3.2 TI TIDEP-01012 . . . 12
2.3.3 Continental ARS430 . . . 12
2.3.4 Continental ARS408 . . . 13
2.3.5 Smartmicro UMRR-11 Type 132 . . . 13
2.3.6 Smartmicro UMRR-96 Type 153 . . . 13
2.3.7 Ainstein mmWave O-79 . . . 14
2.3.8 Bosch Corner/Front/Front Premium . . . 14
2.3.9 Altos V1 . . . 14
2.4 Literature Review . . . 15

3 mmWave 4D Radar Developments **19**
3.1 FMCW Radar Fundamentals . . . 19
3.1.1 FMCW Radar . . . 19
3.1.2 Range Estimation . . . 21
3.1.3 Range Resolution . . . 22
3.1.4 Velocity Estimation . . . 24
3.1.5 Velocity Resolution . . . 27
3.1.6 Angle Estimation . . . 27
3.1.7 Angle Resolution . . . 28
3.2 AWR1843BOOST Evaluation Board . . . 29
3.2.1 MIMO Configuration . . . 30
3.2.2 Radar Configuration Principles . . . 32
3.2.3 Data Output Structure . . . 34
3.2.4 Radar Calibration . . . 34
3.3 360° Radar - Prototype . . . 37

3.4 Radar 360° - MATLAB Controlled Version . . . 42
3.5 Radar 360° - Dedicated Hardware Version . . . 46
3.6 Measurements and Results . . . 49
3.6.1 Validation Measurement in a Static Scenario . . . 49
3.6.2 Validation Measurement in a Dynamic Scenario . . . 52
3.6.3 Integration with ADAS . . . 57
3.7 Conclusions . . . 58

4 mmWave CATR Anechoic Chamber Design and Applications 59
4.1 Design Considerations . . . 59
4.1.1 Selection of the Absorber Material . . . 59
4.1.2 Anechoic Chamber Dimensions . . . 60
4.2 3D Modeling . . . 62
4.3 Prototype Building Process . . . 66
4.4 Linear Rail Motion Control . . . 72
4.5 Chamber Characterization . . . 76
4.5.1 1 to 20 GHz . . . 76
4.5.2 60 to 90 GHz . . . 86
4.6 Radar Applications and Measurements Results . . . 96
4.6.1 360° Radar Calibration . . . 96
4.6.2 Characterization of polymer properties for bumpers . . . 99
4.6.3 SAR Imaging . . . 100
4.7 Conclusions . . . 105

5 Conclusions and Future Work 107
5.1 Summary and Main Conclusions . . . 107
5.2 Future Work . . . 108
5.2.1 Radar . . . 108
5.2.2 Anechoic chamber . . . 108
5.3 Contribution to Literature . . . 108
5.4 Live Demonstrators . . . 108

Bibliography 111

A Radar Configuration Commands 117

List of Figures

2.1 Early automotive radar developments and in-vehicle tests during the 1970s. (*a*) 10 GHz radar system built by VDO. (*b*) 16 GHz radar system built by Standard Electric Lorenz. (*c*) 35 GHz radar system built by AEG-Telefunken. [Figures extracted from [15]] 6
2.2 24 GHz VORAD CWS radar system (highlighted in red) mounted on the front of a Greyhound bus. [Figure extracted from [15]] 6
2.3 ARS100 - The first commercial 76 GHz automotive radar sensor. 7
2.4 Frequency bands for automotive radar. [Figure extracted from [1]] 8
2.5 Automotive radar types of operation. [Figure extracted from [2]] 9
2.6 Radar positioning on the vehicle for 360° awareness. [Figure extracted from [3]] 9
2.7 Radar-on-chip used on the TI AWR1843BOOST. 10
2.8 AWR1843 RoC block diagram. 11
2.9 Radar development boards. 12
2.10 Typical automotive radar system. 12
2.11 RPDNet object detection. 16
2.12 Pedestrian detection and height estimation using particle filter. 17

3.1 Generic high-level block diagram of an FMCW radar. 20
3.2 Up-chirp signal spectrogram. 20
3.3 Up-chirp signal in time domain. 21
3.4 Beat frequency spectrogram. 21
3.5 Diagram scenario of multiple target detection. 22
3.6 Tx and Rx ideal signal representation on a multiple target scenario (considering stationary objects). 23
3.7 Resolution in the IF frequency spectrum. (*a*) 2 distinguished targets. (*b*) 2 targets at the limit detection threshold. (*c*) 2 targets viewed as one, with no distinction between the peaks. 23
3.8 Radar range resolution vs. available bandwidth. 24
3.9 2D FFT processing of a frame containing M chirps, where N samples are taken out each chirp. [Figure extracted from [41]] 26
3.10 AWR1843 antenna configuration diagram. 27
3.11 Angle resolution between two closely placed target objects at the same distance from the radar. 28
3.12 Angle resolution improves with increasing number of RX antennas. [extracted from [47]] 29
3.13 TI AWR1843BOOST evaluation board. 30
3.14 Radiation diagrams of the AWR1843BOOST antennas. 31
3.15 AWR1843BOOST antenna arrays. 31
3.16 Virtual antenna array concept. 31
3.17 Bosch FR5CPEC front radar antenna arrays. 32

3.18 Typical appearance of the commands in a TI mmWave radar configuration file. . . . 33
3.19 Chirp configuration specifications. . . . 33
3.20 Output data structure. . . . 35
3.21 Radar 360° first prototype. . . . 37
3.22 Radar 360° geometry. . . . 38
3.23 Radar 360° with the disassembled radome structure. . . . 39
3.24 Radar 360° with the fully assembled radome structure. . . . 40
3.25 Distance traveled in radome wall for different grazing angles. [Extracted from [59]] . . . 41
3.26 1st tab of the radar 360° MATLAB GUI. . . . 43
3.27 2nd tab of the radar 360° MATLAB GUI. . . . 44
3.28 3rd tab of the radar 360° MATLAB GUI. . . . 45
3.29 Radar 360° - Raspberry Pi version generic block diagram. . . . 46
3.30 Setup inside the anechoic chamber. . . . 49
3.31 3D perspective of the poles position inside the anechoic chamber. . . . 50
3.32 Top view of the poles position inside the anechoic chamber. . . . 50
3.33 3D perspective of the computed point-cloud scatter plots. . . . 51
3.34 Top view of the computed point-cloud scatter plots. . . . 52
3.35 3D perspective of the poles position inside the anechoic chamber. . . . 53
3.36 Top view of the poles position inside the anechoic chamber. . . . 53
3.37 Sequence of frames from a video showing the detection of both stationary and moving targets. . . . 54
3.37 Sequence of frames from a video showing the detection of both stationary and moving targets. (cont.) . . . 55
3.37 Sequence of frames from a video showing the detection of both stationary and moving targets. (cont.) . . . 56
3.37 Sequence of frames from a video showing the detection of both stationary and moving targets. (cont.) . . . 57
3.38 Autoware point-cloud plot. . . . 58

4.1 WAVASORB VHP absorbers typical reflectivity. . . . 60
4.2 WAVASORB absorbers. . . . 60
4.3 3D model of the wooden enclosure for the anechoic chamber. . . . 63
4.4 3D model of the splitted wooden enclosure for the anechoic chamber. . . . 64
4.5 F3D model of the anechoic chamber. . . . 64
4.6 Artwork 3D model of the anechoic chamber. . . . 65
4.7 Covering the enclosure with aluminium foil. . . . 66
4.8 Cuts and holes done on the enclosure. . . . 66
4.9 Covering the enclosure with RF foam absorbers. . . . 67
4.10 Anechoic chamber during the painting process. . . . 67
4.11 Anechoic chamber with the aluminium profiles in place. . . . 68
4.12 Linear rail actuators in place with the removable bottom. . . . 68
4.13 Assembled anechoic chamber on the trolley rack . . . 69
4.14 Control system schematics diagram. . . . 71
4.15 Control system PCB. . . . 71
4.16 Linear rail actuators control system. . . . 72
4.17 Diagram of the linear rails placed at the bottom of the anechoic chamber. . 73
4.18 SAR measurement setup with the external axis mounted on top of the y axis. 73

4.19 Flowchart of the implemented linear rail axis control system. 77
4.20 QRH0140 parameters. 78
4.21 Measurement setup for the 1 - 20 GHz characterization. 79
4.22 Setup diagram (top view). 79
4.23 QRH0140 antenna reflection coefficients 80
4.24 Transmission coefficients on both polarizations, with $|S_{31}|$ corresponding to the horizontal polarization and the $|S_{42}|$ corresponding to the vertical polarization. 81
4.25 Transmission coefficients on both polarizations, truncated from 5 to 20 GHz, with $|S_{31}|$ corresponding to the horizontal polarization and the $|S_{42}|$ corresponding to the vertical polarization. 82
4.26 $|S_{11}|$ in the distance domain. 83
4.27 $|S_{31}|$ in the distance domain. 84
4.28 $|S_{33}|$ in the distance domain. 85
4.29 Transmission coefficients over a frequency sweep at 1 m of separation between antennas. 86
4.30 Transmission coefficients on both polarizations over distance at various frequencies. 87
4.31 Measurement setup for the 60 - 90 GHz characterization. 88
4.32 Moving antenna system. 89
4.33 Setup diagram (top view). 89
4.34 MD249-AA and horn antenna reflection coefficients. 90
4.35 Transmission coefficients 90
4.36 Transmission coefficients - truncated phase response. 91
4.37 Transmission coefficients - phase response from 400 to 500 mm. 92
4.38 $|S_{11}|$ in the distance domain. 93
4.39 $|S_{21}|$ in the distance domain. 94
4.40 $|S_{22}|$ in the distance domain. 95
4.41 Transmission coefficients over a frequency sweep at 500 and 900 mm of separation between antennas. 96
4.42 Transmission coefficients over distance at various frequencies. 97
4.43 Setup for the 360º radar calibration. 98
4.44 Compensation coefficients obtained in the calibration measurement. 98
4.45 Radar support rig for the samples. 99
4.46 Setup for the radar characterization of polymer samples. 100
4.47 Range profiles of the reference and sample polymers. 101
4.48 Geometry of the SAR imaging configuration. 101
4.49 SAR imaging radar 3D data matrix. 102
4.50 SAR imaging setup. 103
4.51 SAR measurement sample and image reconstruction result. 103
4.52 SAR imaging setup using a 3D antenna positioner. 104
4.53 SAR image reconstruction. 104

List of Tables

2.1 Radar-on-Chip Solutions. 11

3.1 Parameter comparison between AWR1843BOOST and Bosch FR5CPEC. . 34
3.2 Chirp configuration parameters as configured using the file presented in Fig. 3.18. 36
3.3 Radar detection capabilities as configured using the file presented in Fig. 3.18. 36
3.4 *x,y* coordinates of the metallic poles *vs.* point-cloud centroids, (in meters). 52

4.1 Range bias from each radar (in meters). 99

Acronyms

3D 3 Dimensions.

4D 4 Dimensions.

ACC Autonomous Cruise Control.

ADAS Advanced Driver Assistance Systems.

ADC Analog-to-Digital Converter.

ADS Autonomous Driving Systems.

AoA Angle-of-Arrival.

BLE Bluetooth Low Energy.

BSD Blind Spot Detection.

CA Collision Avoidance.

CAN Controller Area Network.

CATR Compact Antenna Test Range.

COTS Commercially Off-the-Shelf.

CPU Central Processing Unit.

CWS Collision Warning System.

DC Direct Current.

DIP Dual In-line Package.

DSP Digital Signal Processor.

EB Emergency Braking.

ECC Electronic Communications Committee.

EIRP Equivalent Isotropic Radiated Power.

EM Electromagnetic.

ETSI European Telecommunications Standards Institute.

FCC Federal Communications Commission.

FFT Fast Fourier Transform.

FMCW Frequency Modulated Continuous Wave.

FoV Field-of-View.

GPIO General Purpose Input/Output.

GPU Graphics Processing Unit.

GUI Graphical User Interface.

I In-Phase.

I2C Inter-Integrated Circuit.

IF Intermediate Frequency.

IFFT Inverse Fast Fourier Transform.

IoT Internet of Things.

IR Infrared Radiation.

ISM Industrial, Scientific and Medical.

ITU International Telecommunication Union.

LCA Lane Change Assist.

Lidar Light Detection And Ranging.

LNA Low Noise Amplifier.

LPF Low Pass Filter.

LRR Long Range Radar.

LSB Least Significant Bit.

LVDS Low-Voltage Differential Signaling.

MIMO Multiple-Input-Multiple-Output.

MMIC Monolithic Microwave Integrated Circuits.

mmWave Millimeter Wave.

MRR Medium Range Radar.

MSB Most Significant Bit.

NB Narrow Band.

OEM Original Equipment Manufacturer.

OS Operating System.

PA Power Amplifier.

PAS Parking Assistance Systems.

PCB Printed Circuit Board.

PETG Polyethylene Terephthalate Glycol.

PLA Polylactic Acid.

PLL Phase-Lock-Loop.

PVC Polyvinyl Chloride.

Q Quadrature.

Radar Radio Detection And Ranging.

RAM Random Access Memory.

RCS Radar Cross Section.

RCW Rear Collision Warning.

RF Radio Frequency.

RISC Reduced Instruction Set Computer.

RoC Radar-on-Chip.

ROS Robot Operating System.

RX Receive.

SDK Software Development Kit.

SNR Signal-to-Noise Ratio.

SoC System-on-Chip.

SPI Serial Peripheral Interface.

SRR Short Range Radar.

TI Texas Instruments.

TLV Type-Length-Value.

TX Transmit.

UART Universal Asynchronous Receiver-Transmitter.

UAV Unmanned Aerial Vehicles.

UDP User Datagram Protocol.

USART Universal Synchronous and Asynchronous Receiver-Transmitter.

USB Universal Serial Bus.

USRR Ultra Short Range Radar.

UWB Ultra Wide Band.

VAA Virtual Antenna Array.

VCO Voltage Controlled Oscillator.

VNA Vector Network Analyzer.

VSWR Voltage Standing Wave Ratio.

Chapter 1

Introduction

1.1 Motivation

The main motivation behind this work is to improve the current radar systems used by ADAS and ADS in vehicles, to help reducing road traffic crashes and fatalities. According to a 2018 World Health Organization (WHO) report [1], approximately 1.35 million people die each year as a result of road traffic crashes, and between 20 to 50 million suffered non-fatal injuries. Since about 90% of road traffic crashes are directly related to human failure [2], the implementation of ADAS and/or ADS in vehicles is crucial to mitigate those fatalities and enhance vehicle technology for safety and better driving. An IDTechEx research report [3] shows that, on average, 70% of the new cars produced in 2022 had a front radar and 30% had side radars, showing a steady and continued growth in the next years. This means that the automotive industry is committed on improving the safety of the passengers and mitigate traffic accidents and fatalities.

The ADAS is a system that assists drivers in driving and parking functions, whereas ADS is a system where the vehicle is capable of fully operate without human involvement. ADAS exploits superior knowledge of the surrounding environment thanks to advanced sensors, such as cameras, lidar and radar, and it is composed of both an hardware layer for sensing, and a software layer for post processing and decision making [4]. Sensing the surrounding environment, and communicating with it, are the key challenges of the automotive industry, which is now enhancing its ADAS towards ADS [4]. Progress towards fully autonomous driving has been slow and the vehicles currently on the market only incorporate ADAS.

The architecture of an autonomous vehicle consists of several modules such as, environment perception, decision making, path planning and control [5], with environment perception being the most critical. The sensors used in environment perception typically consist of cameras, lidars and mmWave radars. It is indisputable that cameras and lidars fail to varying degrees in adverse weather conditions such as rain, snow, fog, bright light and darkness, while the mmWave radar is indispensable as it shows strong robustness under bad weather conditions[6]. When an Electromagnetic (EM) wave propagates through the atmosphere, it is absorbed by atmospheric gases such as H_2O, CO_2, O_2 and O_3, and scattered and absorbed by atmospheric aerosols, such as haze, fog, clouds and rain [7]. Despite the fact that these weather conditions are complex, the main conclusions drawn from the study in [7] are: Haze is transparent to Radio Frequency (RF) radiation and attenuates visible radiation more than Infrared Radiation (IR); Clouds are opaque to visible and IR, but are almost transparent to RF radiation; Fogs are opaque to visible and IR radiation, except for small-drop fogs where most of the IR radiation may get through, and are almost transparent to RF radiation; Rains heavier than 10 mm/hour make the visible and IR sensors useless, while the

RF radiation propagates with attenuation ranging from 3 dB/km to 60 dB/km, depending on the frequency of the signal and on the severity of the rain. In the following papers [8–11], the effects of adverse weather conditions on the most used automotive sensors, such as cameras, lidars and radars, are presented and reviewed. In [11] a detailed comparative table between sensors is presented, with the radar being the least affected sensor by the adverse weather conditions.

4D imaging radar emerged as a solution to cope with the drawbacks of the more conventional radars, not only providing 3D spatial information about the target objects but also providing velocity estimation, which creates a time-based motion analysis that allows for object tracking in dynamic environments, through processing algorithms. By exploiting the use of a large number of antennas, 4D imaging radar improves the accuracy of angle estimation and enhances the angle resolution, which ultimately results in high resolution information about the target objects. Therefore, 4D imaging radar is a great solution to tackle the challenge of autonomous driving, since there are no optics involved the 4D radar is robust in all lighting and adverse weather conditions, yielding a high resolution mapping of the surroundings. Since vehicles move in challenging traffic situations, in environments where the hazards are constant and dangerous situations appear almost as if out of nowhere, these radar sensors need to be implemented all around the vehicle, to ensure a reliable all-round monitoring of the vehicle's surroundings, thus forming a 360° environmental detection. To this end, the proposed radar architecture is sought to improve the radar state-of-the-art by making possible to create a 4D 360° high-resolution multi-point point-cloud of its surroundings, which shall augment and improve ADAS and/or ADS.

1.2 Objectives

In this dissertation, a 4D imaging radar prototype with 360° Field-of-View (FoV) is presented. Furthermore, a real case scenario is tested in order to validate the proposed prototype as capable of improving ADAS or ADS systems. A Compact Antenna Test Range (CATR) anechoic chamber for mmWave measurements is designed and built in order to carry out radar measurements and calibrations. Lastly, a EM characterization of said chamber is done for automotive frequency bands. The main objectives of this work are described as following:

- Develop a 4D imaging radar prototype with 360° of FoV;
- Develop a real case measurement scenario;
- Design and build a CATR anechoic chamber for mmWave measurements;
- EM characterization of the CATR anechoic chamber in the automotive frequency bands;
- Perform radar measurements inside the CATR anechoic chamber.

1.3 Document Structure

The document is organized as follows. In Chapter 2 the history of automotive radar is briefly presented, following the state-of-the-art on 4D mmWave radars, and finally presents a literature review on some of the latest work regarding mmWave radars. Chapter 3 presents an overview on some basic concepts regarding the mmWave radar working principles, radar configuration using a single mmWave radar and finally the proposed radar system, as well

as its validation results. In Chapter 4 it is presented the design, construction process and first validation measurements of a compact mmWave anechoic chamber that was built in order to test mmWave radio systems, such as radars. Finally in Chapter 5 a summary of the work done in this dissertation is made, the main conclusions are drawn and the future work is discussed.

Chapter 2

Automotive Radar Systems

This chapter addresses the automotive radar technology. Firstly, in section 2.1, it is presented the history and early developments on automotive radar technology. Section 2.2 presents the frequency bands used by automotive radars as well as their types of operation. Section 2.3 outlines the market solutions supplied by the leading integrated circuit manufacturers, such as, Infineon, STMicroelectronics, TI and NXP. These solutions are widely available in the market, mainly in SoC, to be quickly integrated on hardware and prototypes. Afterwards, the automotive radar sensors from several companies are presented and their technical specifications highlighted. These automotive radar sensors are available as kits, Commercially Off-the-Shelf (COTS), which do not require additional electronic design. Finally, in section 2.4, recent scientific works about 4D imaging radar regarding automotive applications, mainly focusing on object detection, object classification/recognition and resolution enhancing, will be reviewed.

2.1 History

Automotive radar systems are in continuous evolution since the 1960s [12, 13]. In the early 1970s the first radar sensors at 35 GHz were tested over several millions of road kilometers [14]. Still during the 1970s companies such as Bendix Corporation, Info Systems Inc., RCA, General Motors, Mitsubishi and Nissan started investigating and testing with automotive radars [13]. Some of these early development radar tests on vehicles can be seen in Fig. 2.1. The 24 GHz Industrial, Scientific and Medical (ISM) band became a preferred frequency for low-cost sensors and the 76-77 GHz band was assigned worldwide for automotive radar [13]. The first operational radar system appeared on the market in 1992 for buses and trucks and continued ever since [12]. Such radar system, the 24 GHz VORAD (Vehicle on-board radar) CWS, was build by EATON and used a switched multiple frequency modulation, a GUNN diode oscillator with 0.5 mW of power and planar antennas [13]. The VORAD CWS radar system was installed in more than 4000 buses and trucks in the USA, providing an acoustic warning to the driver [15]. In total these radar systems traveled on more than 900 million kilometers of road, reducing the amount of accidents per km traveled by more than 50 percent [15]. In Fig. 2.2 the VORAD CWS radar system can be seen mounted on the front of a Greyhound bus.

Commercial radar sensors for passenger cars appeared on the market in 1998/99 and have been around ever since, both working in the 24 GHz and 76 GHz frequency band [12]. The first commercial 76 GHz automotive radar for passenger cars, the ARS100, was introduced by Mercedes Benz at that time [13], and was used for ACC purposes. The ARS100, shown in Fig. 2.3, was a radar sensor built by Macom [16], it used a folded parabolic reflector



(a) (b) (c)

Figure 2.1: Early automotive radar developments and in-vehicle tests during the 1970s. (*a*) 10 GHz radar system built by VDO. (*b*) 16 GHz radar system built by Standard Electric Lorenz. (*c*) 35 GHz radar system built by AEG-Telefunken. [Figures extracted from [15]]



Figure 2.2: 24 GHz VORAD CWS radar system (highlighted in red) mounted on the front of a Greyhound bus. [Figure extracted from [15]]

antenna and was firstly based on a GUNN oscillator and a microstrip receiver circuit, but later on, GaAs (Gallium Arsenide) Monolithic Microwave Integrated Circuits (MMIC) was included [13]. Advanced versions of this radar sensor were then developed by Continental, firstly by replacing the folded parabolic reflector antenna with a folded reflectarray antenna and by including GaAs MMICs [13]. See [16–18] for specific details about these first 76/77 GHz radar sensors.



Figure 2.3: ARS100 - The first commercial 76 GHz automotive radar sensor.

Since then, automotive radar became commercially available and was employed by various Original Equipment Manufacturer (OEM) all over the world [14]. A new frequency band for radar sensors from 77 to 81 GHz has been allocated recently in Europe [12]. Currently, automotive radar sensors are used for various vehicular applications besides ACC, such as BSD, Rear Collision Warning (RCW), Emergency Braking (EB), to mention a few. Furthermore, and to conclude this section, an extensive and detailed review on automotive radar is impeccably presented by its authors in [13].

2.2 Frequency Bands and Types of Operation

As mentioned in the previous section, automotive radars have been using primarily four frequency bands. There is the 24 GHz ISM band from 24.0 GHz to 24.25 GHz, which is often called the Narrow Band (NB), having a bandwidth of 250 MHz, and there is also an 24 GHz Ultra Wide Band (UWB) from 21.65 GHz to 26.65 GHz, which has 5 GHz of available bandwidth. Then, there is the automotive Long Range Radar (LRR) band from 76 GHz to 77 GHz, with 1 GHz of available bandwidth, that has the benefit of high allowed Equivalent Isotropic Radiated Power (EIRP), and finally, there is the automotive Short Range Radar (SRR)/Medium Range Radar (MRR) band from 77 GHz to 81 GHz, which has a wide sweep bandwidth up to 4 GHz. In Fig. 2.4 it is possible to see the frequency spectrum of the bands used for automotive radar applications. However, due to spectrum regulations and standards developed by the European Telecommunications Standards Institute (ETSI), Federal Communications Commission (FCC), Electronic Communications Committee (ECC) and International Telecommunication Union (ITU), [19–22] respectively, it was decided to phase out the 24 GHz UWB band. It is currently unavailable since January 1st of 2022, both in Europe and in the United States of America, only the narrowband ISM band will be available long term. This lack of wide bandwidth in the 24 GHz band, coupled with the need

for higher performance in emerging radar applications, makes 24 GHz unattractive for new radar implementations [23].

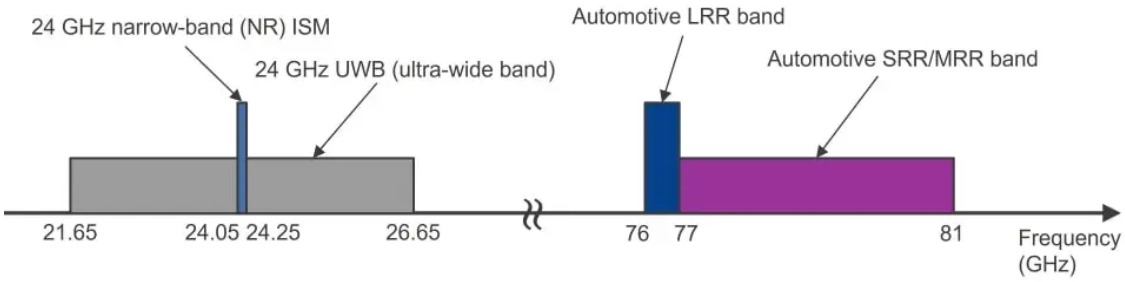


Figure 2.4: Frequency bands for automotive radar. [Figure extracted from [1]]

Automotive radars are typically classified based on their maximum range detection and/or FoV. There are different types of automotive radar, or types of operation, available. Each type exhibits unique characteristics and is used for different applications. Even though there are no official definitions, the TR 103 593 technical report from the ETSI, [19], and also the ITU-R M.2057-0 recommendation from ITU, [22], describes the types of operation as following:

- **Ultra Short Range Radar (USRR)** - Has a detection range up to 15 m with a typical FoV of 90°/110° and operates in the 24 GHz UWB and in the 77-81 GHz frequency bands. USRR is primarily used for close-range detections, such as PAS, BSD, RCW and CWS. It provides very accurate range detections that help the driver avoid collisions during navigation at low speeds, through tight spaces or during parking.
- **SRR** - Has a detection range up to 50 m with a typical FoV of 80°/90° and operates in the 24 GHz UWB and in the 77-81 GHz frequency bands. Just like the USSR, SRR is primarily used for close-range detections, such as PAS, BSD, RCW and CWS. It provides very accurate range detections that help the driver avoid collisions during navigation at low speeds, through tight spaces or during parking.
- **MRR** - Has a detection range up to 150 m with a typical FoV of 50°/60° and operates in the 24 GHz NB and UWB, in the 76-77 GHz and in the 77-81 GHz frequency bands. MRR is primarily used for ACC, CWS, Lane Change Assist (LCA), BSD and EB. It is generally used to detect, and/or track, vehicles ahead.
- **LRR** - Has a detection range up to 250 m, or more, with a typical FoV of 20°/25° and operates in the 24 GHz NB and in the 76-77 GHz frequency bands. LRR is primarily used for ACC, CWS, Collision Avoidance (CA), EB and highway driving assist. It is generally used to detect, and/or track, vehicles ahead. Since it is used for detections at a greater range, it is crucial to provide early warnings, thus enabling proactive measures.

Aside from the previous types of radar operation, high resolution imaging radar technology based on mmWave systems has gained considerable and increasing attention in recent years. Radar imaging is a remote sensing subcategory that requires raw radar data to be collected over an artificially extended aperture that is much larger that the radar receiving antenna and

[1] `https://semiengineering.com/radar-for-automotive-why-do-we-need-radar/?utm_producer=juanantoniodiaz` [Accessed on the 14th of September of 2023]

processed to create a reflectivity image of a scene [24], essentially meaning that imaging radars can provide a radio photo of a surrounding scenario, with benefits such as: high-resolution, robustness and cost efficiency. In conclusion, Fig. 2.5 shows the typical FoV and range that each type of automotive radar has, while Fig. 2.6 presents a possible 360° radar configuration for a vehicle, highlighting the types of operation and their strategic location on the vehicle according to their specific detection features.

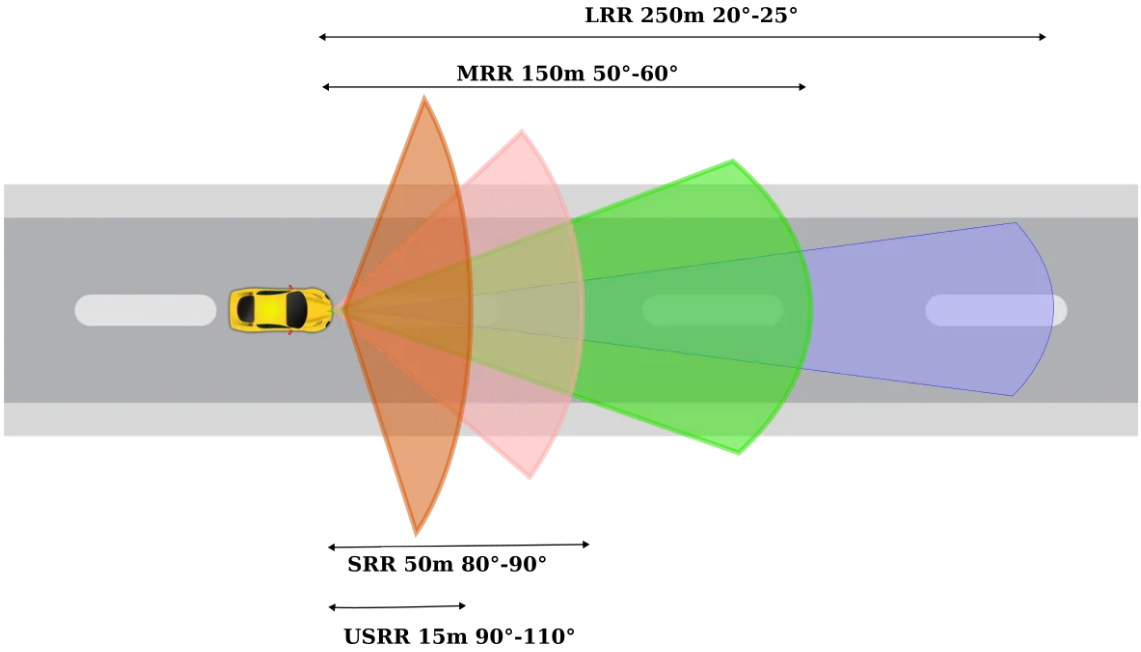


Figure 2.5: Automotive radar types of operation. [Figure extracted from [2]]

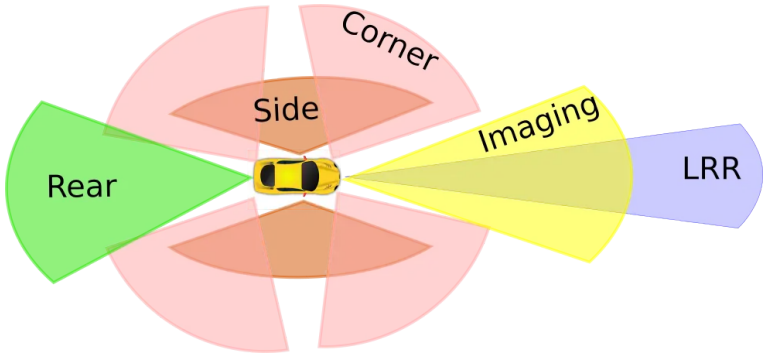


Figure 2.6: Radar positioning on the vehicle for 360° awareness. [Figure extracted from [3]]

[2] https://www.keysight.com/blogs/en/tech/educ/2023/automotive-radar [Accessed on the 14th of September of 2023]

[3] https://www.keysight.com/blogs/en/tech/educ/2023/automotive-radar [Accessed on the 14th of September of 2023]

2.3 State-of-the-Art Market Solutions

A literature review has been performed in this work to identify the state-of-the-art market solutions for radar systems, particularly focusing on the ones for automotive and industrial applications. In the following subsections those solutions will be presented, starting with an overview of a common radar System-on-Chip (SoC), commonly known as Radar-on-Chip (RoC), and then followed by several radar systems that integrate these RoC with some more electronics in order to create a full working radar system. To be hardware and cost efficient, current state-of-the-art automotive radar sensors use Frequency Modulated Continuous Wave (FMCW) radar technology, in particular the chirp sequence modulation with stretch processing [25]. The solutions presented in this document all use this type of technology.

2.3.1 Radar-on-Chip

Radar-on-chip is a solution that integrates all of the RF/Analog circuitry, Phase-Lock-Loop (PLL), mixers, filters, Analog-to-Digital Converter (ADC), Power Amplifier (PA) and Low Noise Amplifier (LNA) as well as a Digital Signal Processor (DSP) and a microprocessor, both programmable, were all of the radar processing is handled. These are solutions that can be used to quickly make a radar system prototype for a proof-of-concept or used in industry for final products. In Fig. 2.7, highlighted in purple and integrated in an evaluation board, it is shown one of these RoC solutions, the AWR1843 from TI, which is integrated in the radar evaluation board that is used throughout this work and will be explained in detail in the next chapter, 3, section 3.2. In Fig. 2.8 it is shown it´s block diagram.

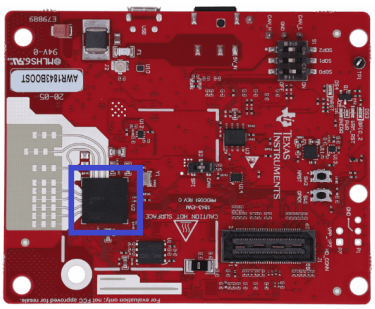


Figure 2.7: Radar-on-chip used on the TI AWR1843BOOST.

In Table 2.1 it is presented a comparison of some of the most used/known RoC solutions.

With these RoC, companies can manufacture the most diverse radar systems, often combining several RoCs into a single system to increase the number of TX and RX channels, hence its resolution and accuracy, or incorporating antenna arrays with different polarizations, offering a more configurable radar system. For example, in Fig. 2.9 it is shown three different radar development boards, where it is possible to see the integration of RoCs and the antenna arrays, 2.9a and 2.9b being designed by Colorado Engineering and 2.9c by Texas Instruments.

The following subsections present some of the most used automotive radar systems on the market, as well as some development boards, which all integrate a RoC within their system. In order to avoid the repetition of similar images, considering the fact that automotive radar systems look identical, Fig. 2.10 presents the typical main board of such system as well as their robust enclosure.

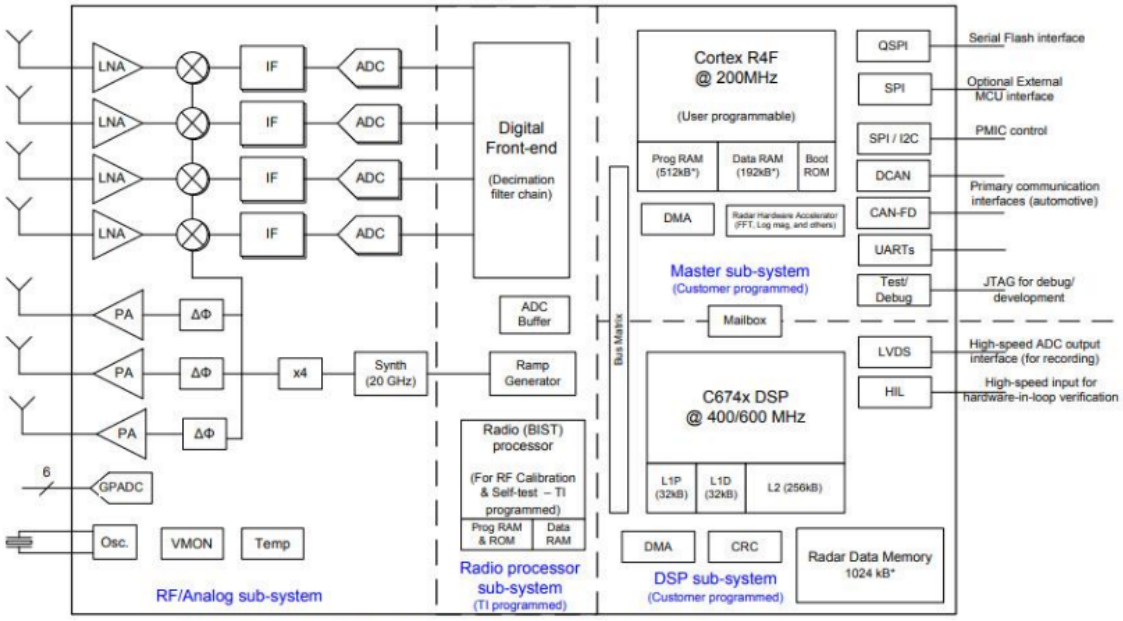
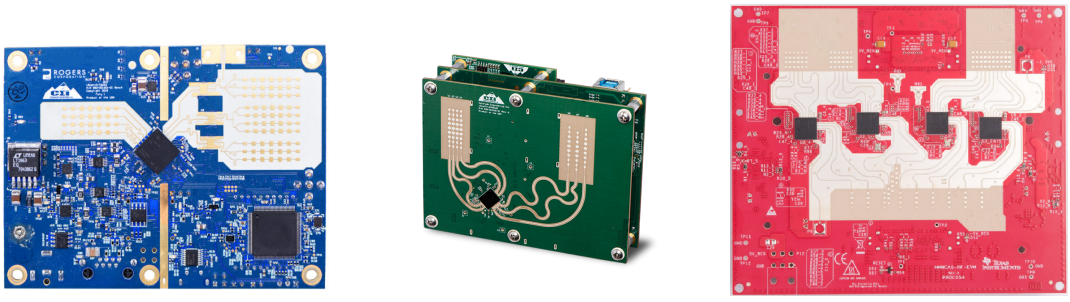


Figure 2.8: AWR1843 RoC block diagram.

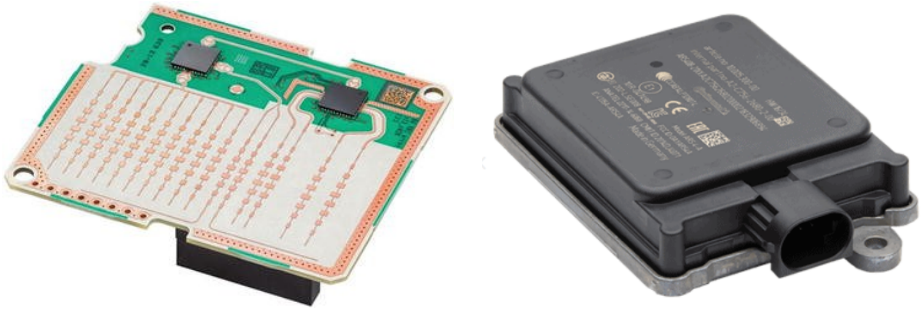
Manufacturer	Model	Frequency Band	Bandwidth	TX Power	Nº of Channels
Infineon	BGT24MTR12	24GHz	250MHz	11dBm	1TX 2RX
Infineon	RXS8150PL	77GHz	2GHz	N/D	2TX 4RX
Infineon	RXS8160PL	77GHz	2GHz	N/D	3TX 4RX
STMicro	STRADA431	24GHz	250MHz	13dBm	1TX 3RX
STMicro	STRADA770	77GHz	N/D	10dBm	3TX 4RX
TI	AWR1642	77GHz	4GHz	12dBm	2TX 4RX
TI	AWR1443	77GHz	4GHz	12dBm	3TX 4RX
TI	AWR1843	77GHz	4GHz	12dBm	3TX 4RX
TI	AWR2243	76GHz	5GHz	13dBm	TX 4RX
NXP	MR3003	77GHz	4GHz	N/D	3TX 4RX
NXP	TEF8101/2	77GHz	2/4GHz	N/D	3TX 4RX

Table 2.1: Radar-on-Chip Solutions.



(a) Fury. (b) iScan Phantom. (c) TIDEP-01012.

Figure 2.9: Radar development boards.



(a) Main PCB. (b) Enclosure.

Figure 2.10: Typical automotive radar system.

2.3.2 TI TIDEP-01012

TIDEP-01012 is an evaluation board that uses 4 cascaded RoC, the AWR2243. The RoC itself is similar, in terms of specifications, to the one presented in the last subsection. By using 4 cascaded RoC, the antenna structure is quite big, having 16 antennas used for reception and 12 antennas used for transmission, in a MIMO configuration. This antenna structure allows for the radar to have a 140° degree field-of-view in the azimuth plane and a 40° degree field-of-view in the elevation plane, and allows angle estimation in both planes, having a resolution of 1.4° in the azimuth plane and 18° in the elevation plane. This radar sensor can work in the following modes: LRR, MRR and SRR. In the LRR mode the radar can detect targets up to 350m with a resolution of 35cm, and with a velocity up to 130km/h with a resolution of 0.5km/h. In the SRR mode the radar can detect targets up to 30m with a resolution of 4.3cm, and with a velocity up to 130km/h with a resolution of 0.5km/h. Finally, this evaluation board comes with the following interfaces: Serial Peripheral Interface (SPI), Inter-Integrated Circuit (I2C), Universal Asynchronous Receiver-Transmitter (UART) and Low-Voltage Differential Signaling (LVDS). Once more, all of these specifications can be found in detail in the technical datasheet [26] as well as in the design guide [27].

2.3.3 Continental ARS430

ARS430 is an automotive radar sensor produced by Continental accordingly to all of the automotive regulations and standards, and already being used by several car models. The ARS430 is a FMCW radar sensor that covers the 77-81 GHz band, and has 4 GHz of available bandwidth. This radar can detect targets up to 250m (in LRR) and has a resolution of 40cm (in SRR), and a precision of 10cm (in SRR). It can detect targets with velocities up

to 200km/h (in LRR) with a resolution of 0.43km/h (in SRR), and a precision of 0.1km/h (also in SRR). It has a field-of-view in the azimuth plane of 120° (in SRR) and 18° (in LRR), with a resolution of 1.6° (in SRR) and a precision of 0.1° (in SRR). Finally, this radar sensor comes with the following interfaces: Controller Area Network (CAN), FlexRay and Ethernet. Once more, all of these specifications can be found in detail in the technical datasheet [28].

2.3.4 Continental ARS408

ARS430 is also an automotive radar sensor produced by Continental accordingly to all of the automotive regulations and standards, and it is possibly the most used radar in car models, as of today. The ARS408 is a FMCW radar sensor that covers the 76-77 GHz band, and has 1 GHz of available bandwidth. This radar can detect targets up to 250m (in LRR), 70m (in MRR) and 20m (in SRR), with a resolution of 1.8m (in LRR) and 40cm (in both MRR and SRR), and a precision of 40cm (in LRR) and 10cm (in both MRR and SRR). It can detect targets with velocities up to 200km/h with a resolution of 0.37km/h (in LRR) and 0.43km/h (in SRR) with a precision of 0.1km/h. It has a field-of-view in the azimuth plane of 120° (in SRR) and 18° (in LRR), with a resolution of 4.5° (in SRR) and 31.6° (in LRR) with a precision of 1° (in SRR) and 0.1° (in LRR). Finally, this radar sensor comes only with the CAN bus interface. Once more, all of these specifications can be found in detail in the technical datasheet [29].

2.3.5 Smartmicro UMRR-11 Type 132

UMRR-11 Type 132 is an automotive radar sensor produced by Smartmicro accordingly to all of the automotive regulations and standards. The UMRR-11 Type 132 is a FMCW radar sensor that covers the 76-77 GHz band, and has 1 GHz of available bandwidth. This radar can detect targets up to 175m (in LRR) with a precision of 50cm (in LRR) and 25cm (in MRR). It can detect targets with velocities up to 200km/h (in LRR) and 170km/h (in MRR) with a precision of 0.1km/h. It has a field-of-view in the azimuth plane of 100° (in MRR) and 32° (in LRR), with a precision of 0.5° (in MRR) and 0.25° (in LRR), and a field-of-view in the elevation plane of 15° with a precision of 0.5°. Finally, this radar sensor comes with the following interfaces: CAN and Ethernet. Once more, all of these specifications can be found in detail in the technical datasheet [30].

2.3.6 Smartmicro UMRR-96 Type 153

UMRR-96 Type 153 is also an automotive radar sensor produced by Smartmicro accordingly to all of the automotive regulations and standards. The UMRR-96 Type 156 is a FMCW radar sensor that covers the 77-81 GHz band, and has 4 GHz of available bandwidth. This radar can detect targets up to 120m (in LRR) with a precision of 50cm, 55m (in MRR) with a precision of 30cm and 20m (in SRR) with a precision of 15cm. It can detect targets with velocities up to 140km/h with a precision of 0.15km/h. It has a field-of-view in the azimuth plane of 130° (in both MRR and SRR) and 100° (in LRR), with a precision of 0.1°, and a field-of-view in the elevation plane of 15° with a precision of 2°. Finally, this radar sensor comes with the following interfaces: CAN and Ethernet. Once more, all of these specifications can be found in detail in the technical datasheet [31].

2.3.7 Ainstein mmWave O-79

Ainstein mmWave O-79 is a FMCW radar sensor that covers the 77-81 GHz band, and only works as MRR and SRR. This radar can detect targets up to 20m (in LRR) with a resolution of 20cm. It can detect targets with velocities up to 2.3m/s with a resolution of 0.04m/s. It has a field-of-view in the azimuth plane of 90° with a resolution of 5.7°, and a field-of-view in the elevation plane of 30° with a resolution of 18°. Finally, this radar sensor comes with the following interfaces: CAN and Ethernet. Once more, all of these specifications can be found in detail in the technical datasheet [32].

2.3.8 Bosch Corner/Front/Front Premium

Corner/Front/Front Premium comprehends a set of FMCW automotive radar sensors produced by Bosch accordingly to all of the automotive regulations and standards, with the same footprint. The Corner is used as MRR and SRR, while the Front and Front Premium are used as LRR and MRR.

The corner radar can detect targets up to 160m with a precision of 12cm, and can detect targets that are down to 45cm apart. It can detect targets with velocities up to 0.3m/s with a precision of 0.04m/s. It has a field-of-view in the azimuth plane of 130° with a precision of 0.1°, and can detect targets that are separated by 4°. It has a field-of-view in the elevation plane of 30° with a precision of 0.2°, and can detect targets that are separated by 6°.

The front radar can detect targets up to 210m with a precision of 10cm, and can detect targets that are down to 20cm apart. While the front premium radar can detect targets up to 300m with a precision of 11-22cm, and can detect targets that are down to 41-83cm apart. Both radars, front and front premium, have a velocity precision of 0.05m/s and can detect targets that have a difference in velocity of 0.1m/s. Both radars have a field-of-view equal to the corner radar.

Finally, all of these radar sensors come with the following interfaces: CAN and Ethernet. Once more, all of these specifications can be found in detail in the technical datasheets [33–35].

2.3.9 Altos V1

Altos V1 is an automotive 4D imaging radar sensor produced by Altos, that, as of summer of 2023, has the best performance on the automotive 4D imaging radar market, according to its manufacturers. In the manufacturer's website a video is presented were it is possible to see the comparison between Altos V1 and Hesai AT128 (the best mass-produced Light Detection And Ranging (Lidar) currently on the market), where the real-time point-clouds of both sensors are shown, and it is possible to see that Altos V1 has an outstanding performance, almost matching the lidar results in terms of accuracy and resolution.

Altos V1 radar can detect targets up to 350 m with a resolution of 31 cm and an accuracy of 10 cm. It can detect targets with velocities from -110 m/s to 55 m/s with a resolution of 0.2 m/s and an accuracy of 0.02 m/s. It has a field-of-view in the azimuth plane of 100° with a resolution of 1.32° and a precision of 0.14°. It has a field-of-view in the elevation plane of 23° with a resolution of 1.43° and a precision of 0.32°. It features 12 Transmit (TX) and 16 Receive (RX) channels. It outputs a 3D point-cloud with up to 3000 points per frame, outputting 10 frames per second.

Finally, Altos V1 radar comes with the following interfaces: Ethernet (100base-T1 User Datagram Protocol (UDP) multicast) and Universal Serial Bus (USB). All of these specifications can be found in more detail in the manufacturer's website [4].

2.4 Literature Review

This subsection presents a brief literature review on current research topics regarding automotive radar systems, complementing the display of state-of-the-art technologies from the previous subsection. It examines scientific publications from various authors, focusing on novel approaches and synthesizing recent advancements in radar hardware, signal processing techniques, and sensor fusion. This review offers a comprehensive overview of emerging trends and challenges shaping the future of automotive radar systems.

In [36], the authors proposed a new radar detector network, called RPDNet, based on deep learning, which is used in the process of generating radar point clouds from raw radar data. The radar detector uses lidar data, only during the model training, to generate the labels. Finally, by combining the label results from the previous operations, a label matrix is generated. By combining the label matrix with the radar data a radar point cloud is generated. The results show that the RPDNet detector has better performance on suppressing radar clutter and generating denser point clouds. Fig 2.11 presents the point-clouds generated by the RPDNet detector *vs.* the "normal" radar and lidar ones, for the same target.

Remarkably in [37], the authors proposed an object classification network, called Radar Transformer. The network takes the radar point cloud as the input and maps it into a feature vector. Deep local features are then extracted using the nearest neighbour algorithm for grouping, which are then integrated to get the final radar point cloud. The collected data has 5 classes (persons, cyclists, motorcyclists, cars and buses). Final results show that this classification model works really well when classifying cars and buses, the degree of confusion is very low and the model makes a good classification. When classifying persons and non-vehicles (cyclists and motorcyclists) the model misclassifies more often, but still rarely. The authors then decided to join cyclists and motorcyclists into one class since they have strong similarities, in order to improve the overall accuracy of the model. The new class is now called non-vehicles. By combining the cyclists and motorcyclists into one class the overall accuracy of the model was improved. Overall this classification model works well and has a good accuracy.

In the work [38], it is proposed a novel radar multiple-perspectives convolutional neural network (RAMP-CNN) that extracts the location and class of objects based on further processing of the range-velocity-angle heatmap sequences. This method combines the spatial and temporal domain information by processing the 3D radar cube sequences, but sliced as 2D images from 3 perspectives, range-angle heatmap, range-velocity-heatmap and velocity-angle heatmap, in order to reduce the computational complexity. These are then processed in parallel deep learning models to generate different features. Camera images are then used as the ground truth for supervising the output of the RAMP-CNN. The RAMP-CNN was then tested under 4 different scenarios: parking lot, curbside, on-road and during night time. The performance results of RAMP-CNN show overall improvements when compared to prior object classification models, especially for moving objects.

[4] `https:altosradar.com/product` [Accessed on the 17th of January of 2024]

Alternatively in [39], the authors study the feasibility to detect and classify targets with a weak Radar Cross Section (RCS), such as pedestrians, using a 4D MIMO radar. Radar point clouds of objects with a weak RCS are sparse and have a low point density, which which makes them unusable for classification models. The authors proposed the use of a particle filter, where the probability density function of the points is used for the classification instead. Two measurements were completed to verify the proposed approach, a walking person in front of a car and a child dummy lying on the ground. The moving pedestrian was successfully tracked and the child dummy was successfully located. Fig 2.12 presents the results of the moving pedestrian measurement, where the red lines are the estimated positions and the blue points are the centroids of the particle clouds.

In [40] the authors proposed a novel high-resolution 4D imaging radar system with 1728 virtual channels, which exceeds the state-of-the-art channel count for automotive radar sensors by a factor of 9. The proposed system consists of 12 MMIC radar transceivers, each with 4 receiving (RX) channels and 3 transmitting (TX) channels. By using 12 radar transceiver MMICs the proposed system will end up having 48 RX channels and 36 TX channels, resulting in a large antenna array with $48 * 36 = 1728$ virtual channels. The total aperture of this system covers 130º in the azimuth plane and 75º in the elevation plane. Results with this system show that it is able to differentiate targets with an angular separation of 0.9º in the azimuth plane and 4º in the elevation plane, and overall radar images present a high level of detail.

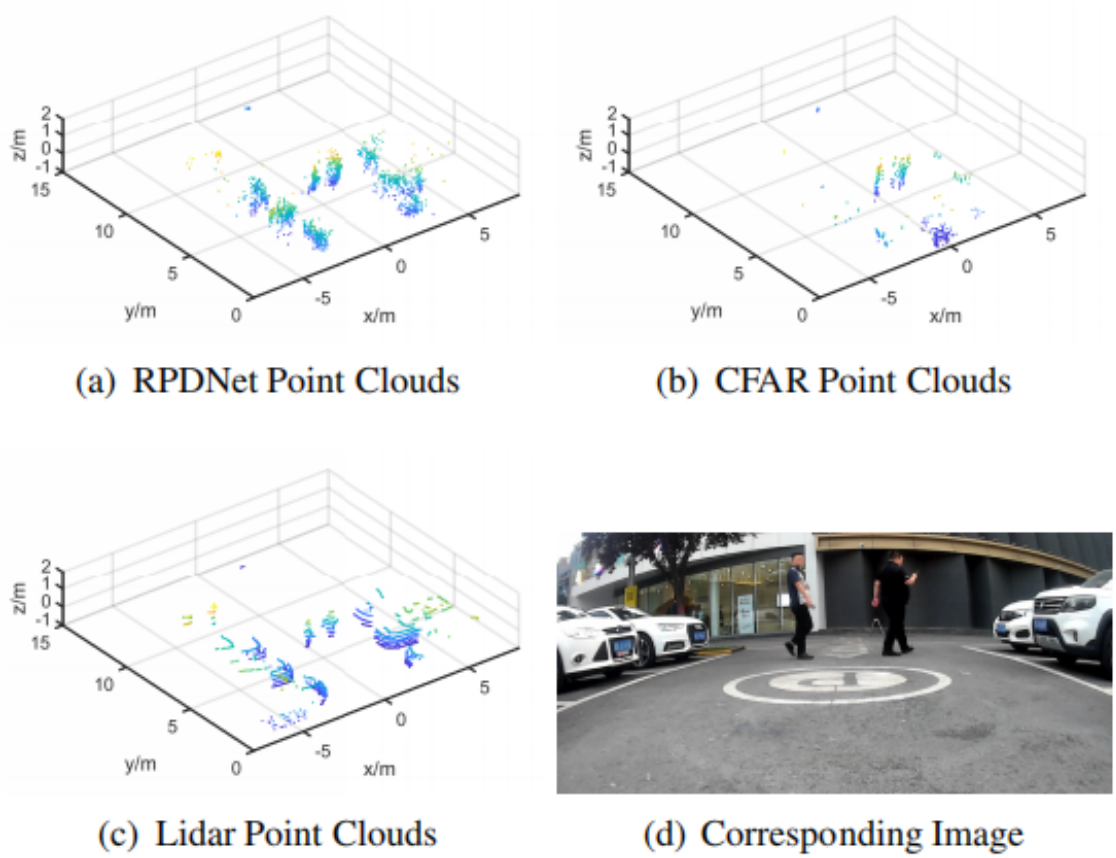
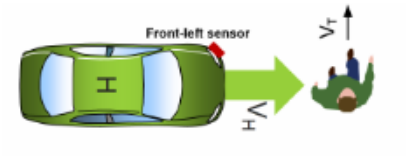
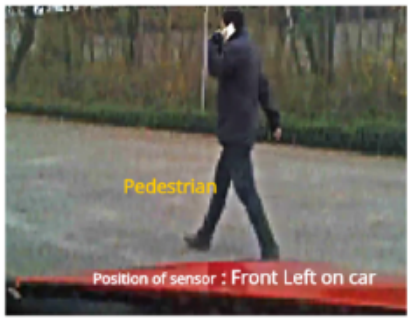
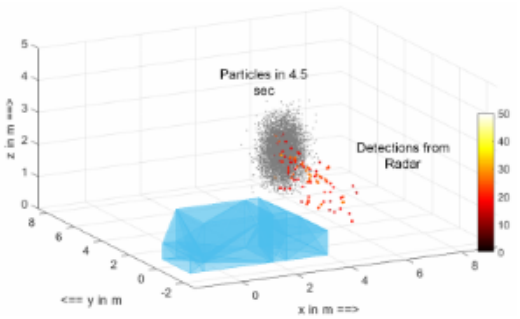


Figure 2.11: RPDNet object detection.

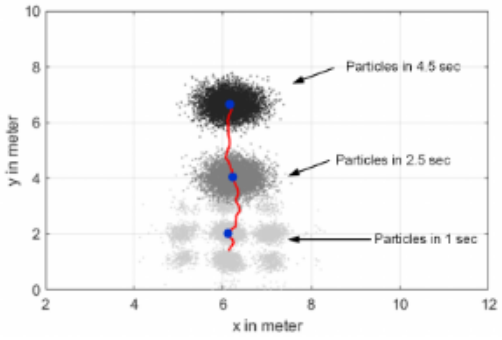




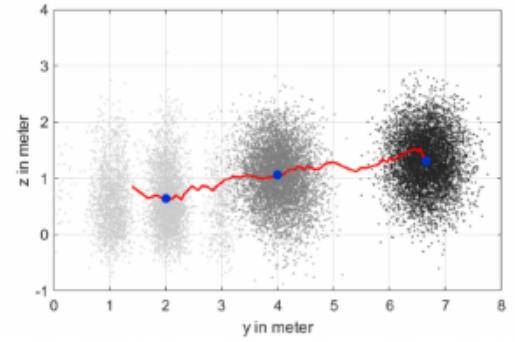
(a) Scenario of the adult pedestrian walking across the front of the host car.



(b) 3D map of the detections of the pedestrian from the radar compared to the particle cloud. The coordinate used is as depicted.



(c) Evolution of the particle cloud within a few seconds.



(d) Height detection and tracking of the pedestrian walking away from the host car.

Figure 2.12: Pedestrian detection and height estimation using particle filter.

Chapter 3

mmWave 4D Radar Developments

This chapter will provide an overview on the working principle, from the background theory to its operation, of a 4D radar system based on TI SoC radars, for automotive and Unmanned Aerial Vehicles (UAV) applications. There are several radar technologies available, however, the focus here is to present the FMCW radar technology, considering that the radars referenced in this document work under this principle. The first section, 3.1, addresses the theory and working principles of the FMCW radar system. In the second section, 3.2, the AWR1843BOOST evaluation board is presented along with its characteristics/parameters and it's configuration is also discussed. The third section, 3.3, addresses the 360° radar prototype, a real-time and high resolution 4D MIMO radar sensor with 360° of field of view. Later on, in the fourth and fifth sections, 3.4 and 3.5, the description of two proposed working architectures regarding the radar 360° radar prototype are presented, one running on a computer through MATLAB with a dedicated GUI and another using a dedicated hardware. In the sixth section, 3.6, experimental results with the 360° radar are displayed to validate the proposed concept. Finally, in the seventh section, 3.7, the main conclusions are presented, followed by a brief discussion of results.

3.1 FMCW Radar Fundamentals

3.1.1 FMCW Radar

The FMCW technique is widely used in radar systems as it shows a high immunity to external signal interference and requires a low processing capacity and data acquisition. In FMCW radar solutions a linear FMCW chirp sequence is transmitted, were the frequency varies over time. Fig. 3.1 shows the generic high-level block diagram of a FMCW radar implementation, whose working principle goes as follows: a TX chirp, depicted in Fig. 3.2 and 3.3, is generated by modulating the sawtooth reference signal (generated in the FMCW Waveform Generator) with a high frequency carrier (generated by the Voltage Controlled Oscillator (VCO)) and is then amplified by the PA and delivered to the TX antenna. The transmitted signal then travels through the air until it hits an object. When it does the signal gets reflected, thus creating the echo signal, a delayed version of the transmitted one. The echo signal (represented as RX in Fig. 3.2 and 3.3) travels back until is received by the RX antenna. Afterwards, it is amplified by the LNA and then down-converted to produce the Intermediate Frequency (IF) signal, which contains the beat frequency. The beat frequency corresponds to the frequency difference between the transmitted signal and the received echo signal. The IF signal then passes through a Low Pass Filter (LPF) and is sampled to digital using an ADC. The sampled signal is then processed using a microprocessor or digital signal processor in order to compute the targets parameters.

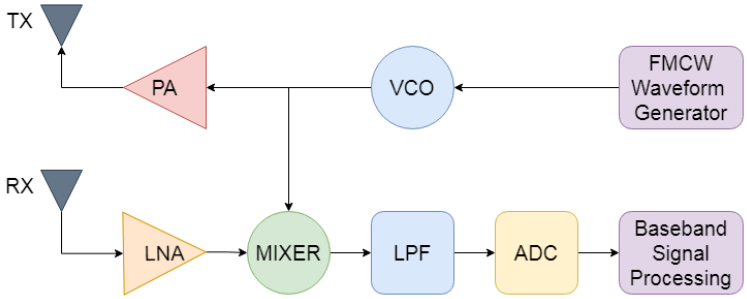


Figure 3.1: Generic high-level block diagram of an FMCW radar.

In Fig. 3.2 it is possible to observe the visual representation of the spectrum of the transmitted and received chirp sequences as they vary with time (also known as "sawtooth shape modulation"), while in Fig. 3.3 it is possible to observe them in the time domain. The difference between the transmitted and received chirp signals is directly proportional to the time of flight.

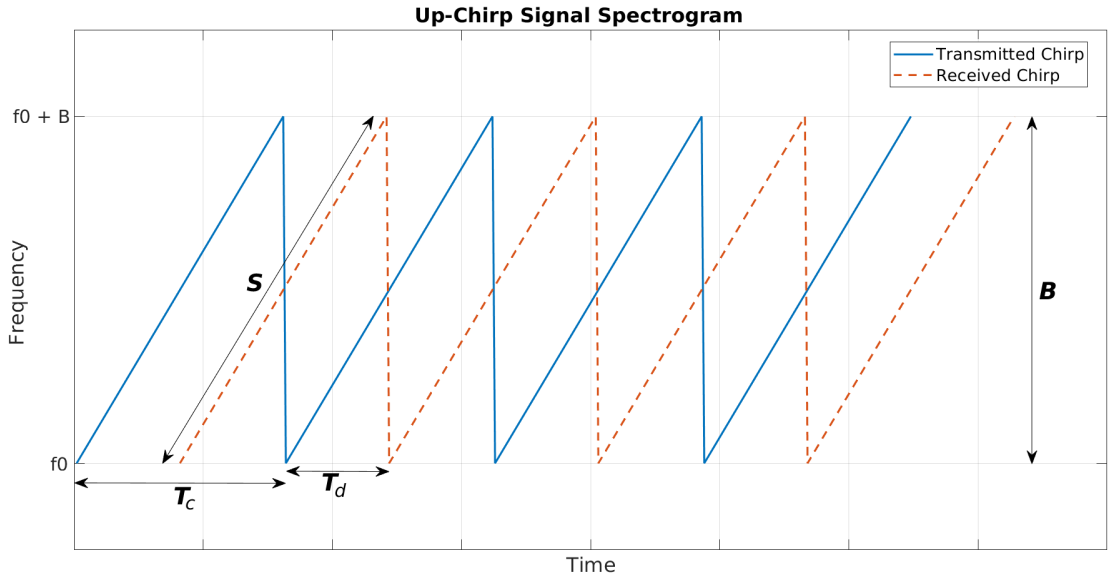


Figure 3.2: Up-chirp signal spectrogram.

The chirp is a sinusoidal signal that starts with a certain frequency that keeps increasing at a given rate until it reaches the stop frequency. In Fig. 3.2 it is possible to see the transmitted and received chirps. The chirp is typically characterized by the start frequency (f_0), the bandwidth (B), the time period of the sequence (T_c) and the slope (S), which indicates the rate at which the frequency of the chirp increases and is given by 3.1. T_d is the time delay between the transmitted and received chirp, and can be mathematically expressed as 3.2, where d is the range to the target object and c is the speed of light.

$$S = \frac{B}{T_c} \tag{3.1}$$

$$T_d = \frac{2d}{c} \tag{3.2}$$

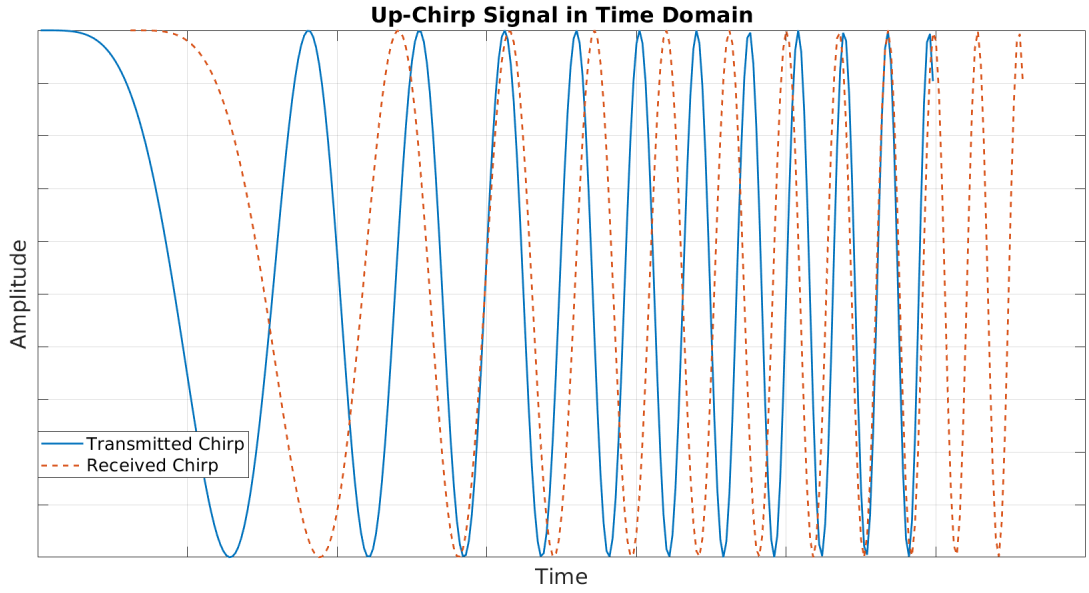


Figure 3.3: Up-chirp signal in time domain.

Finally, in Fig. 3.4 it is possible to observe a representation of the beat frequency for a given transmitted chirp and its echo. f_{bu} and f_{bd} are the lowest and highest points of the beat frequency, created by the up and down modulation slopes of the chirps, respectively.

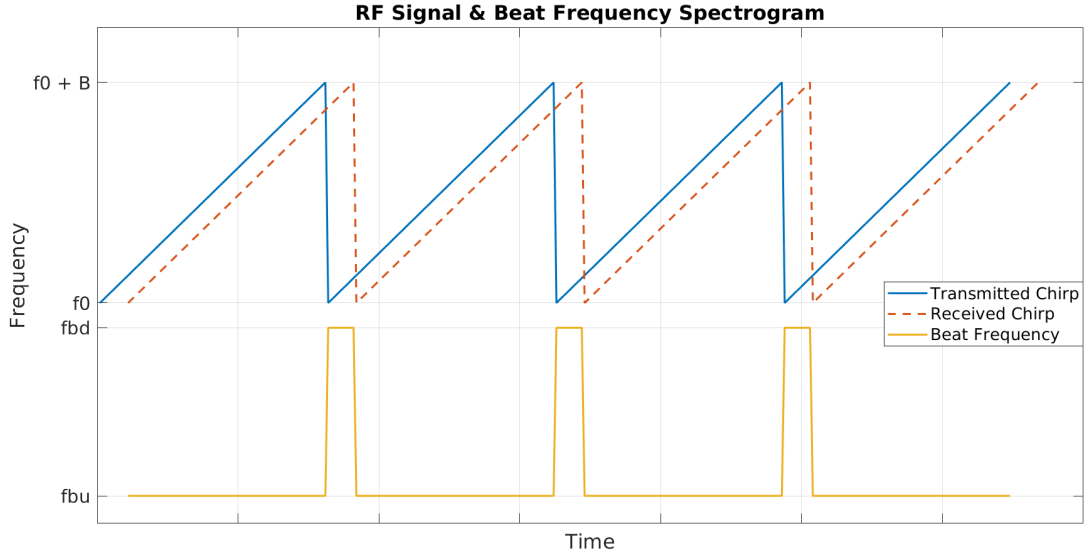


Figure 3.4: Beat frequency spectrogram.

3.1.2 Range Estimation

Range estimation is fundamental to any radar system. Its purpose is, as the name implies, to estimate the physical range between the target object and the radar. Range estimation algorithms can slightly vary in details from one another, but the typical "high-level" procedure consists of finding the beat frequency, for single target, or beat frequencies, for multiple targets, and then from it compute the range.

In Fig. 3.5 it is presented a multiple target scenario, where 3 stationary targets are in front of a radar system at different ranges, d_1, d_2 and d_3. For this scenario, Fig. 3.6 shows a representation of the transmitted signal and echo signals from each target, both in a spectrogram and in frequency domain. In a practical implementation the round-trip delay is typically just a small fraction of the total chirp duration, thus the non-overlapping segment of the transmitted chirp is usually negligible [41], in Fig. 3.6a the representation of this non-overlapping segment was exaggerated for visualization purposes only. Since the target objects are stationary the echo signals are just time delayed replicas of the transmitted signal, without any changes in frequency. This means that there's a constant of proportionality between the transmitted and received signal, which is the chirp slope (S) [41]. By mixing the delayed received signals with the transmitted one it is possible to produce the IF signal that contains a distinct beat frequency for each target object. By applying the Fast Fourier Transform (FFT) to the IF signal it is possible to obtain the beat frequency for each target object. These frequencies in the spectrum are represented as tones, whose frequencies are proportional to the ranges from the radar to the targets [41], and are easily detected because they stand out from the noise floor.

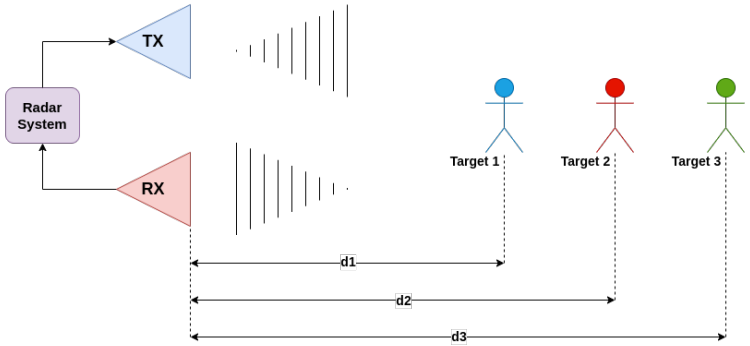


Figure 3.5: Diagram scenario of multiple target detection.

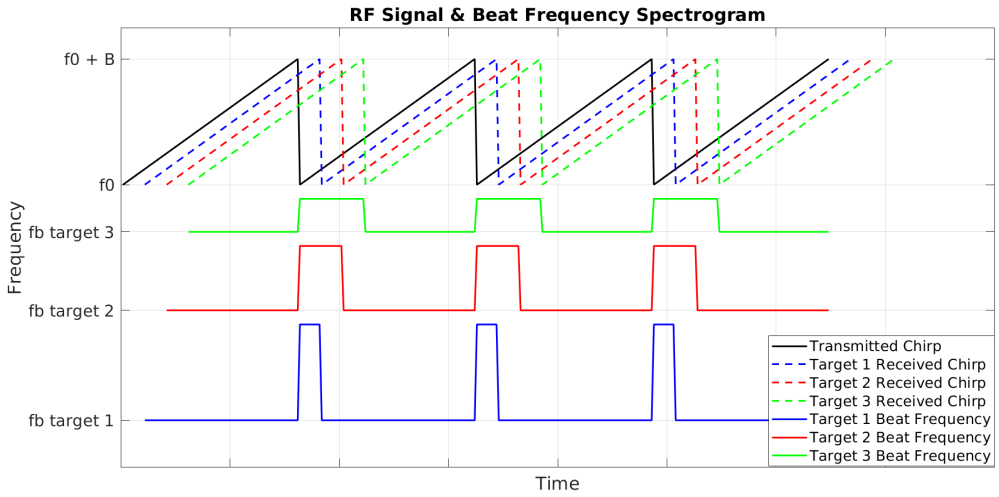
Therefore, the relation between the beat frequency (f_b) for a given stationary target object and it's range (d) to the radar is given by 3.3, with S being the slope of the chirp and c the speed of light.

$$f_b = \frac{2dS}{c} \iff d = \frac{cf_b}{2S} \tag{3.3}$$

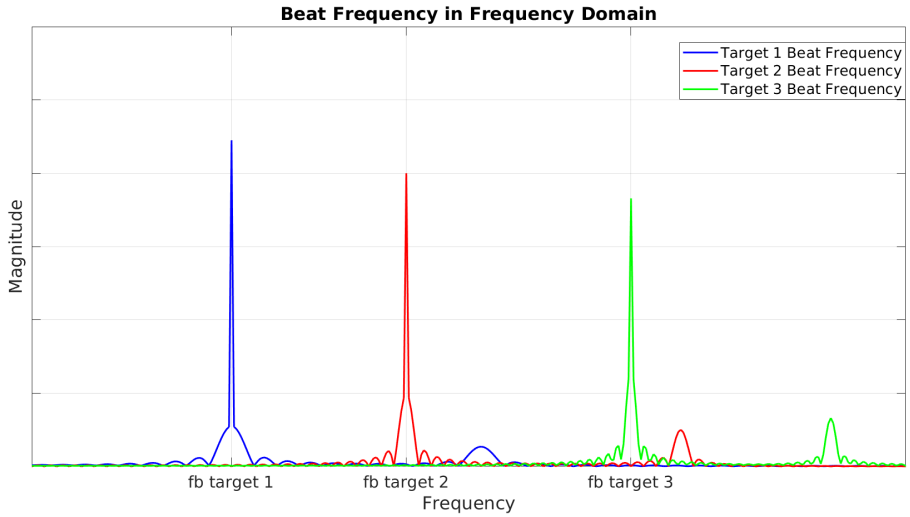
3.1.3 Range Resolution

Range resolution, d_{res}, refers to the ability that a radar system has to distinguish two or more close target objects, and is, therefore, a very relevant property in radar systems. It is, in other words, the smallest distance between two target objects that allows for them to be detected as separated objects rather than seen as only one. In a practical way this can be seen in the IF signal spectrum as two frequency peaks getting closer to each other until the radar system is no longer able to tell them apart, as it is represented in Fig. 3.7. It is possible to see that the beat frequency peaks get close to each other until it is impossible to differentiate one from the other.

In Fig. 3.7a it is possible to observe two distinct frequency peaks, each corresponding to a target object beat frequency. In this case the peaks are well separated in the spectrum and, consequently, are easily detected. The difference in frequency between these peaks is shown

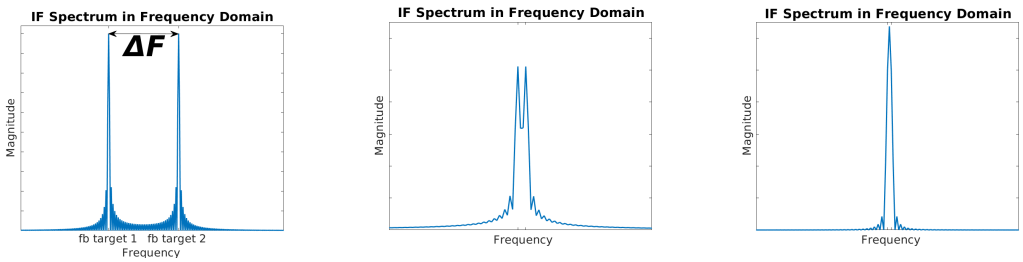


(a) Spectrogram



(b) In frequency domain

Figure 3.6: Tx and Rx ideal signal representation on a multiple target scenario (considering stationary objects).



(a) (b) (c)

Figure 3.7: Resolution in the IF frequency spectrum. (*a*) 2 distinguished targets. (*b*) 2 targets at the limit detection threshold. (*c*) 2 targets viewed as one, with no distinction between the peaks.

in the image as ΔF, and since the beat frequency, f_b, is given by 3.3, as a result we will end with 3.4. Analytically, two or more distinct IF signal tones can be distinguished as long as 3.5 is verified [41]. Thus, by rearranging the variables in 3.4, and having in mind 3.5 and 3.1, the range resolution, d_{res}, is given by 3.6. So, it is possible to conclude that the radar range resolution depends exclusively on the chirp available bandwidth, B.

$$\Delta F = \frac{2S\,\Delta d}{c} \tag{3.4}$$

$$\Delta F > \frac{1}{T_c} \tag{3.5}$$

$$d_{res} = \frac{c\Delta F}{2S} \Rightarrow d_{res} = \frac{c\frac{1}{T_c}}{2S} \Rightarrow d_{res} = \frac{c\frac{S}{B}}{2S} \Rightarrow d_{res} = \frac{c}{2B} \tag{3.6}$$

The radar system most frequently used in this work, the AWR1843BOOST, has 4 GHz of available bandwidth, providing a range resolution of 3.75 cm. In Fig. 3.8 it is possible to see the range resolution as a function of the available bandwidth, with the 4 GHz highlighted due to AWR1843BOOST. Despite having up to 4 GHz of used bandwidth in the RF transmitted signal, the bandwidth of the IF signal is typically in the order of a dozen MHz, due to the mixing of the TX and RX signals. This is one of the most important benefits of FMCW radar systems because they do not require extremely fast, and expensive, ADC's to sample the IF signal, hence their uniqueness.

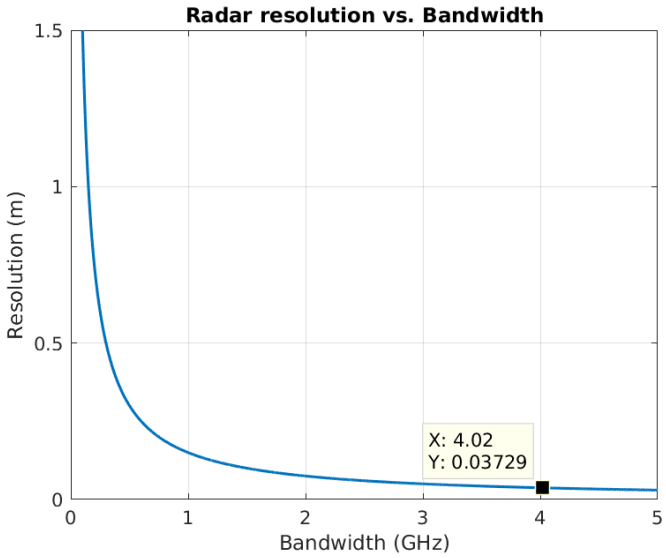


Figure 3.8: Radar range resolution vs. available bandwidth.

3.1.4 Velocity Estimation

Unlike the range estimation, where the target objects are stationary, the velocity estimation is done in a scenario where the target objects are moving towards or away from the radar, which affects the round-trip time delay, T_d, increasing it in the case where the target object is moving away from the radar or decreasing it in the case where the target object is moving

towards the radar. This not only affects the time delay but the frequency of the signal as well, which at reception is given by 3.7. This change in frequency is described by the Doppler effect, and is also known as Doppler shift, when talking about the frequency difference between the transmitted and received wave, which is given by 3.8, a simplification of 3.7.

$$f_{rx} = \left(\frac{1+\frac{v}{c}}{1-\frac{v}{c}}\right) * f_c \Longleftrightarrow f_{rx} = \left[1 + 2\left(\frac{v}{c}\right)\right] * f_c \tag{3.7}$$

$$f_{shift} = \left(\frac{2v}{c}\right) * f_c \tag{3.8}$$

However, the numerical values of Doppler shift are small compared with the radar frequencies because typical target velocities are very small when compared with the speed of electromagnetic wave propagation [42], which is very close to the speed of light. For example, a formula one racing car moving at 320 km/h detected with a mmWave radar at 77 GHz would cause a Doppler shift of only 45 kHz, which is practically indistinguishable, having in mind that 45 kHz is almost 2 million times smaller than 77 GHz. Since this would result in 2 tones with practically the same frequency, the approach to estimate the velocity of the target doesn't rely on the frequency shift but rather on the phase shift between the transmitted and reflected signal, considering that phase changes linearly with range variations of the target object [43]. The phase changes by $\Delta\varphi = \pi = 180^\circ$ for the quarter wavelength displacements, thus, the IF signal's phase is very sensitive to small changes in the object range [41]. The initial phase of the IF signal, the output of the mixer, is the the difference between the phases of both inputs of the mixer, the transmitted and received chirps [43]. The IF signal is a sine wave mathematically expressed as 3.9, where φ_0 is its initial phase. The phase difference between transmitted and received chirps is given by 3.10, considering also 3.2, the time difference between the chirps, where Δd is the range (in m) from the radar to the target object and λ is the wavelength (in m) of the transmitted RF signal.

$$IF = Asin(2\pi f t + \varphi_0) \tag{3.9}$$

$$\Delta\varphi = 2\pi f_c \Delta\tau \Rightarrow \Delta\varphi = 2\pi f_c \left(\frac{2\Delta d}{c}\right) \Rightarrow \Delta\varphi = \frac{4\pi\Delta d}{\lambda} \tag{3.10}$$

In practice, the radar transmits 2 or more consecutive chirps, each with a time duration of T_c. Each chirp reflection is processed to obtain the range from the radar to the target object, using the FFT. This will result in peaks with the same frequency but with different phases. Therefore, these measured phase differences correspond to the spacial motion of the target object moving at a velocity v during the time period T_c [41, 43]. Thus, the movement of the target object is given by 3.11. Then, by substituting it into 3.10, the velocity can be estimated using 3.12.

$$\Delta d = v * T_c \tag{3.11}$$

$$v = \frac{\lambda}{4\pi T_c} * \Delta\varphi \tag{3.12}$$

When there is only one moving target object or when there are multiple moving target objects at different ranges from the radar, the velocity estimation method described before performs great using only 2 consecutive chirps. When there are multiple equidistant target objects with different velocities there is a need to use more than 2 consecutive chirps, considering that the FFT of 2 chirps would just yield a single peak whose frequency would correspond to the range, but whose phase change would present a combined signal from all of these target objects at the same range [41]. In this case, a sequence of equi-spaced chirps is transmitted, known as "frame" or "chirp frame". After the FFT is performed, the phase of each peak across all chirps in the frame is different as it incorporates phase contributions from all of the equidistant target objects [41]. Performing another FFT across this discrete sequence of chirps results in peaks corresponding to normalized angular frequencies of each target object velocity that can be used to calculate the velocities by substituting the phase difference with this discrete angular frequency [41, 43], in 3.12. This second FFT is often referred to as "Doppler-FFT". In Fig. 3.9 it is possible to observe the previously described process using a frame composed of M chirps and N samples per chirp. The first M x N matrix contains the raw radar data, then the first FFT is performed on each column of the matrix to estimate the ranges and finally the second FFT is performed across the matrix rows to estimate the velocities [41].

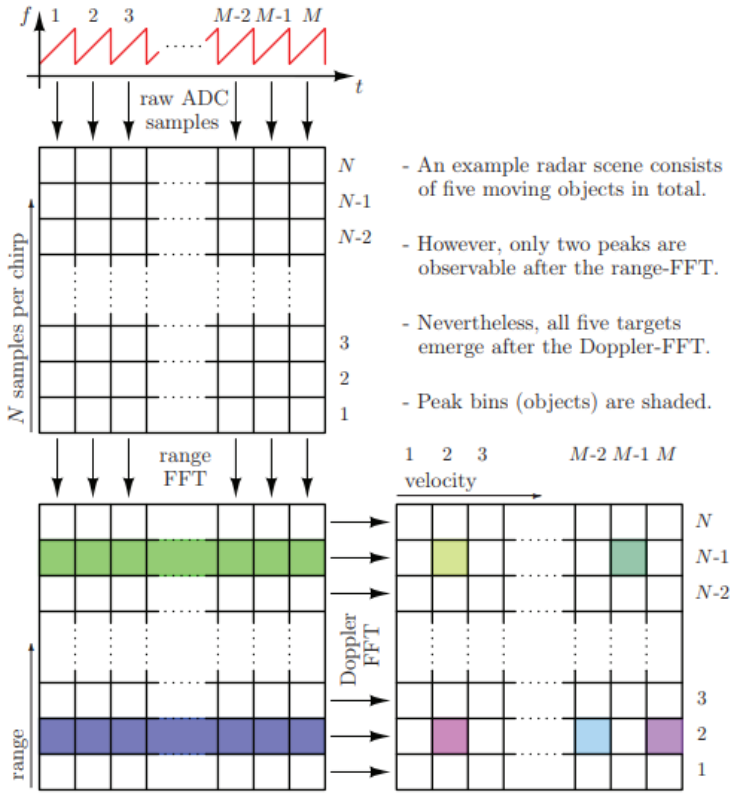


Figure 3.9: 2D FFT processing of a frame containing M chirps, where N samples are taken out each chirp. [Figure extracted from [41]]

The number of chirps that go in a frame, the number of frames used, as well as their periodicity, are all configured according to the specific detection scenario, and will be later explained in the chirp programming section.

3.1.5 Velocity Resolution

Just as with the range estimation, velocity estimation is also limited when it comes to detect 2 close peaks in the Doppler FFT spectrum. Velocity resolution, v_{res}, is, in other words, the smallest velocity change that the radar system is able to detect. According to the theory of discrete Fourier transforms a sequence of M chirps can resolve discrete angular frequencies that are separated by more than $2\pi/M$ radians per sample [41]. Analytically, 2 distinct normalized frequencies can be resolved as long as $\Delta\varphi > 2\pi/M$ [41]. So, having the previous in mind and taking in consideration 3.12, the velocity resolution can be computed using 3.13.

$$\Delta v = \frac{\lambda}{2MT_c} \tag{3.13}$$

Therefore, the resolution is inversely proportional to the number of chirps in a frame. In order to improve the velocity resolution one has to increase the number of chirps in a frame.

3.1.6 Angle Estimation

Angle estimation refers to the estimation of the angular position of a target, on a given plane, in relation to the radar system. In order to do the angle estimation it is necessary to have at least 2 RX antennas. These RX antennas need to be separated by a known distance, which will therefore create an additional traveling distance for the echo EM wave to reach the second RX antenna after reaching the first RX antenna. This results in two RX signals with a phase shift between them, which can be used to calculate the Angle-of-Arrival (AoA) of the reflected EM wave and hence the angular position of the target.

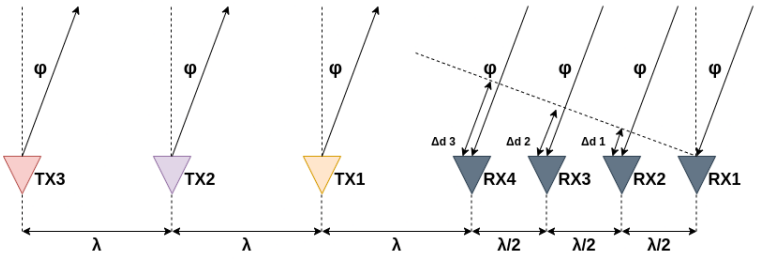


Figure 3.10: AWR1843 antenna configuration diagram.

Fig. 3.10 shows the antenna configuration used in the AWR1843BOOST radar sensor. It considers the antenna configuration as it is specified in its technical datasheet [44], and it will be used to explain how the angle estimation is performed in this case. In this diagram λ is the distance from TX1 to RX4 and $\frac{\lambda}{2}$ is the distance between each RX antenna, taking into consideration that λ is inversely proportional to the radar's operating frequency, and is, in this case just a few millimeters. If a target is placed in front of the radar at a range x and at an angle φ, the additional distance (Δ_d) traveled by the EM wave in relation to RX1, caused by the incident angle, can be calculated using (3.14), (3.15) and (3.16), for RX2, RX3 and RX4 respectively. Note that, since the EM wave reaches RX1 first, the distance from the target to RX1 antenna will be just x, or, in this case and to be more practical, the phase of the received signal will be 0.

$$\Delta_d 1 = [\frac{\lambda}{2}] * \sin\varphi \tag{3.14}$$

$$\Delta_d 2 = [2 * \frac{\lambda}{2}] * \sin\varphi \tag{3.15}$$

$$\Delta_d 3 = [3 * \frac{\lambda}{2}] * \sin\varphi \tag{3.16}$$

Subsequently, the traveled distances from TX2 to each RX antenna will be the same as the ones calculated for TX1 plus an additional $\lambda * \sin\varphi$ (additional traveled path caused by the distance between TX1 and TX2), and the traveled distances from TX3 to each RX antenna will be the same as the ones calculated for TX1 plus an additional $2 * \lambda * \sin\varphi$ (additional traveled path caused by the distance between TX1 and TX3). Since the EM waves reflected from the target will reach each RX antenna at a different time or in a more practical term with a different phase, because they will travel an additional distance to get to each RX, the angle at which the target is can be easily computed. The phase difference between two RX antennas is given by 3.17, where RX_d is the distance between RX antennas (represented in Fig. 3.10 as Δ_d), φ is the incident angle of the EM wave and λ is the wavelength of the transmitted signal. The AoA can then be estimated using 3.18.

$$\omega = \left(\frac{2\pi}{\lambda}\right) RX_d \sin\varphi \tag{3.17}$$

$$\theta = \arcsin\left[\frac{\omega\lambda}{2\pi RX_d}\right] \tag{3.18}$$

3.1.7 Angle Resolution

Angle resolution is the ability that the radar system has to distinguish two closely placed target objects at the same range, instead of detecting it as only one object. Fig. 3.11 presents a scenario were two closely placed target objects are the same range from the radar system. Both target objects are at a range d from the radar and are separated by an angle φ, which consequently leads to a physical distance between target objects of A.

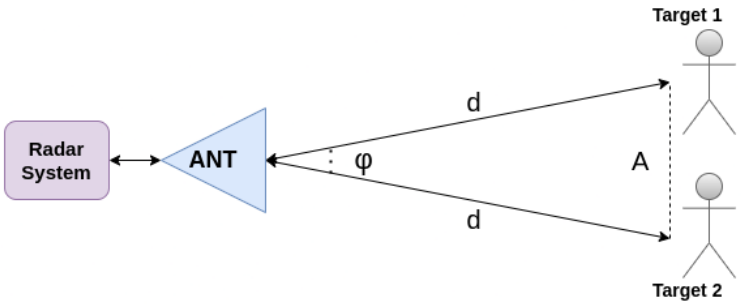


Figure 3.11: Angle resolution between two closely placed target objects at the same range from the radar.

Considering the given scenario, the angle resolution is therefore given by 3.19, where *NumVirtAnt* is the number of virtual antennas of the radar system, which depends on the number of

TX and RX channels that the radar system has. *NumVirtAnt = Number of TX channels x Number of RX channels*. The physical distance between target objects, A, is given by 3.20.

$$\varphi = \frac{2}{NumVirtAnt} \tag{3.19}$$

$$A = 2d \sin\left(\frac{\varphi}{2}\right) \tag{3.20}$$

A precise AoA estimation presupposes an extensive spatial sampling due to the Rayleigh criterion [45]. This can be achieved by a MIMO sensor with a widely spread virtual aperture [46]. Increasing the number of antennas results in an FFT with a sharper peak, thus, improving the accuracy of angle estimation and enhancing the angle resolution[47]. Fig. 3.12 shows the angle-FFT from two radar devices, one with four RX antennas and other with eight RX antennas (both with a distance between RX antennas of $\frac{\lambda}{2}$), where two point objects are placed at the same range, one at $\theta = -10^{\circ}$ and other at $\theta = 10^{\circ}$. As it is possible to see in the figure, the radar with only four RX antennas cannot resolve the two objects, while the radar with eight RX antennas can [47].

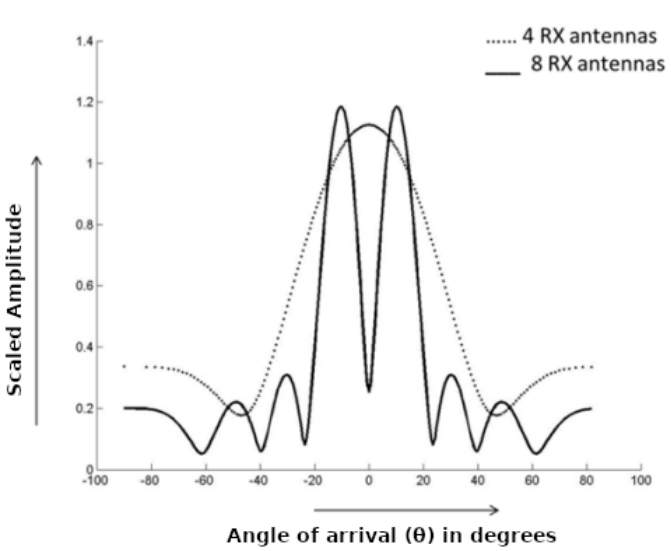


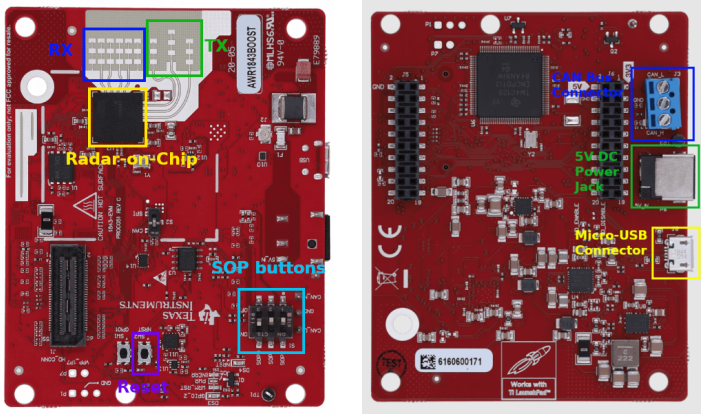
Figure 3.12: Angle resolution improves with increasing number of RX antennas. [extracted from [47]]

Therefore, in order to improve the angle resolution one has to increase the number of virtual antennas in the system, *i.e.*, the number of TX and RX channels.

3.2 AWR1843BOOST Evaluation Board

This section presents the most used radar sensor throughout this work, the AWR1843 evaluation board. The AWR1843BOOST, shown in Fig. 3.13, is an evaluation board that uses one of the latest radar-on-chip by TI, the AWR1843, which is described in section 2.3.1 on chapter 2. The AWR1843 is a FMCW radar sensor that covers both the 76-77 GHZ band and the 77-81 GHz band, and has 4 GHz of available bandwidth. The evaluation

board contains an antenna structure etched on its Printed Circuit Board (PCB), that has 4 antennas used for reception and 3 antennas used for transmission, in a MIMO configuration, which will be explained in the next section. This radar sensor can detect 4 properties of a target: it's range, it's velocity and it's angle in the azimuth and elevation planes. It has a maximum detection range of 100 m with a resolution of 85 cm, and detects targets with a velocity up to 60km/h with a resolution of 5km/h having a typical FoV of 30°. If resolution is a priority, the radar can be configured into a mode were detection range is up to 10 m with a resolution of 4 cm, and can detect targets with a velocity up to 10km/h with a resolution of 2km/h having a typical FoV of 120°. Finally, this evaluation board comes with the following interfaces: SPI, I2C, UART, CAN and LVDS. All of these specifications can be found in detail in the technical datasheet [44] as well as in the user guide [48].



(a) Front. (b) Back.

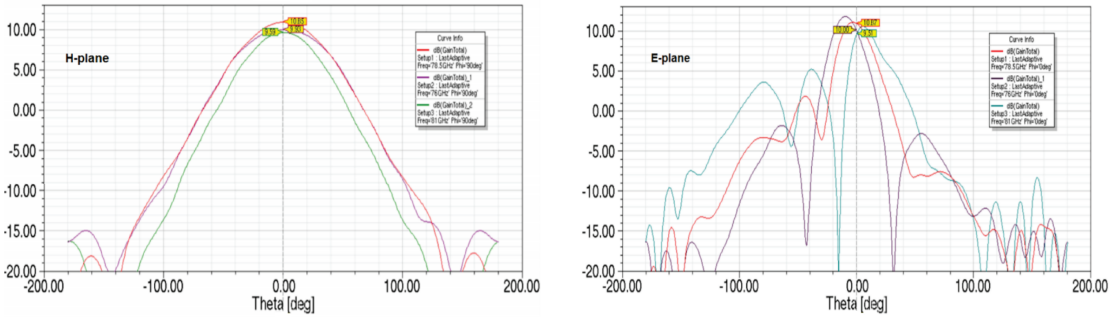
Figure 3.13: TI AWR1843BOOST evaluation board.

It is possible to see in Fig. 3.13 the main components in the evaluation board. Both antenna arrays and radar-on-chip are highlighted, as well as the reset and SOP buttons, which play a crucial role during the flashing of the main code to the processor. On the back it is also possible to see the CAN bus, USB and power supply connectors.

The AWR1843 antenna structure, shown in 3.15, provides the radar 120° degree field-of-view in the azimuth plane and 30° degree field-of-view in the elevation plane. This can be observed, roughly, by looking at the radiation patterns of the antennas, which are presented in Fig. 3.14, where they cross the 0 dB mark. It allows angle estimation in both planes, having a resolution of 15° in the azimuth plane and 58° in the elevation plane.

3.2.1 MIMO Configuration

4D MIMO radar emerged as a solution to cope with the drawbacks of the more conventional 3D radars, being now able to do precise measurements in both the azimuth and elevation planes. In a MIMO configuration a radar has multiple TX and RX antennas. By using a large number of TX and RX antennas, as shown in Fig. 3.15, 4D MIMO radars, in this case the AWR1843BOOST, are able to provide additional high resolution information about the targets by using the MIMO Virtual Antenna Array (VAA) concept, in which a virtual antenna is created in order to obtain a larger antenna aperture[49]. The VAA is determined by the spacing of antennas in both the TX and RX arrays, where the total number of elements is equal to the number of TX antennas multiplied by the number of RX antennas. Fig. 3.16 shows the diagram of the VAA in the case of AWR1843BOOST, where 3 TX and 4 RX



(a) Azimuth plane. (b) Elevation plane.

Figure 3.14: Radiation diagrams of the AWR1843BOOST antennas.

antenna arrays create a VAA of 12 virtual channels. The VAA concept has emerged as a promising beamforming technique in high-performance radar systems that are equipped with separate TX and RX antenna arrays [50].

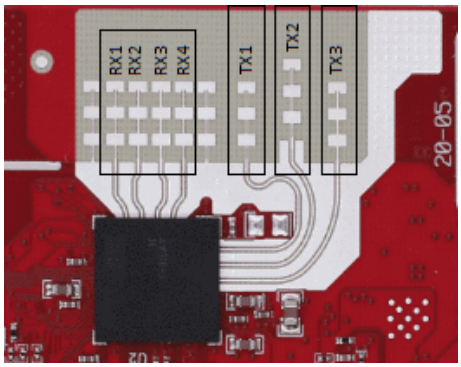


Figure 3.15: AWR1843BOOST antenna arrays.

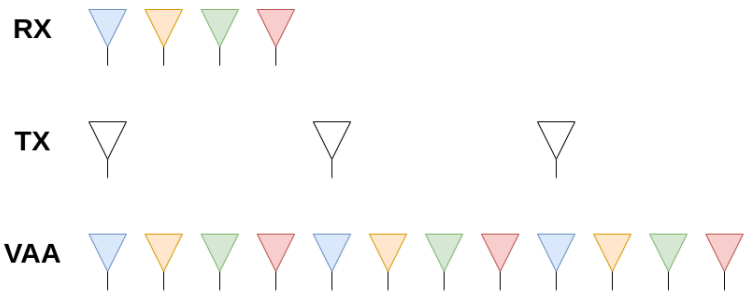


Figure 3.16: Virtual antenna array concept.

In a MIMO radar, the TX antennas transmit FMCW chirp sequences in a way that guarantees their orthogonality, and at each RX antenna the contribution of each TX antenna is extracted by exploiting waveform orthogonality [51]. The arrangement of a VAA is determined by the spatial convolution of the TX and RX arrays positions, and its aperture is the sum of each antenna aperture [52]. Furthermore, MIMO radars can synthesize a VAA with a large aperture using only a small number of TX and RX antennas, an advantage that has been exploited by almost all major automotive suppliers in their different types of radar, such as SRR, MRR and LRR [13, 51–55]. This can be observed for example in Fig. 3.17, where it shows the antenna arrays of a commercially used automotive radar, in this case

the Bosch FR5CPEC front radar, and it is possible to see that the number of elements is quite larger in comparison to the number of elements in the AWR1843BOOST, despite the fact that both radars have 3 TX and 4 RX channels. As demonstrated in section 3.1.7, to improve the angular resolution the number of virtual antennas in the system has to increase, in other words, the angular resolution depends on the aperture size, and in Table 3.1 it is presented a comparison between AWR1843BOOST and Bosch FR5CPEC to highlight the improvements made by MIMO VAA with a higher number of elements. It is possible to see that both the resolution and precision are considerably improved. Note that since the Bosch FR5CPEC radar uses the 76-77 GHz frequency band and therefore only has 1 GHz of bandwidth, the AWR1843BOOST values regarding range resolution and accuracy used for comparison belong to the operation on the same frequency band, 76-77 GHz.

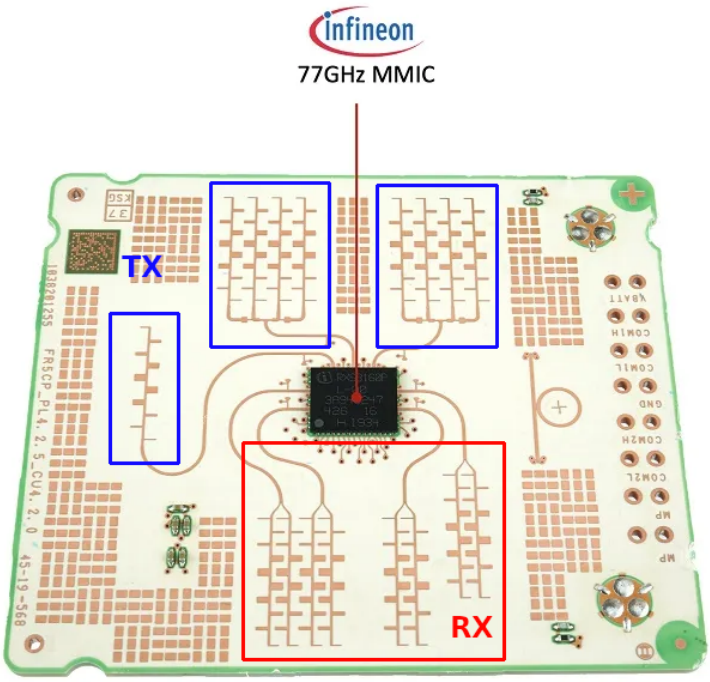


Figure 3.17: Bosch FR5CPEC front radar antenna arrays.

3.2.2 Radar Configuration Principles

To configure the radar to meet our requirements, we need to send several commands. Typically these commands are sent sequentially and are stored in a configuration file, which is a generic preference file that stores settings or configuration information and has the .cfg file extension. Fig. 3.18 shows the typical appearance of the commands stored in a TI mmWave radar configuration file that was used for the radar 360° measurements. Table 3.2 presents the parameters in which the chirp was configured with said configuration file, which results in the radar detection with the capabilities presented in 3.3. In Fig. 3.19 it is possible to see how these values impact the chirp configuration.

Each of these commands configures one particular aspect of the radar system and they are described/explained in A following the order of appearance in the configuration file shown in Fig. 3.18. All of the command values allowed for the normal functioning of the radar

```
sensorStop
flushCfg
dfeDataOutputMode 1
channelCfg 15 7 0
adcCfg 2 1
adcbufCfg -1 0 1 1 1
lowPower 0 0
profileCfg 0 77 7 3 39 0 0 100 1 256 7200 0 0 30
chirpCfg 0 0 0 0 0 0 0 1
chirpCfg 1 1 0 0 0 0 0 4
chirpCfg 2 2 0 0 0 0 0 2
frameCfg 0 2 32 0 100 1 0
guiMonitor -1 1 1 1 0 0 1
cfarCfg -1 0 2 8 4 3 0 15.0 0
cfarCfg -1 1 0 4 2 3 1 15.0 0
multiObjBeamForming -1 1 0.5
calibDcRangeSig -1 0 -5 8 256
clutterRemoval -1 0
compRangeBiasAndRxChanPhase 0 1 0 1 0 1 0 1 0 1 0 1 0 1 0 1 0 1 0 1 0 1 0 1
measureRangeBiasAndRxChanPhase 0 1. 0.2
aoaFovCfg -1 -90 90 -90 90
cfarFovCfg -1 0 0.25 8.64
cfarFovCfg -1 1 -7.06 7.06
extendedMaxVelocity -1 0
CQRxSatMonitor 0 3 11 121 0
CQSigImgMonitor 0 127 8
analogMonitor 0 0
lvdsStreamCfg -1 0 0 0
calibData 0 0 0
sensorStart
```

Figure 3.18: Typical appearance of the commands in a TI mmWave radar configuration file.

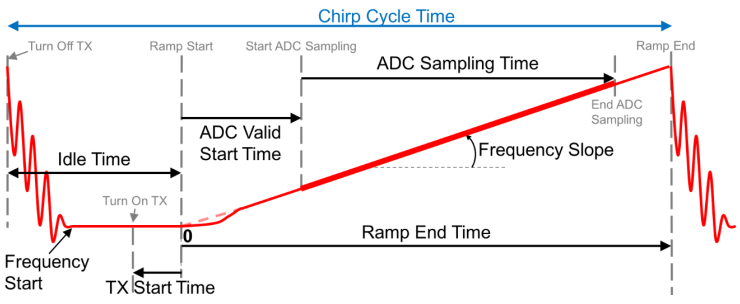


Figure 3.19: Chirp configuration specifications.

Parameter	AWR1843BOOST	Bosch FR5CPEC
Range accuracy	- m	0.1 m
Range resolution	0.85 m	0.2 m
Velocity accuracy	- m/s	0.05 m/s
Velocity resolution	0.56 m/s	0.1 m/s
Azimuth FoV	120°	120°
Azimuth angle accuracy	- °	0.1°
Azimuth angle resolution	15°	3°
Elevation FoV	30°	30°
Elevation angle accuracy	- °	0.2°
Elevation angle resolution	58°	6°

Table 3.1: Parameter comparison between AWR1843BOOST and Bosch FR5CPEC.

system are presented in the particular device datasheet and in the doxygen documentation, which can be accessed in the following directory `mmwave_sdk_<ver>/packages/ti/control/mmwavelink/docs/doxygen/html/index.html`, where `mmwave_sdk_<ver>` corresponds to the location of the used mmWave Software Development Kit (SDK).

So in order to create a configuration file one has to introduced the presented commands with the respective values according to the application in use. This approach is, however, time consuming and requires for the user to have a deeper knowledge on the commands or have the radar-on-chip user guide and datasheet in hand. Nevertheless, it is possible to generate a configuration file using the mmWave Sensing Estimator from TI [1].

3.2.3 Data Output Structure

TI radar sensors such as the AWR1843BOOST send their output data with the Type-Length-Value (TLV) encoding scheme. The type is the tag identifier that is used to identify each data packet, the length depends on the number of detected objects and varies from frame to frame, and the value carries the detected objects information. This data is then packed into a payload structure that is sent via UART in every frame. Fig. 3.20 shows the data structure as sent from the radar, with each packet being identified with a tag. The packets are sent as specified, during the configuration, in the command "guiMonitor", explained in 3.2.2. The data is then read and parsed using MATLAB or python scripts.

3.2.4 Radar Calibration

In this section the calibration process will be explained with more detail. The full calibration process is also presented in the doxygen documentation, which can be accessed in the following directory `mmwave_sdk_<ver>/packages/ti/control/mmwavelink/docs/doxygen/html/index.html`, as explained in the previous section, 3.2.2.

[1] `https://dev.ti.com/gallery/view/mmwave/mmWaveSensingEstimator/ver/2.3.0/` [Accessed on the 28th of September of 2023]

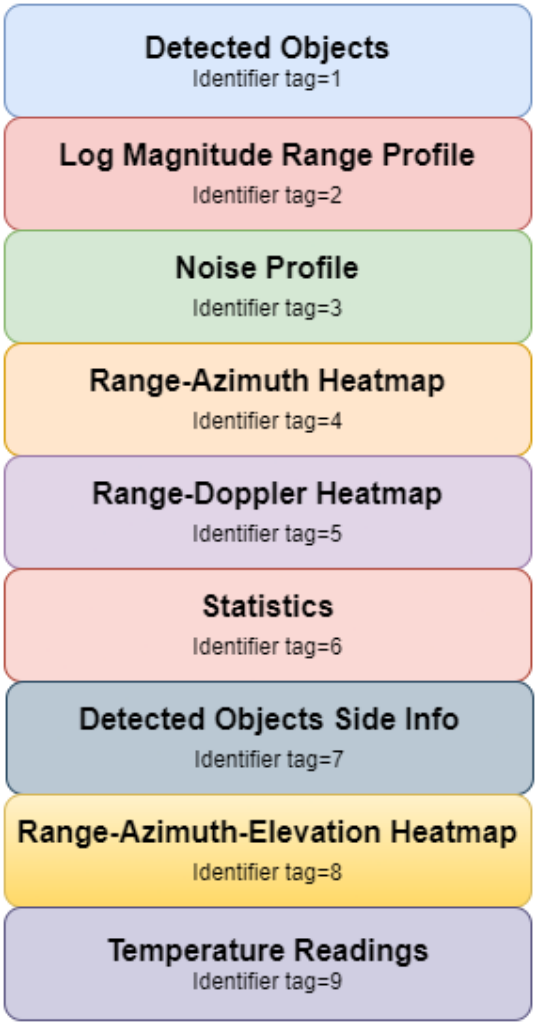


Figure 3.20: Output data structure.

Parameter	Value
Start Frequency	77 GHz
Frequency Slope	100 MHz/μs
Sampling Rate	7.2 Ms/s
Number of Samples	256
Number of Chirp Loops	32
Idle Time	7 μs
ADC Valid Start Time	3 μs
Ramp End Time	39 μs
Frame Periodicity	100 ms
Chirp Time	35.556 μs
Active Chirping Time	3.74 ms
Chirp Repetition Period	138 μs

Table 3.2: Chirp configuration parameters as configured using the file presented in Fig. 3.18.

Parameter	Value
Maximum Range	8.6 m
Range Resolution	4.2 cm
Maximum Velocity	6.87 m/s
Velocity Resolution	0.43 m/s

Table 3.3: Radar detection capabilities as configured using the file presented in Fig. 3.18.

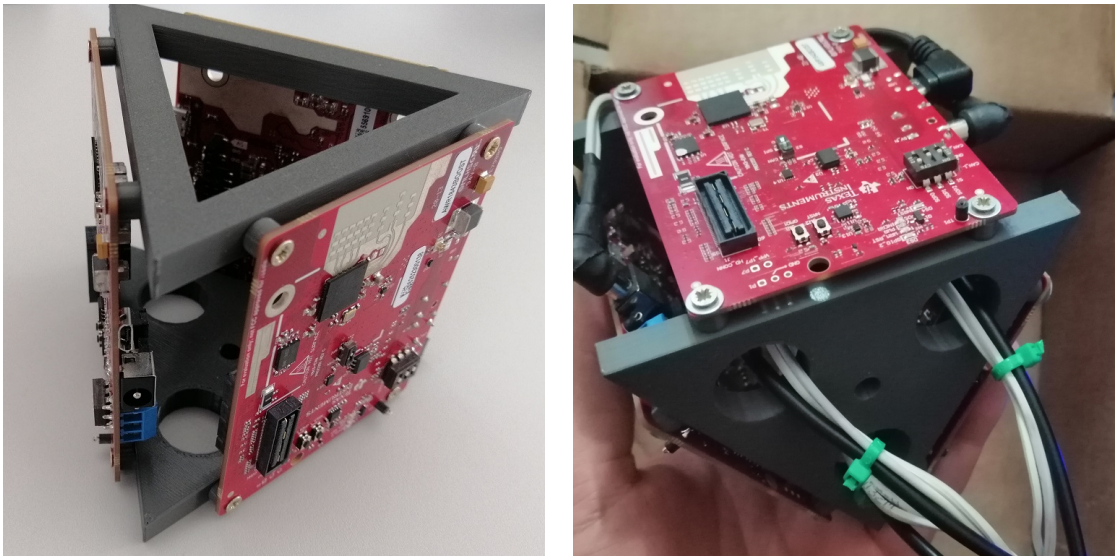
Because of imperfections in antenna layouts on the board, RF delays in SoC, etc, there is the need to calibrate the sensor to compensate for bias in the range estimation and receive channel gain and phase imperfections. TI mmWave radar sensors, such as the AWR1843BOOST, have a calibration function within their firmware. When the calibration measurement is enabled during the start configuration, the radar system assumes that a strong target, such as metallic corner reflector, is placed at boresight at a range of X. Afterwards the radar system does a peak search around the range X with a search window D, i.e. the peak is searched between -D/2 + X and X + D/2, in order to compute the associated error in the range and angle estimations and to provide a more precise and accurate estimation.

If the user wants to calibrate the radar he needs to enable the calibration measurement via the "measureRangeBiasAndRxChanPhase" command in the configuration file. This can be done by setting the enable calibration measurement to '1', following the insertion of the strong target range and search window. Therefore the command sent for calibration is "measureRangeBiasAndRxChanPhase 1 X D". After the calibration measurement is

concluded, the radar sends through the serial port the "compRangeBiasAndRxChanPhase" command with the range bias, receive channel gain and phase imperfections, which, for the AWR1843BOOST, is comprised of 25 values, the first being the range bias and the next 24 being 12 pairs of I (In-Phase) and Q (Quadrature) compensation coefficients, 1 pair for each virtual antenna, as explained before. Finally, the "compRangeBiasAndRxChanPhase" command sent from the radar via serial, with the compensation coefficients, needs to be copied to every radar configuration file in order for the calibration to be applied, and the "measureRangeBiasAndRxChanPhase" command needs to be altered in order to avoid a new calibration every time the radar is configured. It is only necessary to change it to "measureRangeBiasAndRxChanPhase 0 X D" and the calibration measurement will be disabled.

3.3 360° Radar - Prototype

This section presents the 360° radar prototype. It consists of a triangular structure that holds in place three AWR1843BOOST radar sensors. The structure is based on a equilateral triangle and was designed and 3D printed using Polylactic Acid (PLA), and it can be seen in Fig. 3.21.



(a) (b)

Figure 3.21: Radar 360° first prototype.

Since the triangular structure is equilateral, and each radar sensor has a field of view of 120° in the azimuth plane, it is possible to obtain 360° of field of view by placing the three radars in this triangular arrangement. In Fig. 3.22 it is possible to observe the geometry of the radar 360° prototype (the FoV of each radar is illustrative).

This prototype is sought to improve the 4D imaging radar state-of-the-art by creating a 360° point-cloud, including velocity and Signal-to-Noise Ratio (SNR) information of the targets. The radar 360° sensor can be mounted on the top of a vehicle in order to capture its surroundings. This type of setup is quite common for driver data collection or autonomous vehicle testing, such as in [56] for example, but normally with 360° lidars being used instead of radars. Although the implementation of the radar 360°, or a lidar 360° for that manner, on the top of a vehicle might be impractical as a final product, the 3D 360° point-clouds

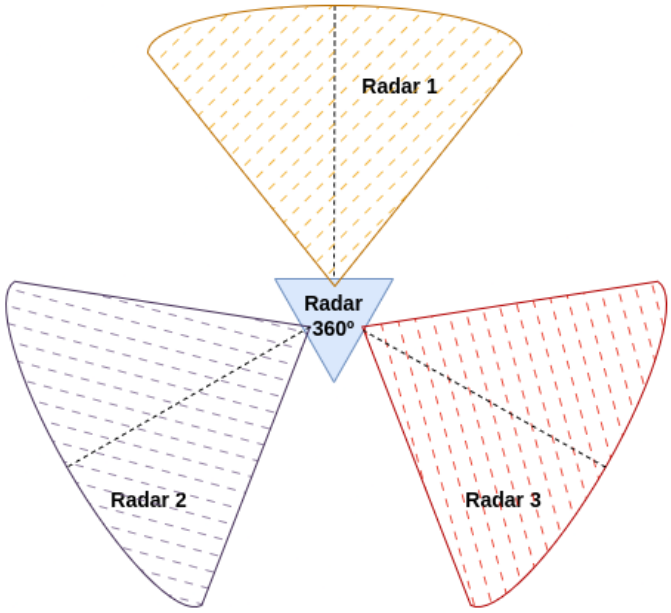


Figure 3.22: Radar 360° geometry.

are useful as input training datasets for object classification and recognition algorithms used by ADAS and ADS. In a car it is more common to use the radars separately in different locations instead of being all mounted in one spot. But nevertheless, this prototype serves as a proof of concept and can be used in other types of vehicles, such as UAV, like drones.

The radars are connected via USB to a computer, which receives the radar data using the UART protocol. The data is received and parsed using Matlab and Python scripts. The received point-clouds from each radar include the 3D coordinates in Euclidean space [range (y), azimuth (x) and elevation (z)] from all detected objects, as well as their velocity and SNR. The range and azimuth values then undergo a multiplication by a rotation matrix, shown in 3.21, in order to transform them to a panoramic 360° point-cloud. The elevation values do not need to undergo any multiplication since the height of the detected objects is not affected regardless of each radar position.

$$\begin{bmatrix} \cos(\theta) & -\sin(\theta) \\ \sin(\theta) & \cos(\theta) \end{bmatrix} \begin{bmatrix} x \\ y \end{bmatrix} \tag{3.21}$$

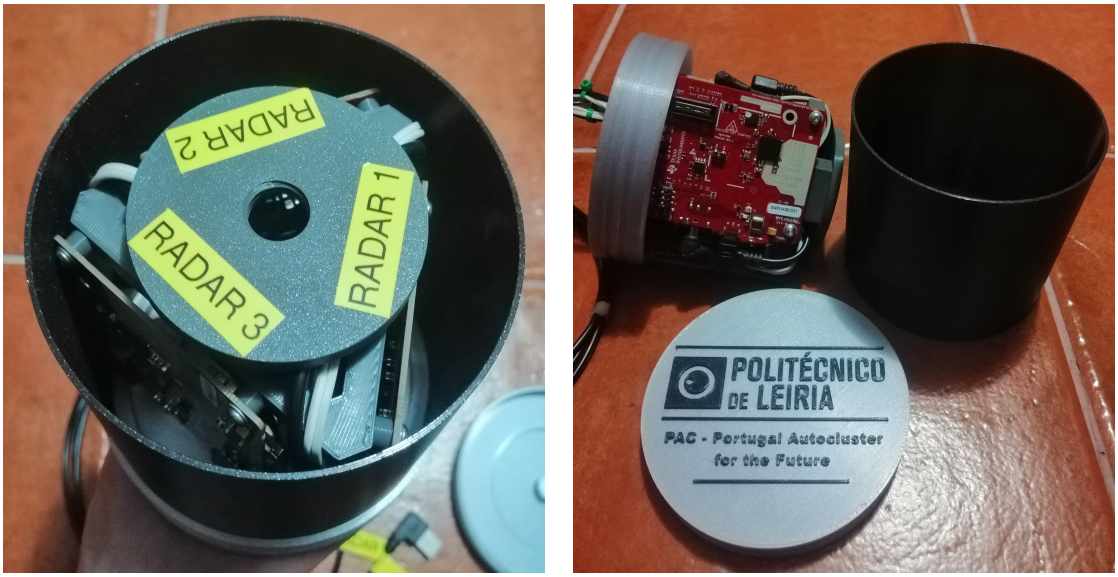
The θ angle used in the rotation matrix corresponds to the angle offset between the reference radar and the radar from where the objects were detected. The azimuth (x) and range (y) new coordinates are therefore given by 3.22.

$$\begin{bmatrix} x\cos(\theta) - y\sin(\theta) \\ x\sin(\theta) + y\cos(\theta) \end{bmatrix} \tag{3.22}$$

The reference radar was chosen as the radar 1, therefore the x and y coordinates from objects detected by radar 2 will undergo a multiplication by the rotation matrix with a $\theta = 120°$, while the x and y coordinates from objects detected by radar 3 will undergo a multiplication

by the rotation matrix with a θ = -120°. At last, all of the coordinates are stored in a single structure and then displayed as a 360° point-cloud.

To conclude this section, a radome was designed and 3D printed using Polyethylene Terephthalate Glycol (PETG). PETG was used this time because it is more resistant to thermal degradation, more thermally stable and more flexible than PLA [57], which is more suitable for this application given the fact that the electronics from the radar sensors heat up quite a bit and also because of the exposure to sunlight/heat. This radome is sought to shield the radar 360° from the elements. A radome (a portmanteau of radar and dome) is a structural, weatherproof enclosure that protects a radar sensor antenna [58]. It protects and conceals the mmWave antennas and electronics from external environment effects such as rain, sunlight, wind and dust, providing a structural weatherproof enclosure [59]. The radome is constructed to be electromagnetically transparent so that it minimally attenuates the EM signal transmitted or received by the antennas [59]. In order for a radar sensor to perform flawlessly it is critical to ensure that the radome or housing is designed to minimize electrical and environmental interferences to the radar sensor antennas [59]. The authors in [59] present a guide that provides an insight on radome design while taking in consideration the radar sensor performance. The radar 360° radome was designed based on the concepts addressed on this design guide, and it can be seen in Fig. 3.23 and 3.24. Although this is not the main scope of this work, a brief explanation on radome design will be addressed here since one was designed. The most important aspects in radome design and performance that one can take from [59] are the radome wall thickness, the antenna to radome distance, the shape of the radome, the relative permittivity of the material used for the radome as well as the frequency used by the radar.



(a) (b)

Figure 3.23: Radar 360° with the disassembled radome structure.

The radome wall thickness plays a key role in achieving the optimum performance as it is of the most importance to ensure that the radome wall thickness is equal to an integer multiple of the radar wavelength/2, so that the radome becomes "nearly transparent" for the mmWave frequency range [59]. The optimum radome wall thickness (t_o) can be calculated using equation 3.23, where n is an integer (1,2,3...), c is the speed of light, f is the radar



Figure 3.24: Radar 360° with the fully assembled radome structure.

frequency (79 GHz in the case of AWR1843BOOST for 77-81 GHz bandwidth) and ε_r is the relative permittivity of the material.

$$t_o = \frac{n}{2} * \frac{c}{f * \sqrt{\varepsilon_r}} \tag{3.23}$$

In order to get the optimal radome wall thickness, using 3.23, it is necessary to know the relative permittivity of the material that is going to be used, in this case PETG. In [60], the author performed an EM characterization of several 3D printed materials, with PETG being one of them. The measurement was performed in the W-band, from 75 to 110 GHz (which includes the used 76-81 GHz automotive frequency band), using a 3 mm thick piece of PETG, resulting in a relative permittivity with a mean value of 2.7. Having this value and using 3.23, one can calculate the optimal wall thickness of the radome, which is given in 3.24.

$$t_o = \frac{1}{2} * \frac{3 * 10^8}{79 * 10^9 * \sqrt{2.7}} \approx 1.16mm \tag{3.24}$$

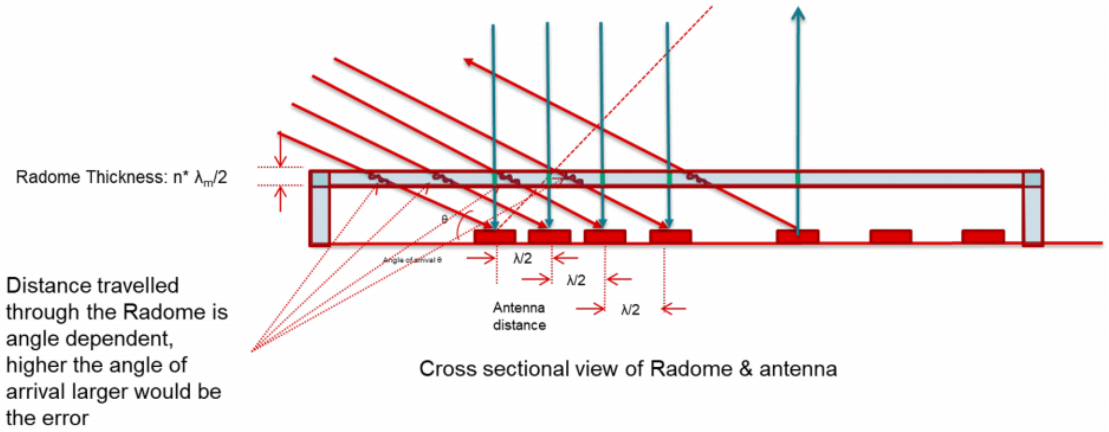
The optimal distance between the radar antenna and the internal surface of the radome helps to minimize the effects of reflections caused by the radome, and these effects become minimal if the EM waves returning to the antenna are in phase with the transmitted ones [59]. This optimal distance can be calculated using 3.25, where n is, once more, an integer (1,2,3...) and λ_0 is the wavelength, in air, of the transmitted signal.

$$d_o = \frac{n * \lambda_0}{2} \tag{3.25}$$

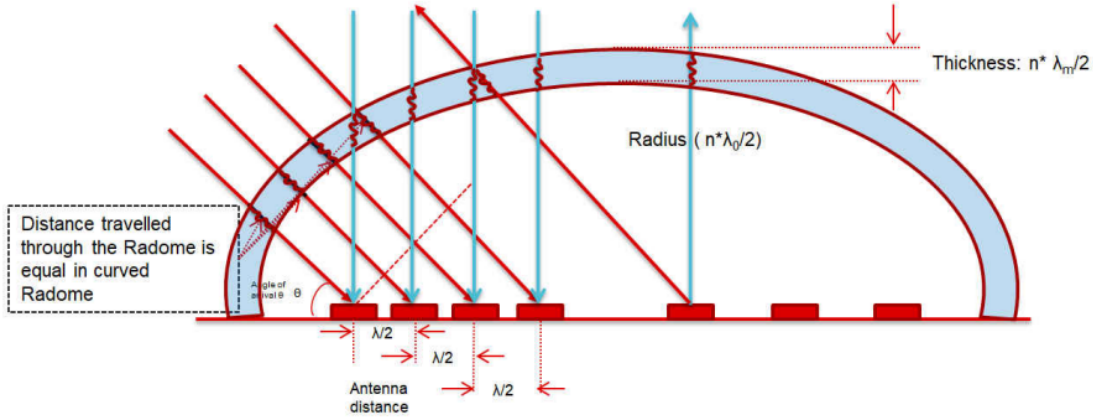
To meet some of the geometrical constrains imposed by the radar 360° prototype, 9 was used as the integer n. So, the optimal distance between the antenna and the radome is given by 3.26.

$$d_o = \frac{9}{2} * \frac{3 * 10^8}{79 * 10^9} \approx 17mm \tag{3.26}$$

Finally, the shape of the radome needs to be taken into consideration. Depending on the type of radome, the distance traveled in the radome material can be angle dependent [59]. For a rectangular radome the traversed radome wall would be larger at higher grazing angles, while in a curved radome, both at boresight and at higher grazing angles, the distance traveled through the radome is the same, therefore, the angle dependent error would be lower [59]. This issue is presented in Fig. 3.25, where it possible to observe that in a rectangular radome the waves travel more distance through the wall at grazing angles than in a spherical radome. This becomes a problem when the traveled distance is greater than the optimal thickness, which will cause multiple reflections at the radome interface boundary resulting in ripples in the antenna radiation patterns and leading to nulls that can cause inconsistency in the detection of the objects at the higher grazing angles, which results in angle estimation errors [59]. Therefore, in order to avoid this issue, the radar 360° radome was designed having a spherical shape.



(a) Rectangular radome.



(b) Spherical radome.

Figure 3.25: Distance traveled in radome wall for different grazing angles. [Extracted from [59]]

3.4 Radar 360° - MATLAB Controlled Version

This section presents the working of the radar 360° where all of the radars are connected to the computer and are controlled through a MATLAB Graphical User Interface (GUI) that was created in order to interact and configure the radars, as well as for visualizing the point-cloud data. The GUI is comprised of 3 tabs, the first being for radar setup and configuration and the second and third for point-cloud data visualization and on-the-fly radar configuration. These tabs can be seen in Fig. 3.26, 3.27 and 3.28.

The first tab is where the user sets up all of the radars, as it can be seen in Fig. 3.26. Here is where the user inserts the COM ports that the radar uses for data transmission and configuration and also upload the configuration file to the radar. In this tab, the user can also calibrate each radar as well as enable/disable the clutter and DC removal, configure which type of CFAR detector for each radar to use and apply the CFAR threshold in dB. Lastly, there are two push buttons to start and stop the measurement. Fig. 3.27 presents the second tab of the GUI, which is where its possible to visualize the data point-cloud on a 3D perspective and also send on-the-fly commands to reconfigure the radar to meet the user's requirements. The user can also set the size of the visualization windows according to the measurement scenario that the radar is in and deactivate any radar if it is necessary. Lastly, Fig. 3.28 presents the third tab of the GUI, which is similar to the second tab, the only difference being the fact that the point-cloud is presented in a 2D perspective as seen from above.

This version has a downside however, which is the fact that MATLAB cannot read from multiple instruments/devices at the same time, it cannot read data from the 3 radars in parallel, thus it reads the data from the radars one by one, sequentially. This is not ideal, because it takes considerably more time by reading data from each radar, one by one, than if it were reading the data from the radars at the same time, in parallel/multi-threading. In order to cope with this issue, a new controlling architecture was designed, this time considering a dedicated hardware capable of multi-threading, with the goal to fix the sequential data reading and turn it into parallel data reading. This version is presented in the next section.



Figure 3.26: 1st tab of the radar 360° MATLAB GUI.

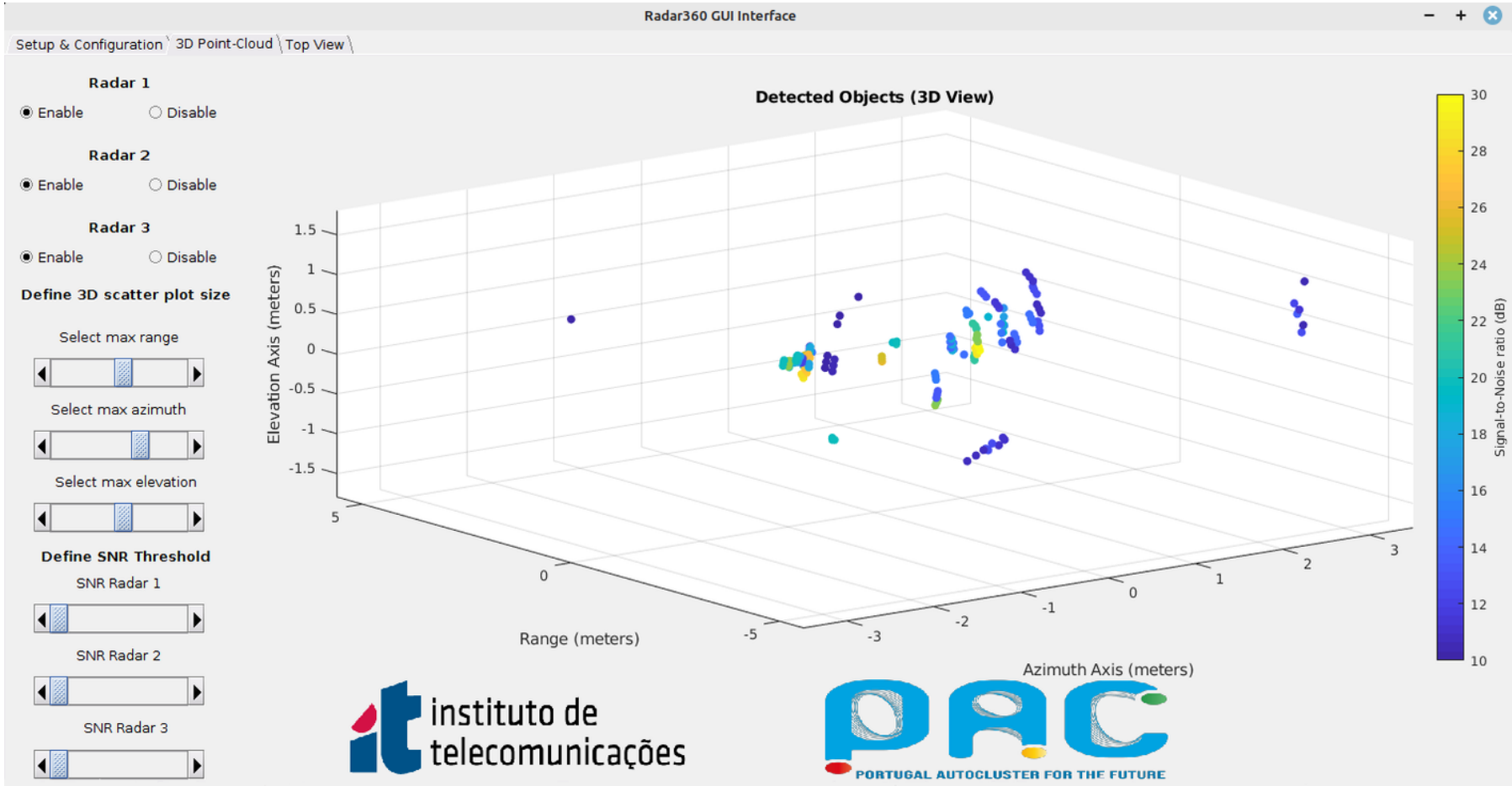


Figure 3.27: 2nd tab of the radar 360° MATLAB GUI.

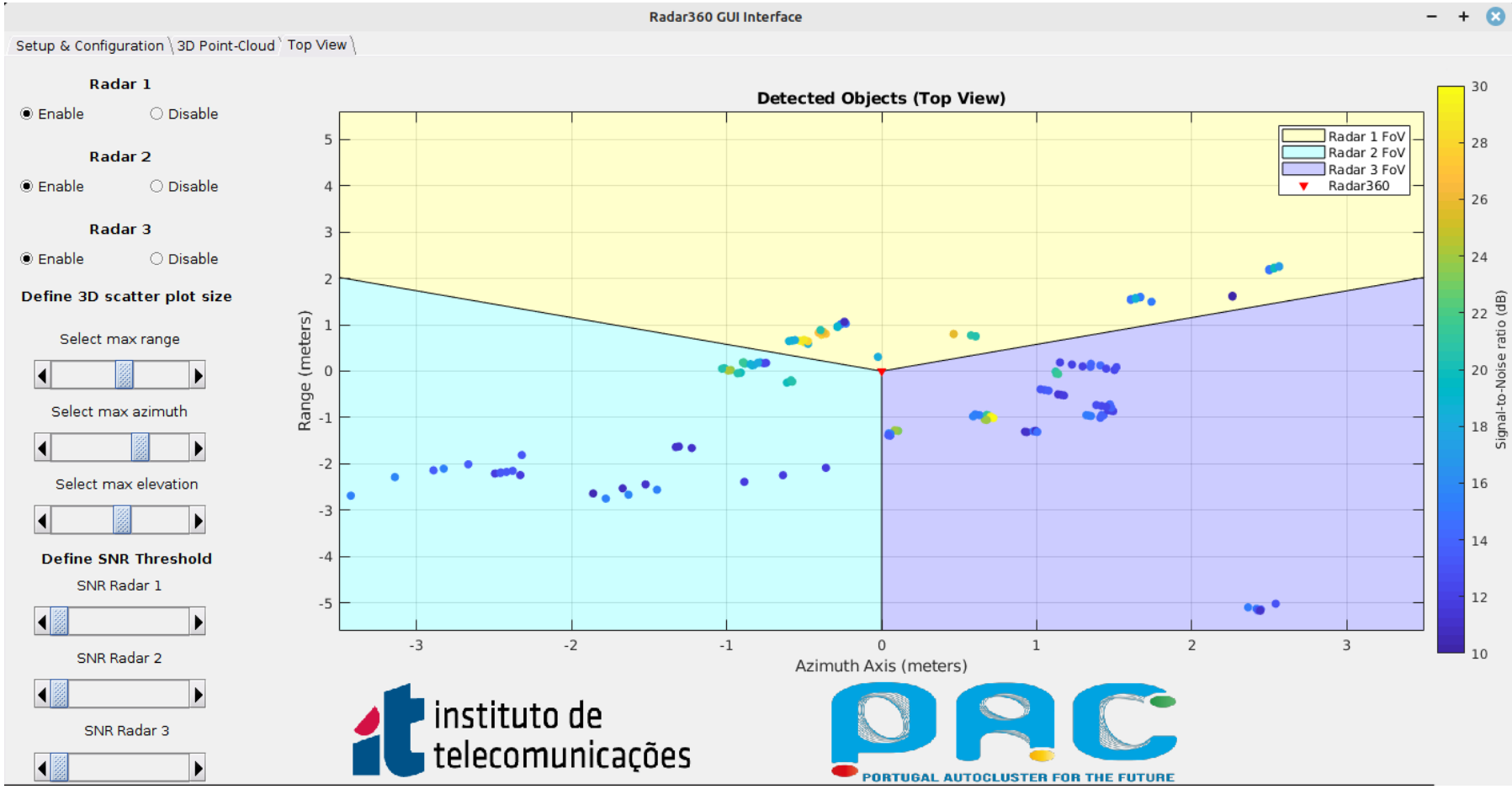


Figure 3.28: 3rd tab of the radar 360° MATLAB GUI.

3.5 Radar 360° - Dedicated Hardware Version

This section presents the working of the radar 360° where all of the radars are connected to the a small single-board computer, in this case a Raspberry Pi 3 Model B. The Raspberry Pi 3 Model B is an open source, Linux based, small single-board computer widely used in applications such has Industrial/Home automation, Robotics, Internet of Things (IoT), Web server and much more. It has a Broadcom BCM2387 SoC that features a 1.2 GHz Quad-Core ARM Cortex-A53 64bit Central Processing Unit (CPU), a Dual-Core VideoCore IV Graphics Processing Unit (GPU), 1GB of Random Access Memory (RAM), connectivity through BCM43438 wireless LAN and Bluetooth Low Energy (BLE), 40-pin extended General Purpose Input/Output (GPIO), 4 USB-2 ports, 1 10/100 BaseT Ethernet Socket, 1 Micro SD port for loading the Operating System (OS) and storing data, a HDMI connector as the graphical interface with a screen, etc. All of the detailed information about the Raspberry Pi 3 Model B can be found in the product brief [2].

In this architecture all of the data processing is done on the Raspberry Pi, where the configuration of the radars is also handled. As it is presented in Fig. 3.29, in this architecture the Raspberry Pi essentially serves as a dedicated processing unit that takes some of the heavy processing from the computer, which is only used for data visualization and radar configuration/control. The Raspberry Pi is connected to the computer through an Ethernet cable and using TCP protocol for communicating. In the computer the point-cloud data is received and then presented in graphs in a GUI, while the commands for radar configuration are sent from the computer to the Raspberry Pi according to the user's choices.

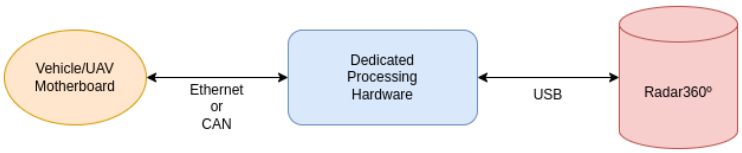


Figure 3.29: Radar 360° - Raspberry Pi version generic block diagram.

The main goal with this architecture is to have a very light OS running on the Raspberry Pi, preferably with no heavy graphics, managing the data processing scripts of the radars in parallel/multi-threading, so that the processed and parsed data is sent from the Raspberry Pi to the computer ready to be visualized through a GUI. By using a very light OS it is expected that the radar data processing is gonna be handled faster than when using just a computer, which has a lot of tasks running in background plus all of the heavy graphics that are inherent to a typical OS, be it Linux, Windows or MacOS. After some research on light OS's it was decided to use piCore, the Raspberry Pi dedicated OS by Tiny Core Linux, which is an independent system architected by Robert Shingledecker and now developed by a small team of developers with a strong community support. Tiny Core Linux is not a traditional distribution but a toolkit used to create a customized system that offers flexibility, a recent kernel and a set of applications that makes it ideal for a custom system such as this one. The concept behind piCore is that is runs entirely on RAM, boot media is not used after boot and there is no installation in conventional terms. The file system is in RAM and extensions are mounted to the file system read-only, thus changes are not saved over reboots so there's always a clean system after boot. Scripts and files, such as piCore extensions and libraries,

[2] `https://www.raspberrypi.com/products/raspberry-pi-3-model-b/` [Accessed on the 24th of January of 2024]

can be stored in a 2nd Linux partition in the micro SD card and be available during next boot, which is referred to as persistent storage or mounted mode. All of this information regarding piCore was taken from the Tiny Core team's website [3], [4] and also in [61].

In order to put the raspberry Pi running with the piCore OS the following steps were executed:

- **Download the piCore image** - The piCore OS can be downloaded using the following URL [5];
- **Burn the piCore image into the micro SD card** - To burn the piCore image in the micro SD card one can use a image writing software tool, like balena etcher [6];
- **Boot the raspberry Pi with piCore** - Having the piCore image burned in the micro SD card it is time to plug it on the raspberry Pi and power it on;
- **Manage the micro SD card partitions** - Since this OS runs completely from RAM and changes or new files are not stored in memory, if the user doesn't want to, it is important to understand the OS partitions, which are the following:
    1. /dev/mmcblk0p1 - This is the first partition and is of type Win95 FAT32 (VFAT). This partition contains the basic piCore system and the Raspberry Pi boot loader, firmware and other support files. This partition is unmounted during operation, and the system does not use it after the boot process gets completed;
    2. /dev/mmcblk0p2 - This is the second partition and is of type ext4. This partition is used for pre-installed extensions, such as python, tcp packet manager, ssh and other network tools and many more. However, the size of this partition is very small and it won't allow the installation of any additional extensions. This partition must be expanded in order to have enough free space for additional extensions, files and backups.
- **Expansion of the 2nd partition** -
    1. To manage the disk partitions the fdisk partitioning tool must be used, and started as root. This can be done using the command *sudo fdisk -u /dev/mmcblk0* or *sudo fdisk -u /dev/mmcblk0*;
    2. List the partitions, which can be done with the *'p'* command. Then the value of the starting cylinder of the 2nd partition must be saved;
    3. Delete the 2nd partition. This can be done using the *'d'* command and by entering 2 as the *Partition Number*;
    4. A new partition must then be created. This process can be done by using the *'n'* command and then select *'p'* for *Primary Partition* and 2 for *Partition Number*. Then the value of the starting cylinder must be used as the *First Cylinder*, as for the *Last Cylinder* the default value can be used;
    5. System reboot, which can be done using the command *sudo reboot*;

[3] `http://tinycorelinux.net/5.x/armv6/releases/README` [Accessed on the 24th of January of 2024]
[4] `http://tinycorelinux.net/concepts.html` [Accessed on the 24th of January of 2024]
[5] `https://distro.ibiblio.org/tinycorelinux/ports.html`
[6] `https://etcher.balena.io/` [Accessed on the 24th of January of 2024]

6. Expand the 2nd partition. After the system reboot and start up, the 2nd partition must be expanded. This can be done using the command *sudo resize2fs /dev/mmcblk0p2*.

The next step is to prepare the piCore OS to run the python scripts that configure and read data from the radar. Running python scripts in the piCore OS requires some extensions that are not available in the downloaded image, such as the python development environment and programming language, the python package installer (pip) and the package library *Numpy*, which are essential for a correct operation. All of these were installed using the following commands:

- Install the python development environment, using the command *tce-load -wi python 3.6.tcz*;
- Install the python programming language, using the command *tce-load -wi python-dev.tcz*;
- Install the nano text editor, using the command *tce-load -wi nano.tcz*;
- Install the python package installer, which requires the following commands to be executed:
    1. Create a directory for the pip extension, using the command *mkdir cd /home-/tc/pip3Persistent*;
    2. Go to the newly created directory, which can be done using the command *cd /home/tc/pip3Persistent*;
    3. Download a python script that uses bootstrapring logic to install python-pip, using the command *wget https://bootstrap.pypa.io/get-pip.py*;
    4. Run the previously downloaded script, using the command *sudo -H python3.6 get-pip.py*.
- Install the python package for scientific computing, *Numpy*, using the command *pip install numpy*.

All of the downloaded extensions will be stored in a temporary directory at */tmp/tce/* (tce stands for Tiny Core Extensions), which is created at each and every boot. The */tmp* directory will be lost when the system restarts or is shut down, and with it all of the files that it holds, since this OS stores almost everything in the RAM. To avoid this from happening it is necessary to make these changes "persistent", which essentially can be done by executing *filetool.sh -b* in the terminal prompt. This executes a script which provides the backup function that supports persistence, which, by default, stores the */home* and */opt* directories in a compressed archive at */etc/sysconfig/tcedir/mydata.tgz*, effectively making the changes permanent at every boot, since they are now stored in the 2nd partition of the microSD card.

Afterwards, the python scripts used for the radar configuration, data reading and processing were copied to the home directory of the piCore OS. Once there, the *filetool.sh -b* was executed again in order to permanently store them in the 2nd partition of the microSD card.

Finally, the last step in the system implementation was to make the main python script to automatically start after the OS startup. To do this it is necessary to change the *bashrc* file, which can be done according to the following commands:

1. Open the *bashrc* file with the nano text editor, using the command *sudo nano /.bashrc*;
2. Add /main.py to the end of the *bashrc* and then press "Ctrl + x" to exit the editor and save the changes at exit.

The main python script implements multi-threading, which makes the acquisition and data processing to be performed in parallel, in order to improve processing time and, in essence, perform just as a single radar. However, after the first tests and measurements, the results were not as promising as initially thought. The average processing time per iteration was slightly higher than the one observed using the MATLAB version. This eventually led for this architecture to be abandoned, at least for the moment. The processing time could be improved by using a newer version of the raspberry Pi, which has a finer hardware, or other small state-of-the-art supercomputer.

3.6 Measurements and Results

This section is going to present the practical implementation of the radar 360° and the measurements results.

3.6.1 Validation Measurement in a Static Scenario

In order to evaluate the proposed radar arrangement, the setup shown in Fig. 3.30 was assembled inside the anechoic chamber in order to reduce external RF and multipath interferences. The radar 360° was placed at the center of the anechoic chamber, at a height of 1.4m from the ground. Six 6 metallic poles, with a 7 cm of diameter and of 2 m of height, were distributed around the radar according to the geometry depicted in Fig.3.31 and 3.32. In the figure, the radar is illustrated as the red triangle. This served as the first measurement and initial validation of the radar 360° prototype.

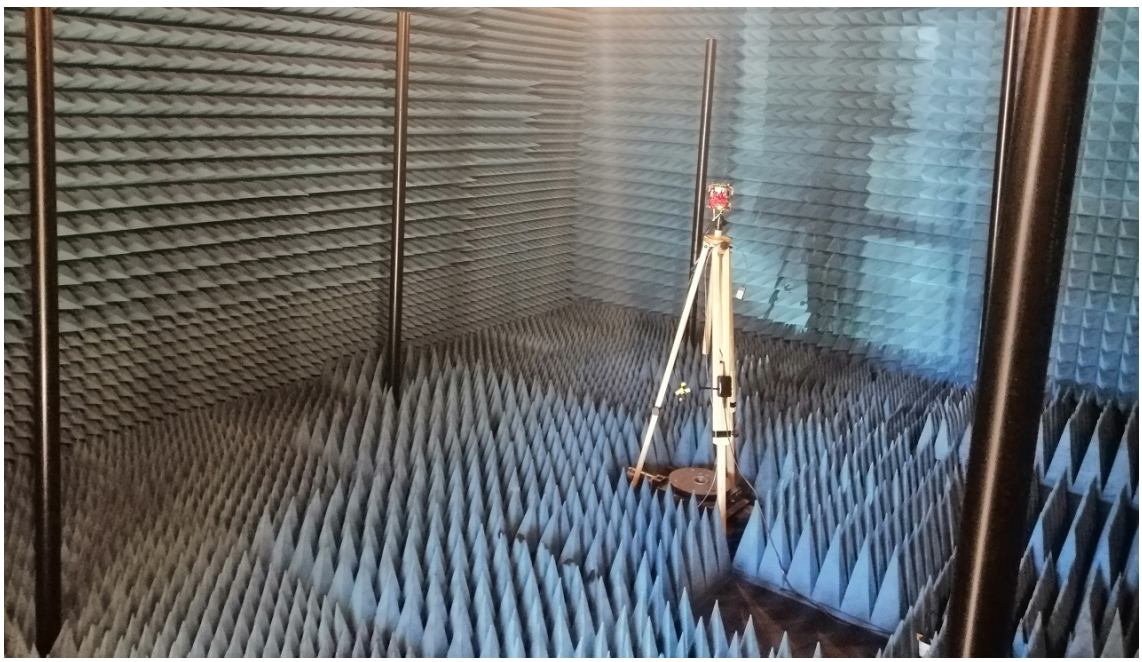


Figure 3.30: Setup inside the anechoic chamber.

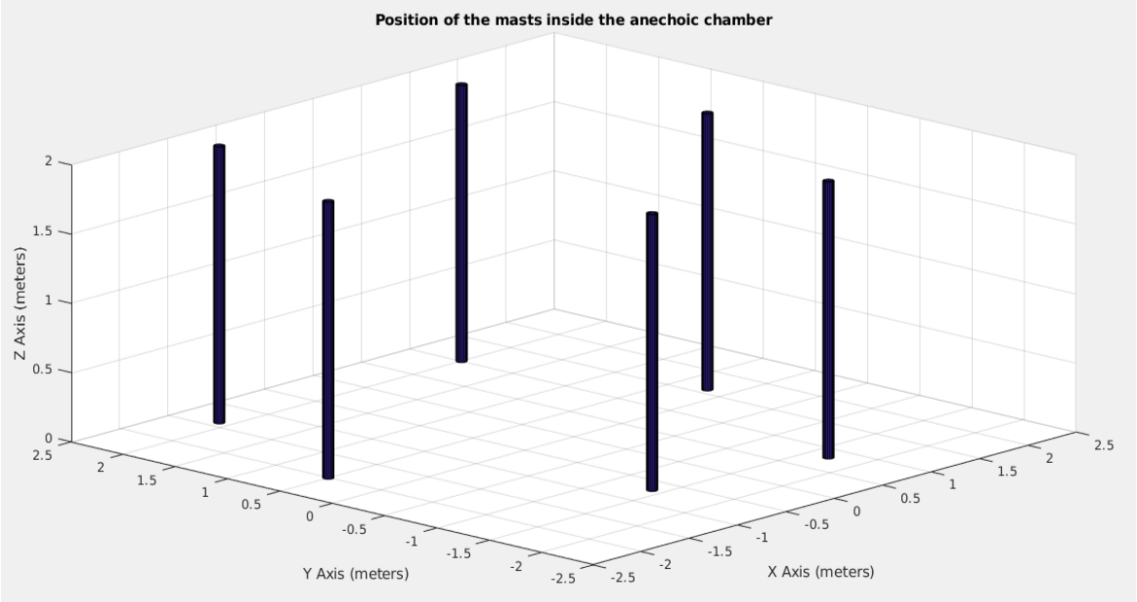


Figure 3.31: 3D perspective of the poles position inside the anechoic chamber.

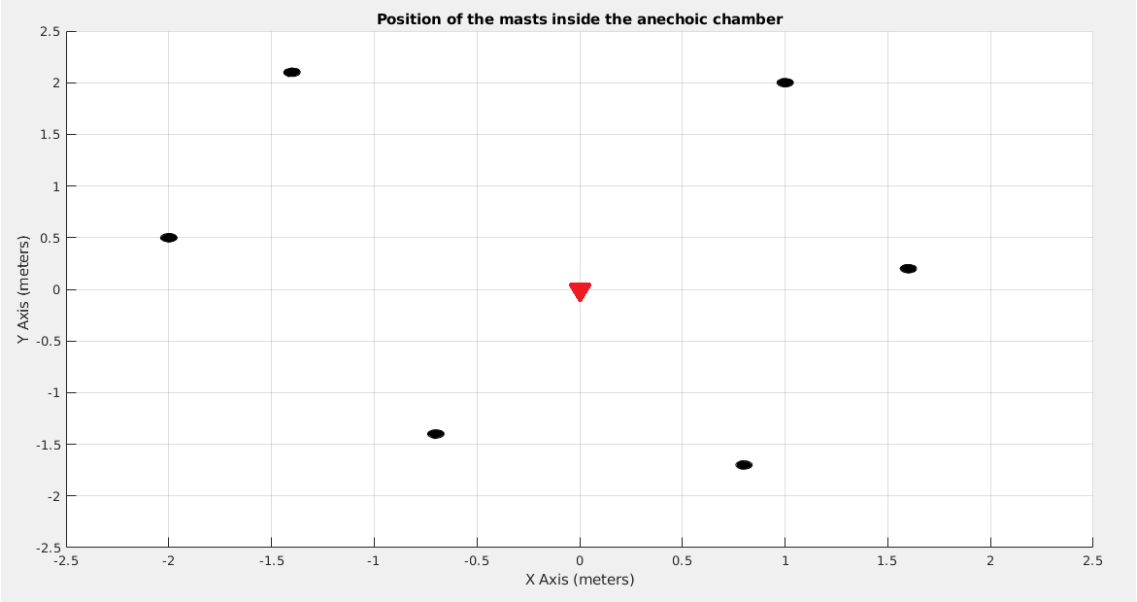


Figure 3.32: Top view of the poles position inside the anechoic chamber.

The radar 360° prototype was then tested in the scenario previously described. Ten radar acquisitions were obtained and its values averaged, in order to obtain a point-cloud of the poles. The calculated point-cloud can be seen in Fig. 3.33, where each point has a colour that is correlated with the SNR for that particular point. Next to the point-cloud scatter plot is the respective SNR colourbar, with values ranging from 10 to 30 dB. As it is possible to observe from the experiments, in Fig. 3.33 and 3.34, the resultant point-cloud is fairly good. In 3.4 it is presented the *x,y* coordinates of the metallic poles as well as the centroid coordinates of the detected point-cloud, in meters. The centroid is, essentially, the center of a set of points. In this case, the *x,y* coordinates of the points around each pole were averaged in order to find the respective centroids, so that they could be compared with the actual position of the poles. It is possible to see that some detected points are not exactly centered with the pole, and this as to do mainly with two circumstances. The first being the measurement of the exact positions of the poles, which was conducted using a meter measuring tape, which leaves room for some small error. The other being the error associated with the spacial precision of the radar, which in this case is 4 cm for the given 4 GHz of bandwidth. Another aspect that might draw the attention of the observer is the average height of the detected points, and this has to do with the fact that the radar is located at 1.4 m from the ground and has a maximum of 30° of field of view in the elevation plane, which is quite narrow at close range. These factors contribute to the average height of the detected points. Nonetheless, as it can be observed in the figures, all the poles are being detected.

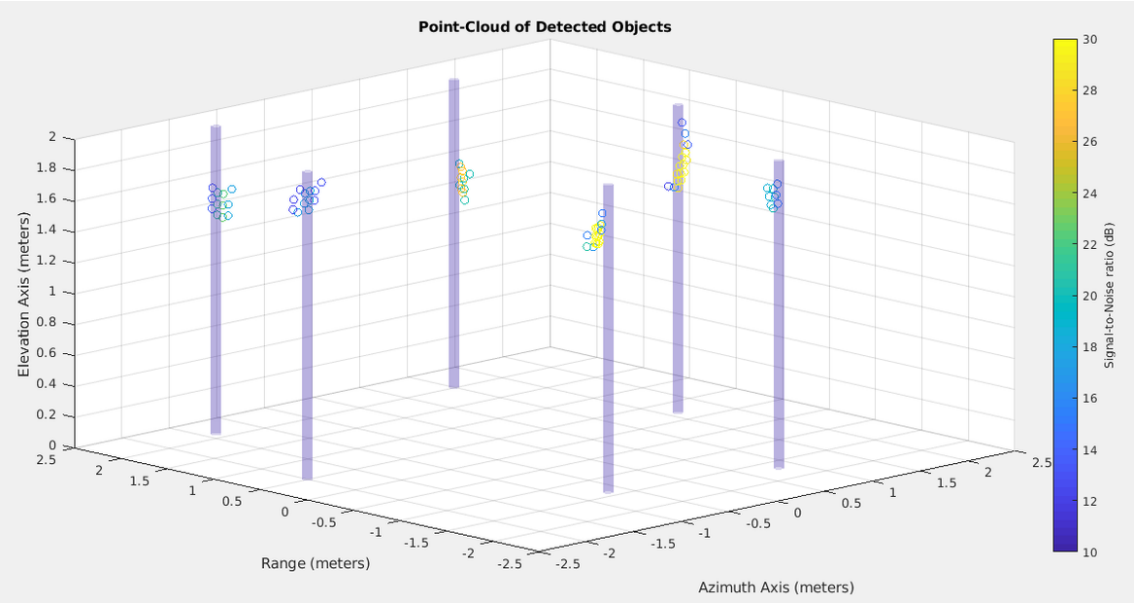


Figure 3.33: 3D perspective of the computed point-cloud scatter plots.

In this first measurement all of the target objects were stationary. This was obviously just a practical and first validation of the system in order to see how it behaved. In a real-world application it is very rare to get a scenario were all of the target objects are stationary, because real-world scenarios are dynamic, and especially in automotive applications were all of the possible target objects are almost certainly moving, such as cars, motorcycles, pedestrians, animals, etc. So, in order to test the radar 360° under those circumstances, the second measurement performed involved both stationary and moving objects.

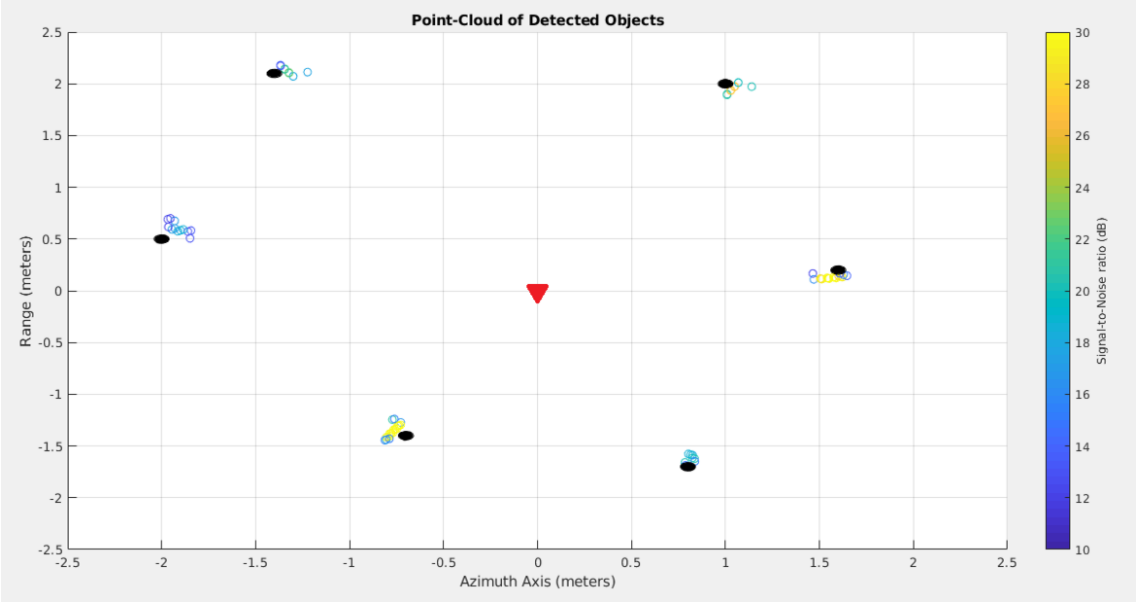


Figure 3.34: Top view of the computed point-cloud scatter plots.

Metallic poles	Coordinates	Centroid coordinates
Nº1	(1,2)	(1.12,1.96)
Nº2	(1.6,0.2)	(1.56,0.12)
Nº3	(0.8,-1.7)	(0.8,-1.62)
Nº4	(-0.7,-1.4)	(-0.8,-1.34)
Nº5	(-2,0.5)	(-1.9,0.58)
Nº6	(-1.4,2.1)	(-1.36,2.12)

Table 3.4: *x,y* coordinates of the metallic poles *vs.* point-cloud centroids, (in meters).

3.6.2 Validation Measurement in a Dynamic Scenario

The setup for the second measurement consists of 2 stationary metallic poles, just like the ones used in the first measurement, 1 stationary trihedral metallic reflector and me walking around the radar 360° with a smaller trihedral metallic reflector. There was no predefined trajectory for me to walk around the radar 360°, I just walked in a path that was cleared from the absorber foam in the anechoic chamber floor. The position of the poles for this measurement setup can be seen in Fig.3.35 and 3.36, while the radar 360° is represented by a red triangle at the center.

In this measurement a camera was used to record me walking around the radar 360°. This video was then split into frames and they were traced into their respective point-cloud scatter-plot using timestamps. This frame sequence captures me entering the anechoic chamber, moving the stationary trihedral reflector a little to the side, walking around the radar 360° back and forth and finally exiting the anechoic chamber.

Fig.3.37, 3.37, 3.37 and 3.37 present a series of frames taken from a video of me walking around the radar 360° with their respective point-cloud scatter-plots. In the scatter-plots, the poles and trihedral reflector are showcased inside red elipses, while the purple elipse

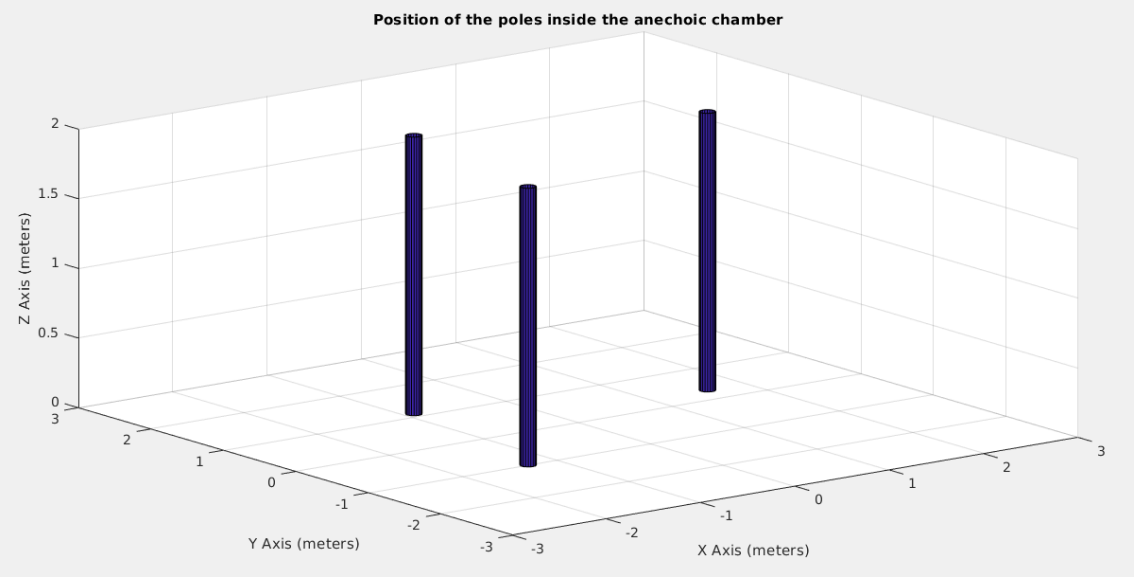


Figure 3.35: 3D perspective of the poles position inside the anechoic chamber.

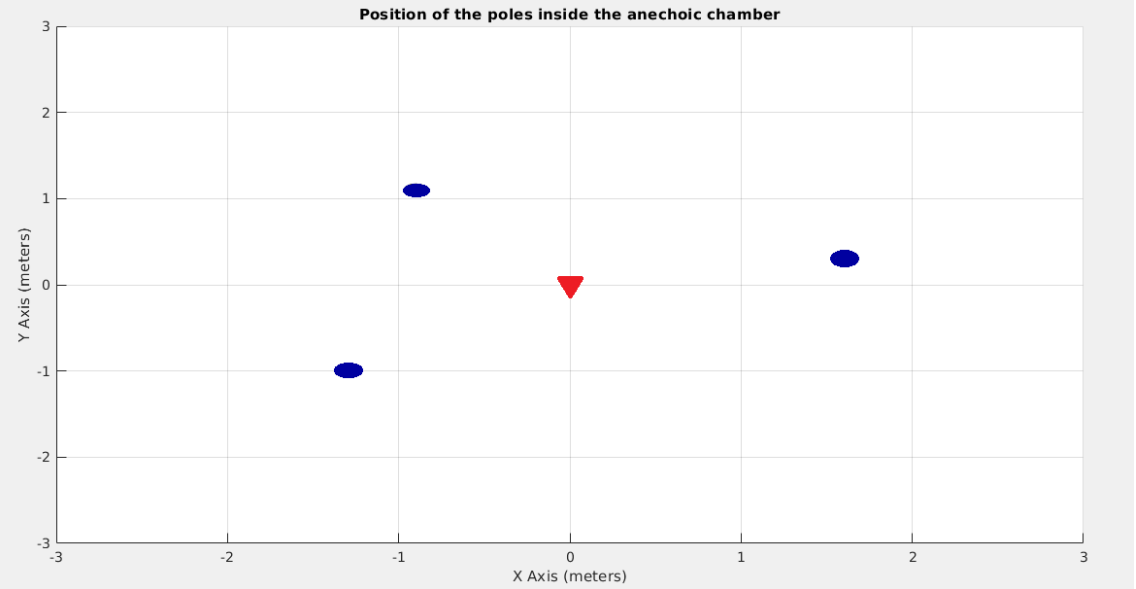
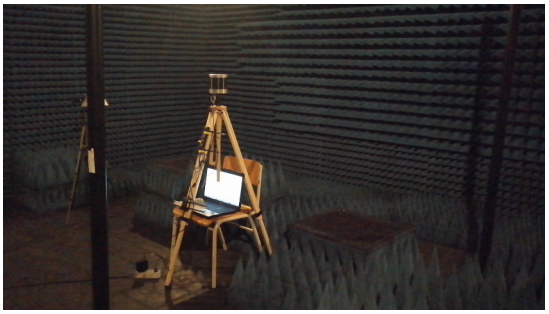
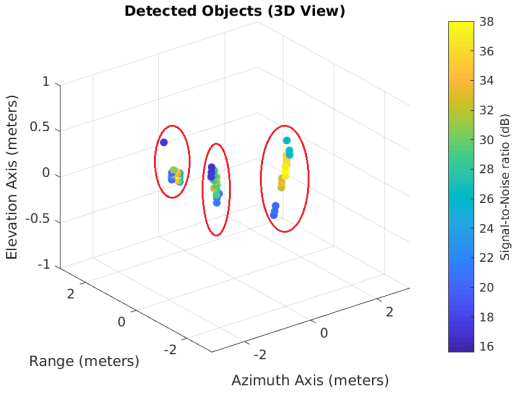


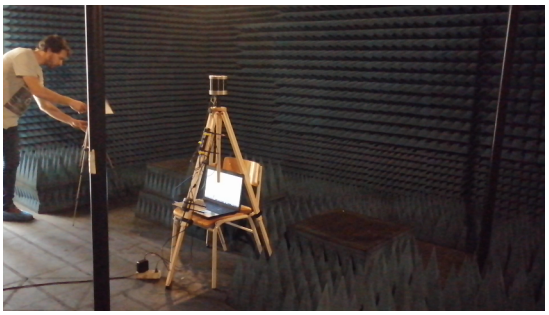
Figure 3.36: Top view of the poles position inside the anechoic chamber.



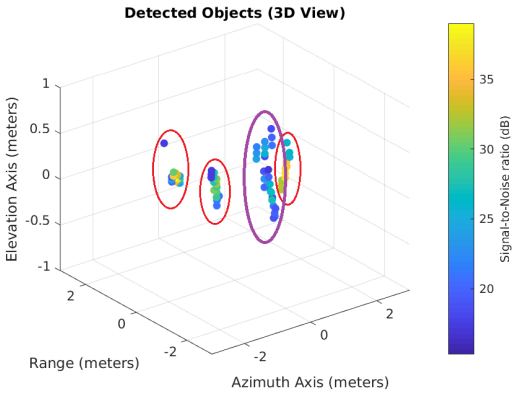
(a) Frame 1.



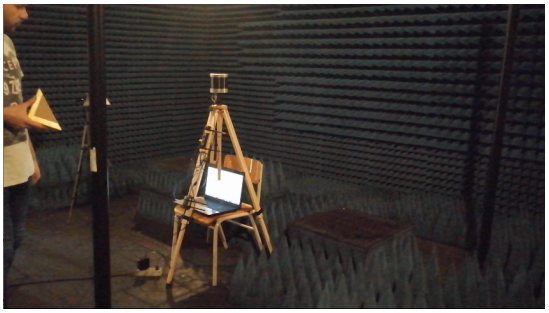
(b) 3D scatter-plot of frame 1.



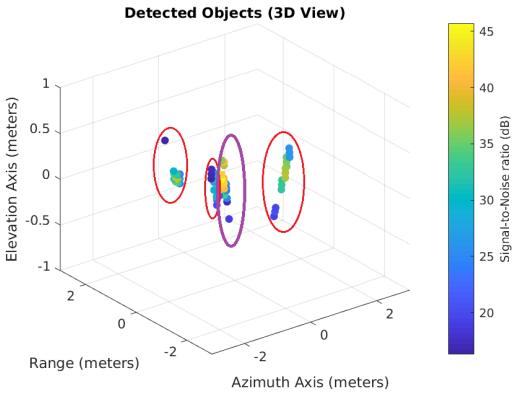
(c) Frame 2.



(d) 3D scatter-plot of frame 2.

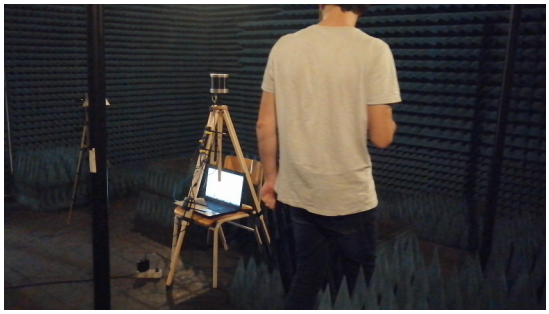


(e) Frame 3.

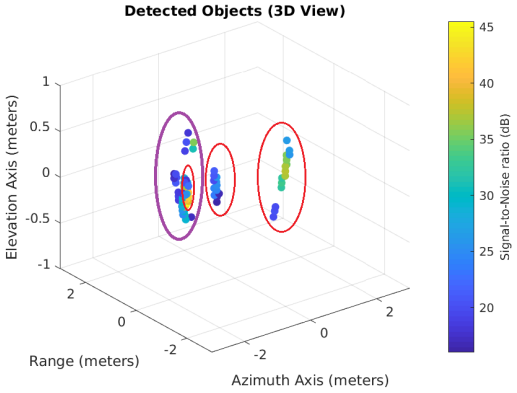


(f) 3D scatter-plot of frame 3.

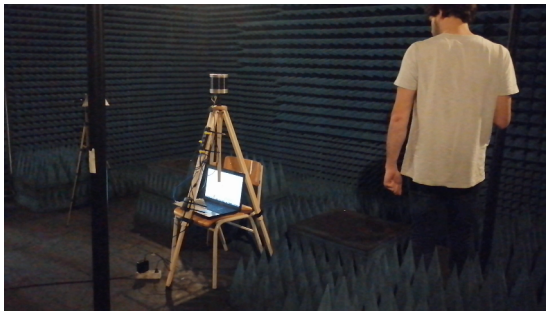
Figure 3.37: Sequence of frames from a video showing the detection of both stationary and moving targets.



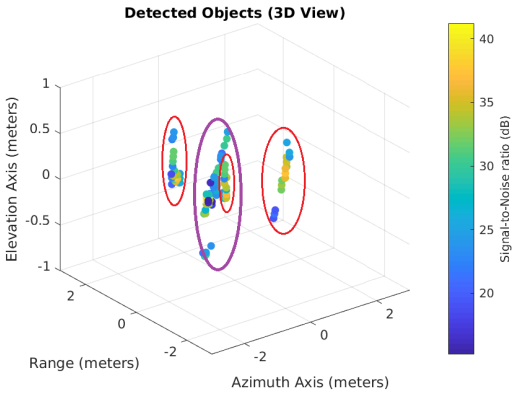
(g) Frame 4.



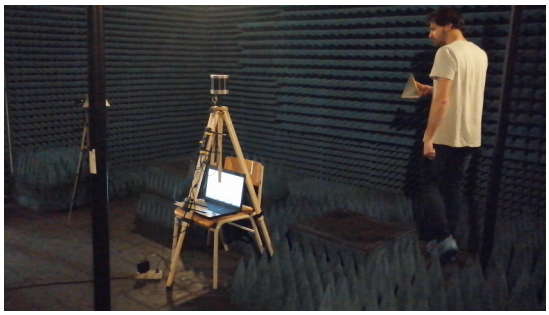
(h) 3D scatter-plot of frame 4.



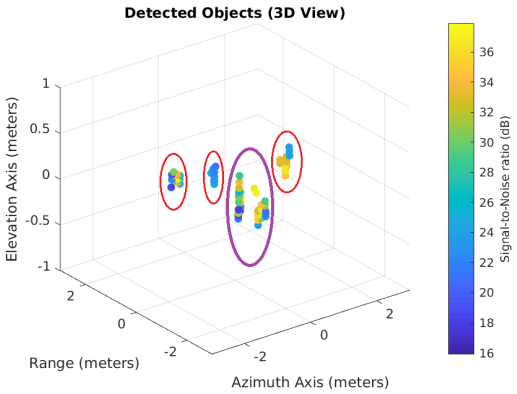
(i) Frame 5.



(j) 3D scatter-plot of frame 5.

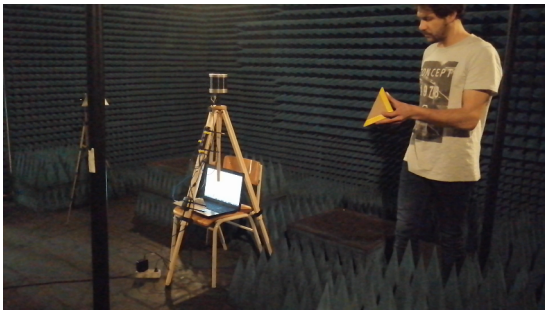


(k) Frame 6.

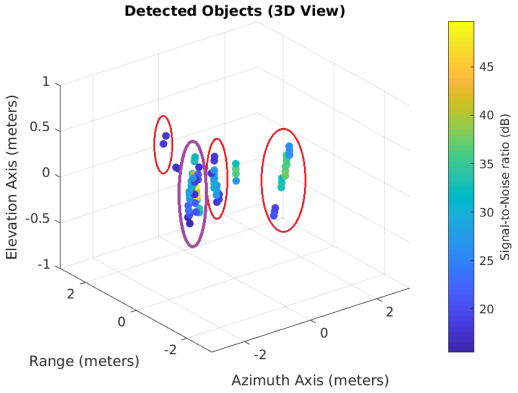


(l) 3D scatter-plot of frame 6.

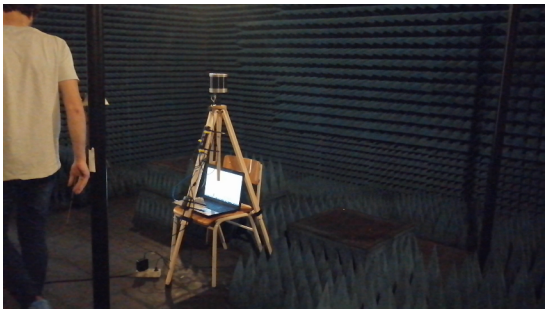
Figure 3.37: Sequence of frames from a video showing the detection of both stationary and moving targets. (cont.)



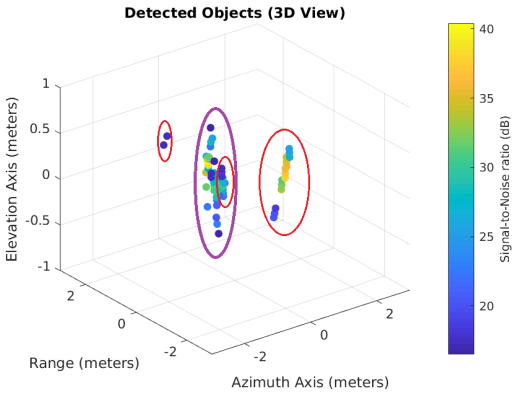
(m) Frame 7.



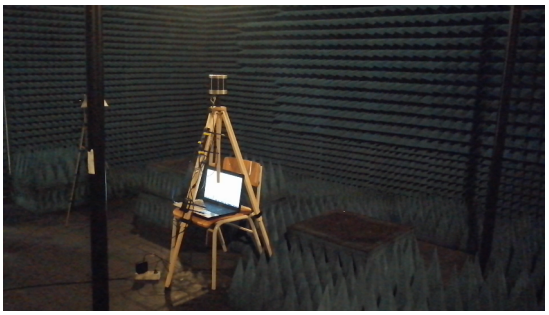
(n) 3D scatter-plot of frame 7.



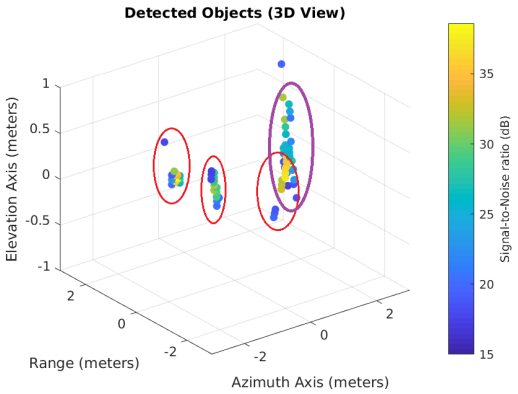
(o) Frame 8.



(p) 3D scatter-plot of frame 8.

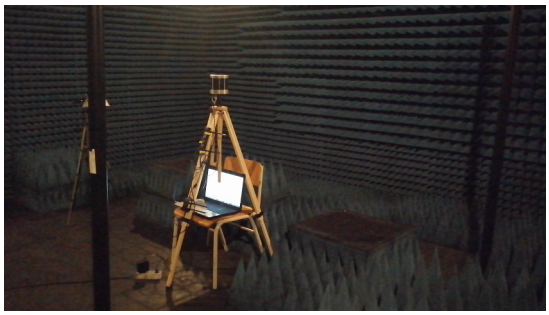


(q) Frame 9.

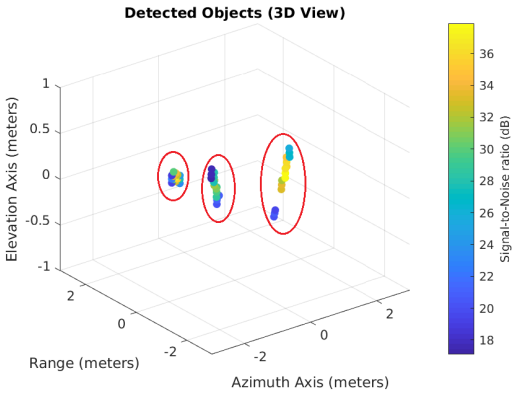


(r) 3D scatter-plot of frame 9.

Figure 3.37: Sequence of frames from a video showing the detection of both stationary and moving targets. (cont.)



(s) Frame 10.



(t) 3D scatter-plot of frame 10.

Figure 3.37: Sequence of frames from a video showing the detection of both stationary and moving targets. (cont.)

displays the moving target, in this case me. Unlike with the stationary poles measurement setup, in this case it is more difficult to calculate the detection error since my trajectory around the radar 360° was somehow limited due to the disposition of absorber foam in the anechoic chamber floor and because the movement of my legs and arms during a walk is almost impossible to predict and generates too many points in the point-cloud. Furthermore, since these frames were taken from a recorded video, its impossible to know my exact position in those frames. Overall, the stationary target objects are successfully detected and the points regarding my movement seem to follow my trajectory quite well. It is also possible to see that when I'm in front of the stationary target objects they seem to be almost blocked out from view, having only a couple of points left to identify them.

3.6.3 Integration with ADAS

To conclude this section, the results from the integration of the radar 360° with an ADAS/ADS software are presented. Autoware is an open-source software platform designed for autonomous driving applications. It provides a complete software stack for self-driving vehicles, encompassing key functionalities such as perception, localization, planning and control. Built on the Robot Operating System (ROS) framework, Autoware relies on it to interface with various sensors. Each sensor publishes data to a specific ROS topic, where different modules subscribe in order to process the sensor's information.

For demonstration purposes, in the final presentation of PAC project, the radar 360° was directly integrated with Autoware. Through python scripts, the radar 360° publishes the object detection data in ROS topics, which Autoware then subscribes to process for subsequent point-cloud visualization. As a final touch, a vehicle model and highway guidelines were added to the visualization plot in order to give a more realistic representation to the point-cloud data. In Fig. 3.38 it is shown the point-cloud plot of recorded data during the final presentation of PAC project. Highlighted in red, it is a blob of points which represent a person standing next to the radar 360°. The other detected points that can be seen represent people that were walking past our exhibition stand. Another aspect regarding this image is the several points that can be seen "inside" the vehicle, which as to do with the simple fact that the radar 360° was on a tripod in our stand instead of being mounted on top of the car, so in reality there were no vehicle boundaries to limit the persons from coming

closer to the radar. Nevertheless, it was highly valuable to integrate the radar 360° into a "real" system and explore its capabilities and functionalities, even if only for demonstration purposes.

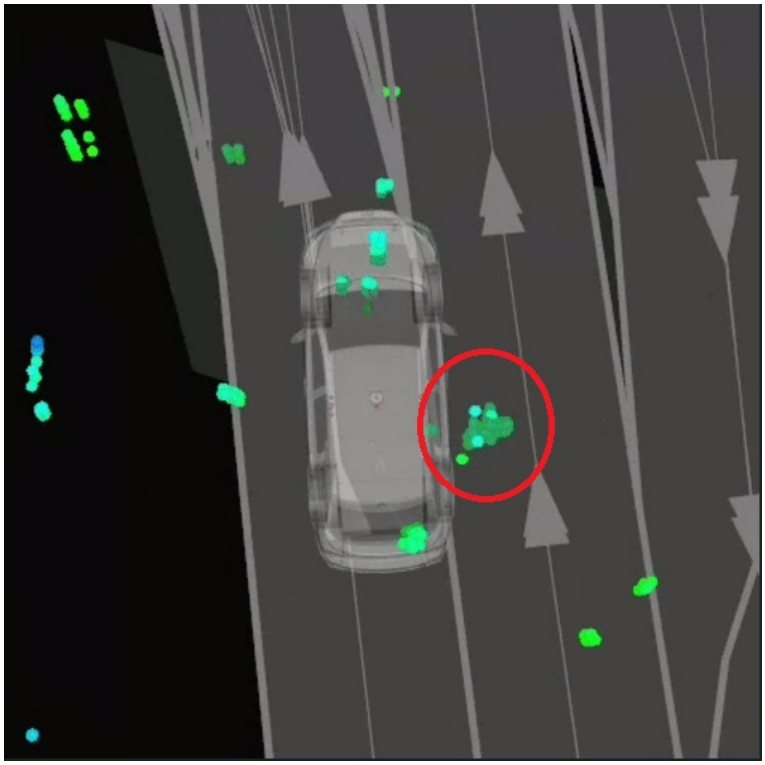


Figure 3.38: Autoware point-cloud plot.

3.7 Conclusions

This chapter presented an overview on the working principle of a radar system, focusing on the FMCW radar technology, and also the implementation and validation of a novel approach of a 360° 4D imaging radar. The developed MATLAB scripts and GUI play an important role in the operation and real-time configuration of the 360° radar prototype. This comprehensive GUI not only simplifies radar management but also provides the tools for data visualization and real-time control. The practical implementation and testing of the radar 360° prototype has demonstrated its capability to detect and map objects in both stationary and dynamic scenarios within a controlled environment. The initial stationary pole setup provided a solid validation of the system's ability to create accurate point-cloud representations, despite some minor discrepancies which are attributed to the coordinates precision of the measurement and also from radar resolution. The subsequent dynamic testing, involving both stationary and moving objects, further showcased the radar's effectiveness in tracking movement and maintaining object detection when the stationary target objects were obstructed by the moving one, despite some small detection errors and decrease in point-cloud points. Although the results are promising, the limitations observed, such as detection inaccuracy and errors created by the dynamic environments, highlight the need for further improvements. Nonetheless, the radar 360° prototype has proven to be a functional system with potential applications in real-world scenarios.

Chapter 4

mmWave CATR Anechoic Chamber Design and Applications

To properly test and calibrate radar sensors, before using them in real world applications and scenarios, it is necessary a controlled environment, one where there are no external RF interferences, which are considered noise to the sensors, and also where no RF echo signals are present. Such environment is known as an anechoic chamber. Since the state-of-the-art radar systems now work at such high frequencies, in the mmWave region of the spectrum, the antennas have smaller dimensions and the far-field region is typically only a few centimeters way. This means that for the mmWave region of the spectrum it is possible to work on smaller, more compact, anechoic chambers. To this end a mmWave CATR anechoic chamber was built.

This chapter will address the development process of such chamber for radar tests and measurements. The first section, 4.1, addresses the design considerations that were taken into account. The second section, 4.2, presents the 3 Dimensions (3D) modeling of the anechoic chamber. The third section, 4.3, addresses the building process and its several stages. The fourth section, 4.4, provides an insight on how to control the linear rails. The fifth section, 4.5, presents the EM characterization of the chamber, with the measurement setups. The sixth section, 4.6, addresses the radar measurements inside the chamber, a radar calibration, a polymer characterization and a SAR imaging reconstruction. Finally, in the seventh section, 4.7, the main conclusions are presented, followed by a brief discussion of results.

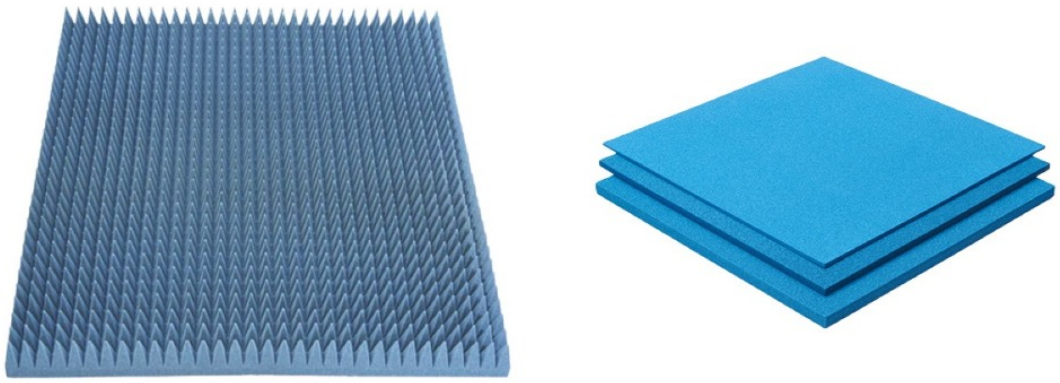
4.1 Design Considerations

4.1.1 Selection of the Absorber Material

The key components to an anechoic chamber are the RF absorbers. They are designed and shaped in such a way that the incident RF radiation is absorbed, effectively preventing the RF radiation to enter the chamber and also preventing it to exit the chamber. There are several types of RF absorbers, however, only two types will be addressed, the pyramidal and the flat absorber. The urethane pyramidal absorber, the one used to cover the majority of the chamber, was chosen mainly because it offers great performance when the incident waves come from different angles [62]. The flat panel absorber was only used to cover the corners of the chamber, given the fact that the pyramidal absorber can´t be used to cover 90° corners due to it's geometry.

	TYPICAL REFLECTIVITY (dB)											
	100 MHz	160 MHz	200 MHz	300 MHz	450 MHz	800 MHz	1 GHz	3 GHz	6 GHz	12-18 GHz	18-40 GHz	40-110 GHz[2]
WAVASORB® VHP-2								-20 dB	-25 dB	-40 dB	-45 dB	-55 dB
WAVASORB® VHP-4							-18 dB	-32 dB	-45 dB	-50 dB	-55 dB	-55 dB
WAVASORB® VHP-8						-20 dB	-30 dB	-40 dB	-50 dB	-50 dB	-55 dB	-55 dB
WAVASORB® VHP-12					-20 dB	-30 dB	-35 dB	-45 dB	-50 dB	-50 dB	-55 dB	-55 dB
WAVASORB® VHP-18				-20 dB	-30 dB	-35 dB	-40 dB	-50 dB	-50 dB	-50 dB	-55 dB	-55 dB
WAVASORB® VHP-26			-20 dB	-25 dB	-32 dB	-40 dB	-45 dB	-50 dB	-50 dB	-50 dB	-55 dB	-55 dB
WAVASORB® VHP-36		-20 dB	-25 dB	-30 dB	-40 dB	-45 dB	-50 dB	-50 dB	-50 dB	-50 dB	-55 dB	-55 dB
WAVASORB® VHP-45	-20 dB	-22 dB	-25 dB	-35 dB	-40 dB	-45 dB	-50 dB	-50 dB	-50 dB	-50 dB	-55 dB	-55 dB

Figure 4.1: WAVASORB VHP absorbers typical reflectivity.



(a) VHP-2 pyramidal absorber. (b) AN-75 flat absorber.

Figure 4.2: WAVASORB absorbers.

After a research among microwave absorbing materials manufacturers it was decided to use the WAVASORB VHP-2 from Emerson & Cumming Inc, which is a high performance urethane pyramidal absorber. According the manufacturer technical datasheet [63] these absorbers are composed of urethane foam covered in carbon and offer a reflectivity of -45dB for RF signals from 18 - 40 GHz and -55dB for RF signals from 40 - 110 GHz, as it can be seen in Fig. 4.1, which comprehends the entire frequency bands typically used in automotive applications (i.e. 24 GHz, and 76 – 81 GHz).

The chosen flat panel absorber is the WAVASORB AN-75 also from Emerson & Cumming Inc. According the manufacturer technical datasheet [64] these are a series of lightweight, flat, flexible, carbon loaded urethane foam absorbers, consisting of a multilayer structure with different graded layers. These absorbers typically offer a reflectivity of -15dB, which is not as good as the reflectivity of the presented pyramidal absorbers, however they will exclusively be used to cover the chamber's corners, as previously explained.

Both of these absorbers are available in tiles with 61 cm x 61 cm. The pyramidal absorber has a height of approximately 5.6 cm, as specified in its technical datasheet [63], and can be seen in Fig. 4.2a, and the flat absorber has a height of 2.9 cm, as specified in its technical datasheet [64], and can be seen in Fig. 4.2b.

4.1.2 Anechoic Chamber Dimensions

When designing a rectangular anechoic chamber one must account for the following factors: far-field distance, which sets the phase uniformity across the test aperture, and the minimum and maximum operating frequencies of the antennas [65].

According to [65] the minimum length of an anechoic chamber is determined by the far-field condition, given by equation 4.1 where the parameter R is the minimum length of the anechoic chamber, D is the aperture size of the antenna under test and λ is the wavelength of the highest operating frequency.

$$R \geq \frac{2D^2}{\lambda} \tag{4.1}$$

Subsequently, according to [65, 66], the width of the anechoic chamber must meet the criteria given by equation 4.2, where the parameter W is the width of the anechoic chamber, in order to have incidence angles below 60° which influences the amount of attenuation experienced by the RF radiation. According to [67], the height of the anechoic chamber should be the same as the width.

$$W \geq \frac{R}{2} \tag{4.2}$$

Since the main goal is to use the chamber for the frequency bands typically used in automotive applications (i.e. 24 GHz, and 76 – 81 GHz), the far-field condition was calculated for 24 GHz as well as for 81 GHz.

At 24 GHz the antenna with the biggest aperture in our laboratory has an aperture of 10 cm. So by applying equation 4.1 and substituting D with 10 cm, and λ with 1.25 cm (wavelength at 24 GHz) we get a far-field length of 1.6 m. The antenna of the AWR1843BOOST evaluation board has an aperture of 12 mm. So by applying equation 4.1 and substituting D with 12 mm, and λ with 3.7 mm (wavelength at 81 GHz) we get a far-field length of 7.8 cm.

So, in order to meet both conditions the anechoic chamber needs to have a length bigger than 1.6 m. Considering that the selected absorber tiles have 61 cm in length/width it was decided to design the chamber with 1.83 m in length, using 3 entire absorber tiles to make the full length. Since the width needs to be greater or equal to half the length of the chamber, as previously shown, it was decided that the width would be half of the length of the chamber, 91.5 cm. This decision accounts not only for the width requirements, 4.2, but also ensures that the chamber's dimensions are always multiples of the absorber tile dimensions, simplifying the cutting process and avoiding unnecessary cuts that could compromise the integrity of the absorbers. As previously discussed, the height should be the same as the width, so the height will also be 91.5 cm. With all of these measures figured out, the anechoic chamber will have an effective volume, or test region, of 1.83 m x 91.5 cm x 91.5 cm.

The last dimensions to figure out are related to the bottom of the chamber. In order to provide motion to the devices under test or sample materials it was decided to use a linear rail actuator system at the bottom of the chamber. In this case the bottom of the anechoic chamber would be modular and therefore easily removable. This provides a versatile system that can be used for both static measurements and measurements with materials in motion. The linear rail actuators are going to provide motion in 2 axis, in a T shape. One linear rail actuator, with 1.35 m in length, will be placed at the center of the chamber parallel to the chamber's length, while the other, with 75 cm in length, will be placed close to one of the chamber's end parallel to the chamber's width. These linear rail actuators have 6 cm of height so in order for them to fit in the bottom of the chamber, the bottom was designed

as a removable piece with a 7 cm spacing underneath, where the linear rail actuators will be placed. Such a linear rail actuator can be seen assembled in section 4.3.

4.2 3D Modeling

With the measures worked out it was time to proceed to the 3D modeling of the chamber. It was decided that the enclosure of the chamber would be made out of plywood. Plywood is a primary choice building material for many builders because it presents several benefits over other materials, such as strength, durability and lightweight, which came mainly because of the way plywood is built. Plywood is made of thin sheets of wood that have been pressure-bonded with adhesives at varying angles, which gives plywood a cross-grain pattern. This pattern ensures a consistent strength across the entire length of the board, gives it durability and also makes it resistant to warping, cracking and twisting. In addition to its strength, durability and lightweight, plywood is also less expensive than similar boards made of solid wood.

The first step was to design the enclosure using 10 mm thick plywood, except for the base, which uses 20 mm thick plywood. This happens because the strength of a wooden enclosure is rated based on the weight it can carry before the cap (top ans sides) is added. In order to maintain the effective volume of 1.83 m x 91.5 cm x 91.5 cm the enclosure needed to be a little bigger to take into account the absorber height, 5.1 cm. So by adding the height of the absorber, 5.1 cm, plus the thickness of the plywood, 10 mm, on each side we end up with the real length and width of the enclosure, 195.2 cm and 103.7 cm respectively. The height of the enclosure is a little bigger given the fact that the linear rail actuators are on the bottom of the chamber which adds roughly 7.5 cm of height to the overall height. So by adding the height of the absorber on each side, 5.1 cm, plus the thickness of the plywood, 10 mm on the top and 20 mm on the bottom, and the 7.5 cm from the removable bottom we end up with having a height of 112.2 cm. In Fig. 4.3 it is shown the 3D model of the wooden enclosure for the chamber.

The enclosure was then splitted close to the top in order to provide a removable opening top that might be used as an extension for the test region or to use a certain equipment outside of the chamber. This opening top will be closed for most of the time and for most of the measurement setups. In Fig. 4.4 it is shown the 3D model of the splitted wooden enclosure for the anechoic chamber as 2 parts, the removable top and the bottom, identified as 4.4a and 4.4b respectively.

Afterwards the front doors were drew over the enclosure and also splitted. Both doors are 80 cm x 80 cm in order to provide a good opening to easily setup the measurement equipment inside. They are located at the center of the front side of the enclosure, both in height and length.

Lastly, as a final touch, for both robustness and embellishment, aluminium angle profiles were added along the edges of the enclosure. A trolley table rack was also added to the 3D model, and it will serve as a stand for the measurement equipment as well as for a smooth and easy transportation. It also adds height to the chamber, roughly 80 cm, which makes it easier to setup the equipment inside while standing. The final 3D model for the chamber can be seen in Fig. 4.5, where the heights are highlighted, and also in Fig. 4.6, which represents an artwork model of the chamber.

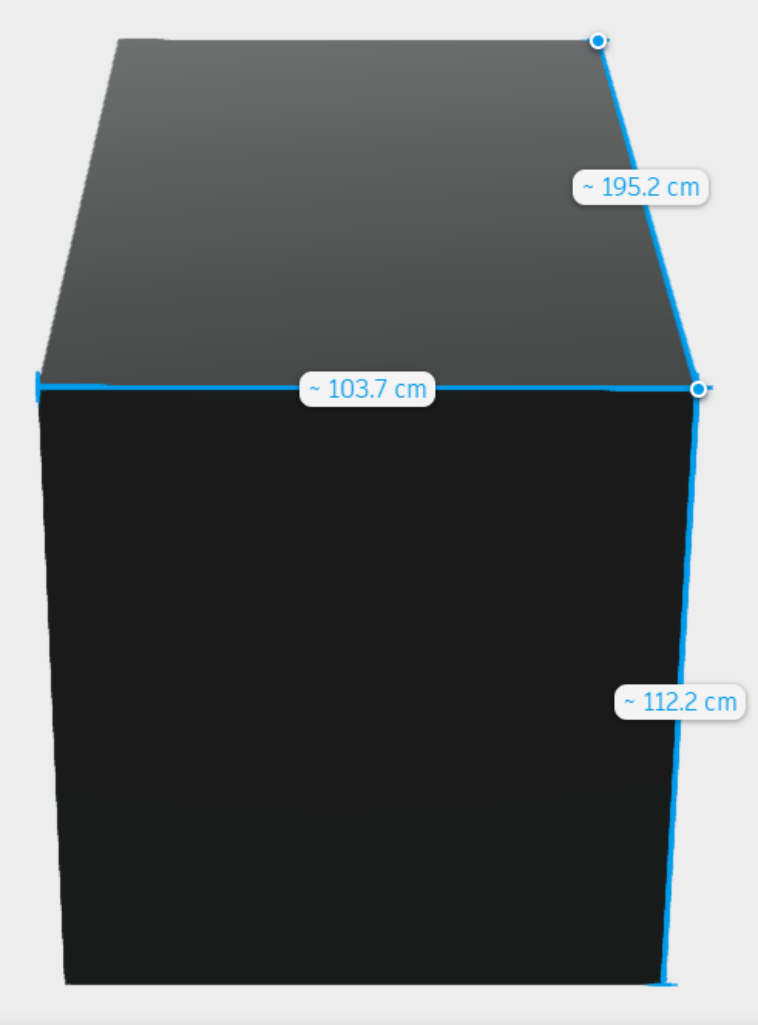
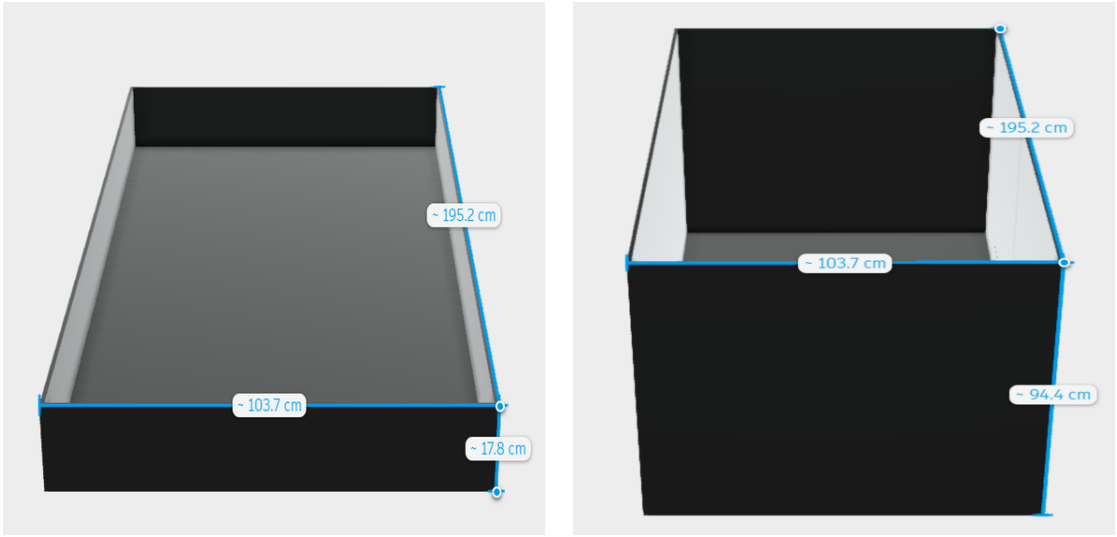


Figure 4.3: 3D model of the wooden enclosure for the anechoic chamber.



(a) Removable top. (b) Bottom.

Figure 4.4: 3D model of the splitted wooden enclosure for the anechoic chamber.



Figure 4.5: F3D model of the anechoic chamber.

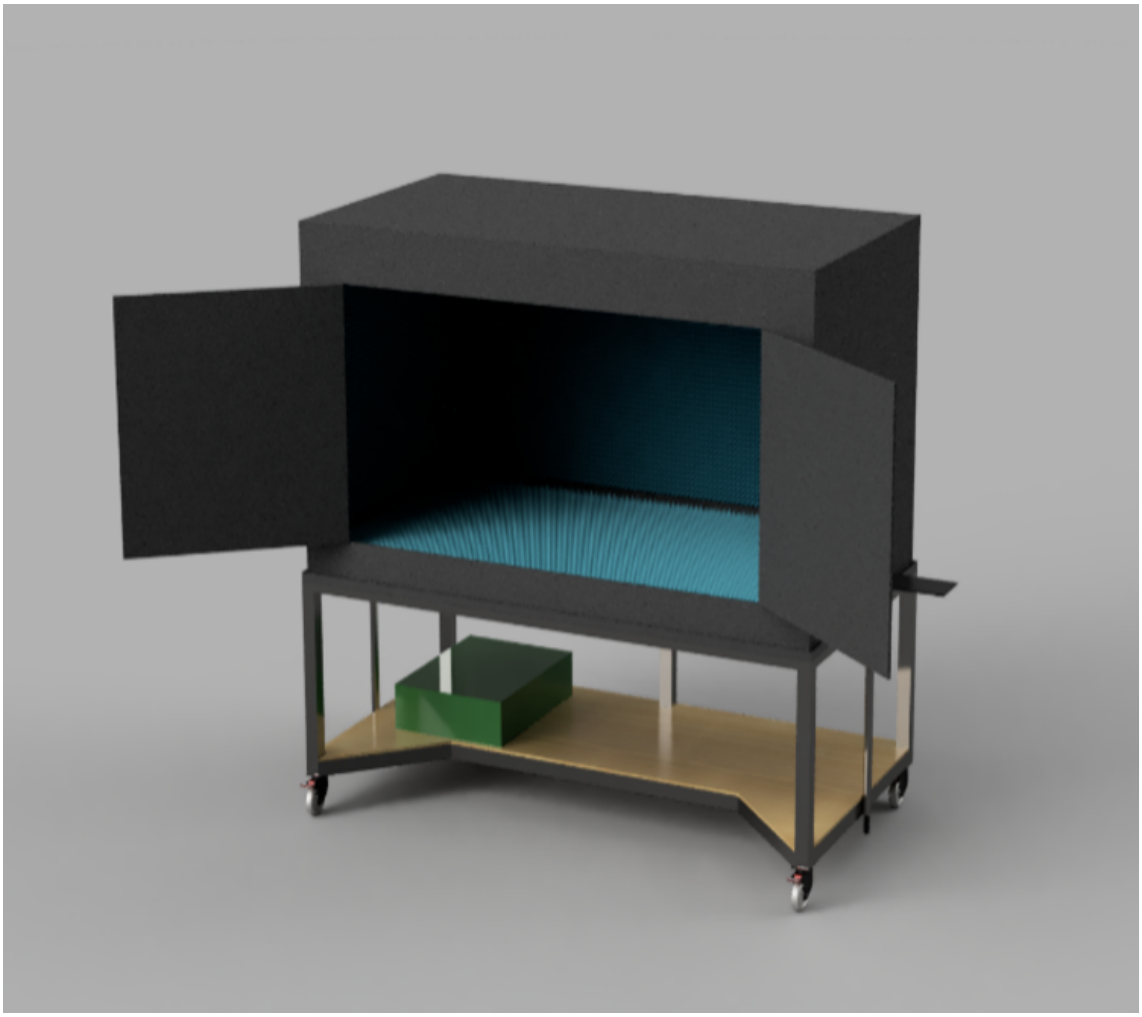


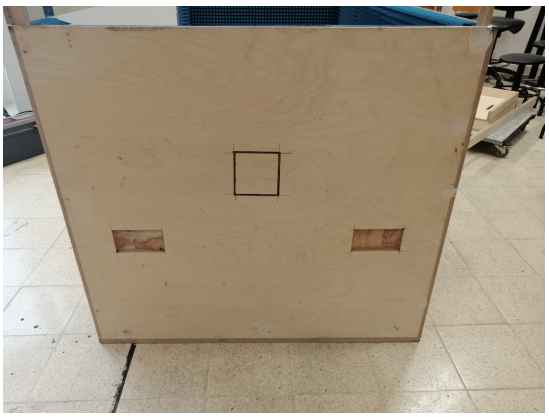
Figure 4.6: Artwork 3D model of the anechoic chamber.



Figure 4.7: Covering the enclosure with aluminium foil.



(a) Holes for the cable grommets (in blue).



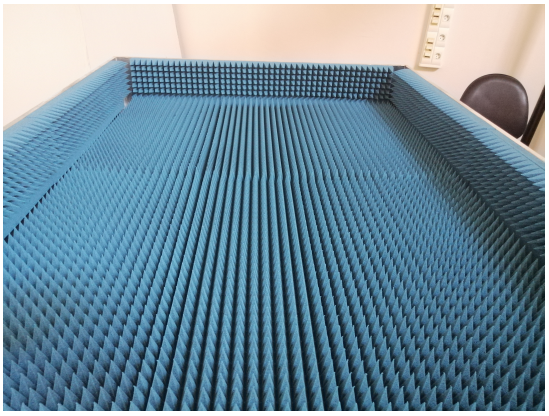
(b) Holes for the handles and frequency extenders.

Figure 4.8: Cuts and holes done on the enclosure.

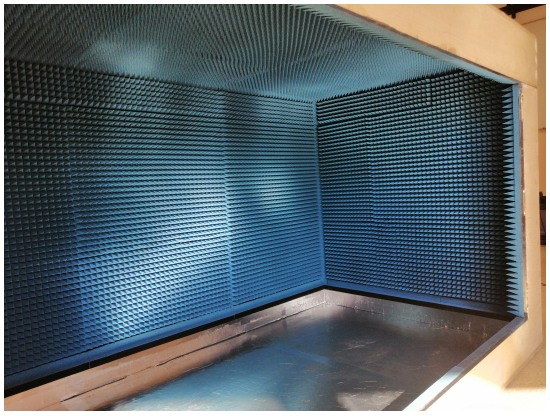
4.3 Prototype Building Process

The plywood enclosure for the anechoic chamber was then built by a local carpenter according to our 3D model and all of the remaining work was done in our facilities. The first step was to cover the inside of the enclosure with aluminium foil sheets, in order to create EM shielding. This shielding causes the RF signals present on the outside of the chamber to be reflected, thus preventing them to influence the RF signals inside of the chamber [65]. 0.1 mm sheet aluminium was used to cover the interior of the enclosure, as it can be seen in Fig. 4.7.

The next step was to cut the holes for both front doors as well as for the handles, cable grommets and also for the Vector Network Analyzer (VNA) frequency extenders, all shown in Fig. 4.8. Afterwards we proceeded to cover the entire enclosure with the RF foam absorbers, as it can be seen in Fig. 4.9.



(a) Removable top.

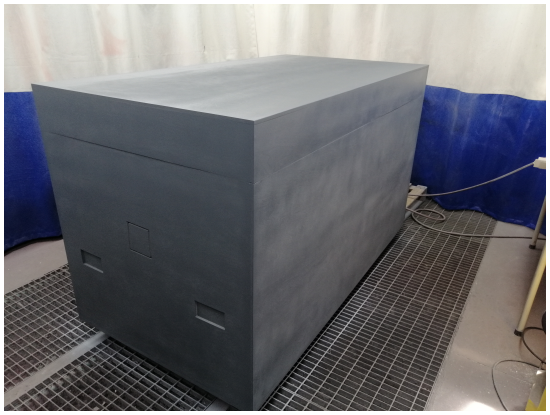


(b) Chamber interior.

Figure 4.9: Covering the enclosure with RF foam absorbers.



(a) Primer.



(b) Epoxy paint.

Figure 4.10: Anechoic chamber during the painting process.

After all the RF absorbers were glued it was time to paint the chamber. The chamber was then taken to a automotive spray painting booth with downdraft airflow ventilation, in order to be properly painted using a air compressor paint sprayer. However there was a need to repair the cracks and dents in the plywood, because paint will not fill in cracks or other imperfections, and as a result we would end with a poor finishing. We repaired the plywood using wood filler which was then sanded, in order to provide a smooth surface for the paint. Afterwards a coat of primer was applied on the chamber. The primer is effective in sealing the plywood surface and prevents the paint from soaking in it and also helps the paint to achieve a uniform, rich look on top of wood. The painting process then continued by adding two coats of dark grey satin paint, which provides a higher durability to the plywood, as well as a neat finishing look. In Fig. 4.10 the chamber is shown during the painting process.

Following the painting process we started adding aluminium angle profiles along the edges of the anechoic chamber. This improves the overall aesthetics of the anechoic chamber and also makes it more robust in case it hits a wall or other objects during transportation. The transportation and door handles were also placed. In Fig. 4.11 the chamber is shown with the aluminium profiles and handles in place.

The linear rail actuators were then installed on the chamber floor using screws, the removable



(a) Front. (b) Sideways.

Figure 4.11: Anechoic chamber with the aluminium profiles in place.



(a) (b)

Figure 4.12: Linear rail actuators in place with the removable bottom.

bottom was then placed on top. In Fig. 4.12 it is possible to see the linear rail actuators with the removable bottom on top. End switches were then added to each rail in order to properly calibrate the movable platform.

The chamber was then finally placed on top of the trolley table rack and with it the construction/assembly process was complete. The trolley table rack provides an easy transportation for the chamber and, at the same time, serves as a stand for the measurement equipment. The anechoic chamber with the trolley is shown in Fig. 4.13.

The last and final step was to design and assemble a electronic system to control the stepper motors. The main controller behind the system will be an Arduino Nano, which is a board based on the ATMEGA328p. The ATMEGA328p is a high-performance 8-bit AVR Reduced Instruction Set Computer (RISC)-based micro-controller with an operation voltage between 1.8V and 5.5V and offers many features, however only the ones used in this system will be highlighted here, such as: 23 general purpose I/O lines, 8 channel 10 bit ADC, three flexible timer/counters with compare modes, internal and external interrupts and a serial programmable Universal Synchronous and Asynchronous Receiver-Transmitter (USART), as specified in its technical datasheet [68]. The DM556T digital driver was used as the high power controller for each stepper motor. This driver is able to power 2-phase and 4



Figure 4.13: Assembled anechoic chamber on the trolley rack

phase stepper motors smoothly with optimal torque and low motor heating and noise. Its operating voltage is 20-50V Direct Current (DC) and it can output up to 5.6A of current. It has 3 digital (0-5V) input signals for the motion control, the clock signal, which sets the speed of the stepper motor, the direction signal, which sets the rotation direction of the stepper motor ('1' for anti-clockwise motion and '0' for clockwise motion) and the enable signal, which enables the power output of the driver ('1' disables the power output and '0' enables it), while all of the micro step and output current are done via Dual In-line Package (DIP) switches, as specified in its technical datasheet [69]. As previously mentioned in 4.1 the used stepper motor was the Nema 23. This is a 2 phase bipolar stepper motor with 1.8° of step angle, 1.85Nm of holding torque and 2.8A of rated current/phase, as specified in its technical datasheet [70]. Lastly a switching mode power supply was used to power the system. The power supply is the Meanwell LRS-350-24, which has an output voltage of 24V DC and is capable of outputting current up to 14.6A, as specified in its technical datasheet [71].

The schematics diagram of the control system is presented in Fig. 4.14. The 3 control digital signals, required to run the DM556T drivers, are connected directly to the arduino in its general purpose I/O lines. The end switches are connected to the ADC channels in order to check which end switch was activated. Ideally this process should be done using external interrupts connected to each end switch, however the Arduino Nano only has 2 external interrupts. External interrupts are triggered by external signals applied to specific pins of the micro-controller, in the Arduino Nano those pins are D2 and D3. Those pins directly fire interrupt signals to the micro-controller when a certain external event occurs. When the micro-controller receives an interrupt signal, it pauses the main program execution and saves its current state, then jumps to the address where the corresponding interrupt function is located and executes that function in its entirety. Afterwards the micro-controller restores the state of the main program and resumes its execution. But since there are only 2 external interrupts, it was not possible to connect 6 end switches to the external interrupts "the right way". In order to bypass this situation a dual-quad or logic gate was used, the 4072BE. This way, and as shown in the schematics diagram in Fig. 4.14, all of the end switches are connected to the or logic gate which produces only one output that is then connected to one external interrupt. So, when one of the end switches is activated the external interrupt is activated as well, which means that the interrupt function is then executed. In this function the micro-controller checks which end switch was activated by reading the voltage on each one, since they are all connected to its ADC channels. This way we effectively check which end switch was activated and are then able to deactivate the corresponding driver to that axis and calibrate the movable platform position.

With everything considered a PCB was designed to integrate all of the components, and it can be seen in Fig. 4.15. The connections to the DM556T drivers as well as to the end switches are done via the orange t-block connectors present in the PCB.

Finally, all of the components were placed inside a Polyvinyl Chloride (PVC) enclosure to ensure that internal electrical and electronic components are protected in any environment. Holes were drilled on the enclosure for all of the connectors and for air ventilation. The components were then placed on the bottom and screwed to it, and the wiring was then performed. In Fig. 4.16 the control system PVC enclosure is shown with all of the components mounted on it.

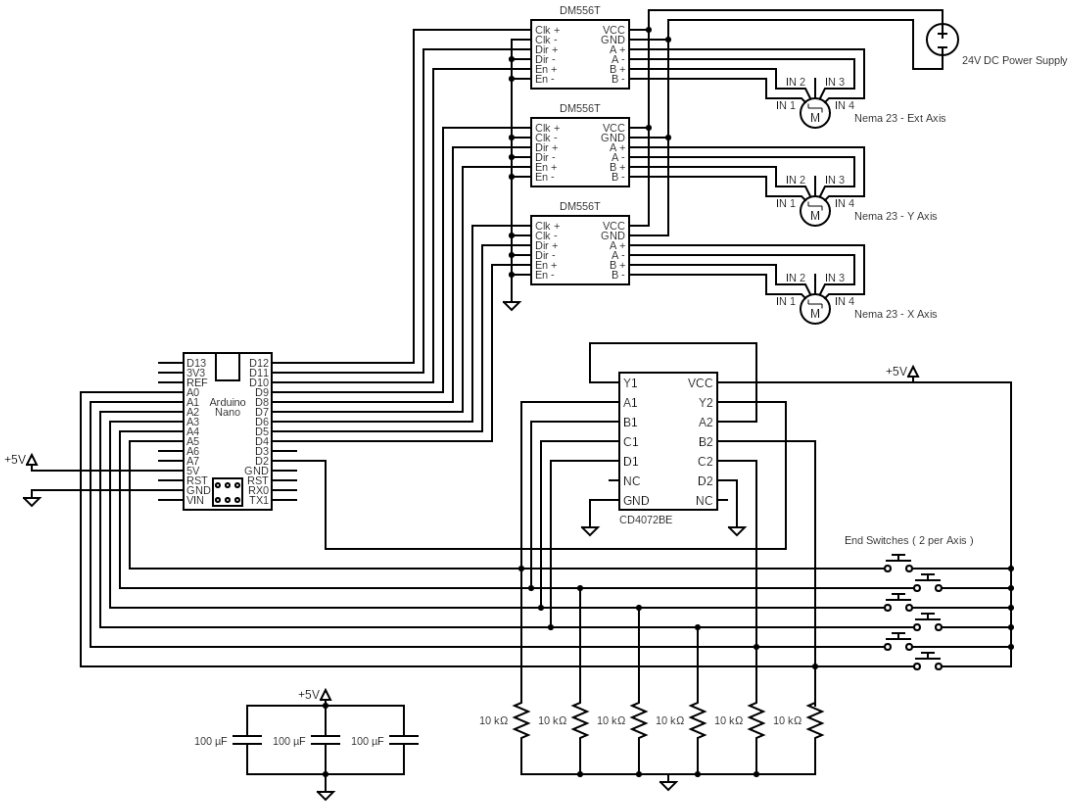


Figure 4.14: Control system schematics diagram.

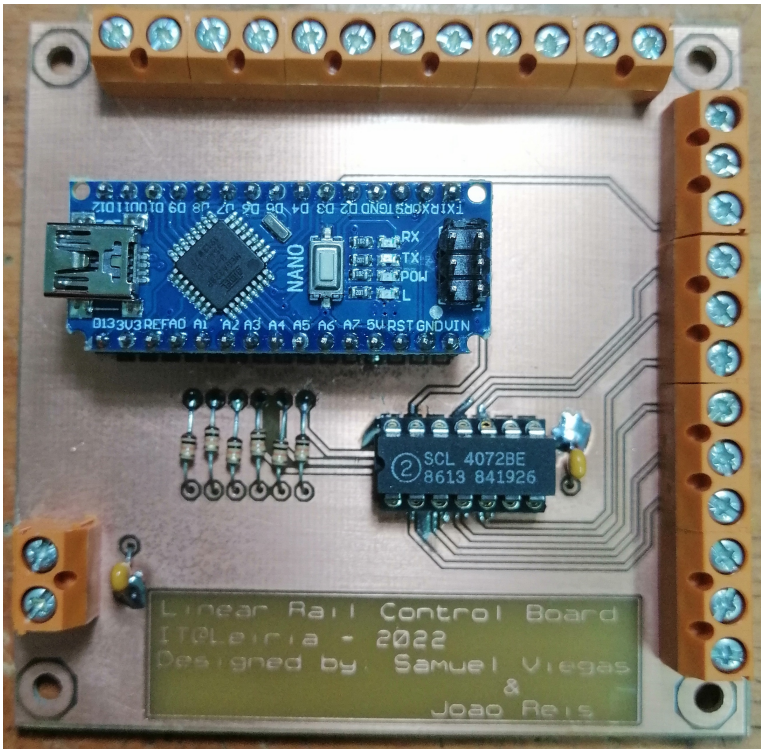
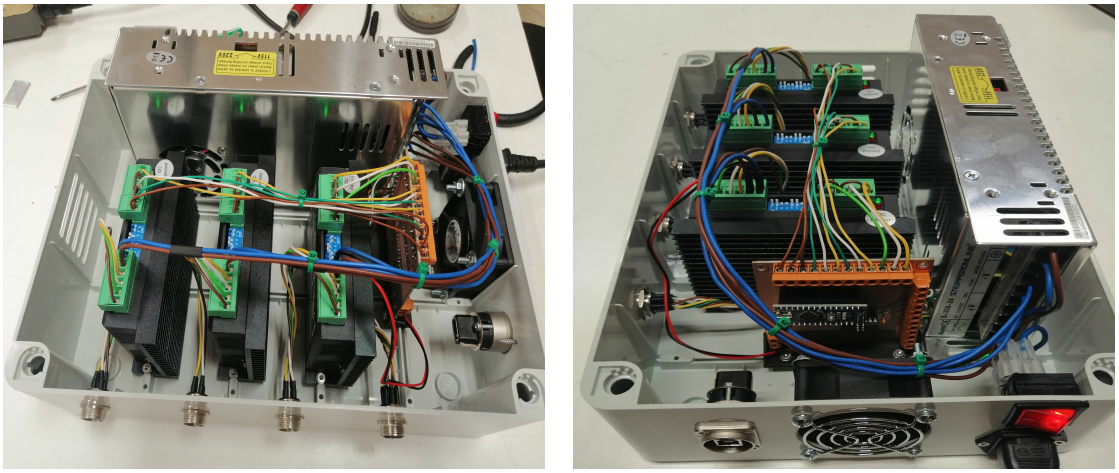


Figure 4.15: Control system PCB.



(a) (b)

Figure 4.16: Linear rail actuators control system.

The entire construction process was recorded and a time-lapse video was made. It can be seen using the following YouTube URL [1].

4.4 Linear Rail Motion Control

The linear rails stand at the bottom of the anechoic chamber, according to the diagram presented in Fig. 4.17, and as shown during the building process in the previous section 4.3. As it is possible to visualize in the figure, the linear rail corresponding to the x axis has a maximum travel distance of 1180 mm while the linear rails corresponding to the y and external axes both have a maximum travel distance of 635 mm. However the maximum allowed travel distance on the y axis gets 60 mm smaller (575 mm) when the external axis is placed on top of the y axis, a setup that is usually used for SAR measurements. The stepper motor of the external axis, which is highlighted in red in Fig. 4.18, eventually takes 60 mm from the available travel distance on the rail of the y axis.

The motion of the linear rail axis, managed by the control system, is requested via serial commands, taking advantage of the USART protocol available in the micro-controller. When the control system is powered it will send the following information (with a baud-rate of 115200):

- COMPACT ANECHOIC CHAMBER - Linear Rail Control System
- Send 'start' to initialize

It will then wait until the 'start' command is sent. When the 'start' command is received the control system immediately sends the following information:

- Bypass home function? [Y/n]
- Warning: Only bypass home function when the linear rails are calibrated and the positions are known!

[1] `https://youtu.be/ZtirszrjntU`

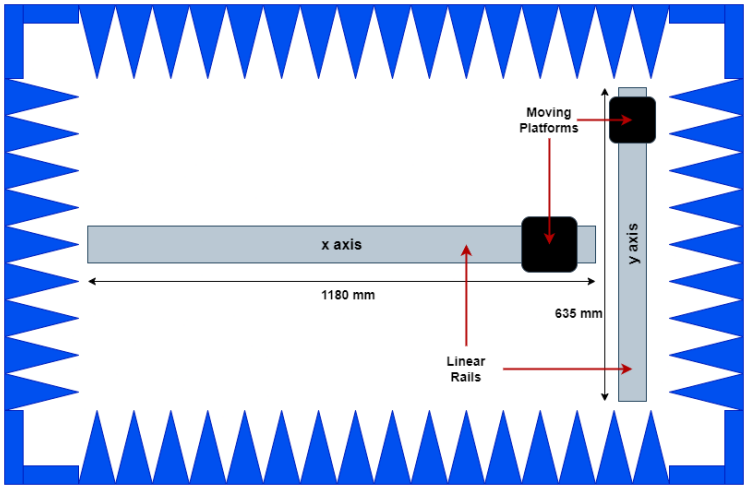


Figure 4.17: Diagram of the linear rails placed at the bottom of the anechoic chamber.

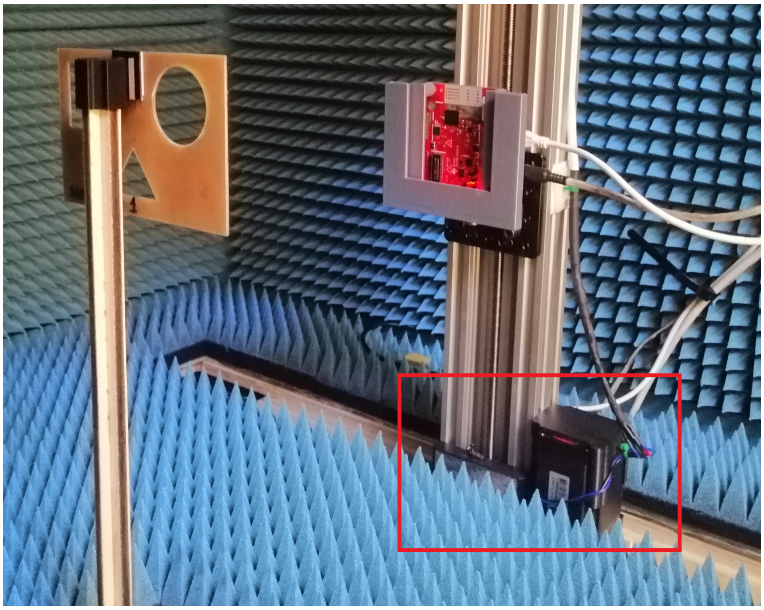


Figure 4.18: SAR measurement setup with the external axis mounted on top of the y axis.

Depending on the received command, 'Y' for yes and 'n' for no, the control system will either perform the linear rail calibration to a home position or discard it. When 'n' is received the control system discards the calibration of the linear rails and essentially accepts any command regarding the movement of the rails. This approach must only be used when the user knows the exact position of the linear rails and needs to perform very specific movements. When 'Y' is received the control system will calibrate the linear rails to a home position. Before the home function is done the control system sends the following information:

- Home each axis separately? [Y/n]
- Useful when only one axis is needed! If 'n' is sent then home is performed in all axis!

This serves to evaluate what the user wants to do, and is useful when only one axis is needed for a measurement. If the user chooses 'n' the system will proceed to do a complete home function where all of the axes are calibrated to the home position. If the user chooses 'Y' then the program will send the following information:

- Select which axis to home by sending the following options:
- homeX - Home X axis in the default home position
- homeInvertX - Home X axis in the opposite side of the default home position
- homeY - Home Y axis in the default home position
- homeExt - Home external axis in the default home position
- Once the home function is performed on the axis it is possible to home another axis
- Simply send 'done' in order to continue once the axis is at home position

This gives the user the option to select which axis is needed for a specific measurement and only home the one that is needed. It is also possible to home more than one axis. The user can select the home calibration on one axis and then select the option to calibrate the next axis. When the user already has the needed axis calibrated he just needs to send the command 'done' and the system is ready to use.

When the home function is selected for all axis the system sends a couple additional information to check if the external axis is connected to the system or not. It evaluates if the the external axis is connected to the system and if it is the only one connected to the system. This avoids unnecessary calibration of axes in case they are not connected. The sent information are the following:

- Is the external axis connected? [Y/n]
- Warning: If the answer is no, the external axis will not be calibrated and will be deactivated!
- Is the external axis the only one connected? [Y/n]
- Warning: If the answer is yes, the X & Y axes won't be calibrated and will be deactivated!

After the home calibration is completed the system will ask the user if he wants to receive the current positions of the rails as they move, which is send every 500 ms. For that it sends the following information:

- Display rail positions while in motion? [Y/n]

- If yes, the rail positions will be sent via USART every 500ms!

The message that displays the current positions of the rails looks like this:

- X current position: 0.0mm Y current position: 0.0mm Ext current position: 0.0mm

Finally, when the linear rails are calibrated the system is setup and ready to use. It informs the user of such with the following information:

- Setup and calibration completed! Anechoic chamber linear rails are ready to use!

In order to control the system the user then simply has to send a command that contains the distance that the user wants for each axis to move. The command basically contains the axis that we want to move followed by the distance that we want it to move in mm, accepting float type. The following command shows how it can be done, to move only one axis or to move all of them:

- ySet70.5
- xSet80.0,ySet120.5,extSet0.0

When the commands are received by the system it acknowledges it by sending the following information:

- X axis set: 80.0mm Y axis set: 120.5mm Ext axis set: 0.0mm

When the values in the sent command exceed the maximum distance that the linear rail can travel on, the system sends the following information:

- Warning: The set x position exceeds the maximum distance on the x axis rail! Sending it to the maximum allowed distance (1180mm)
- Warning: The set y position exceeds the maximum distance on the y axis rail! Sending it to the maximum allowed distance (575mm)
- Warning: The set y position exceeds the maximum distance on the y axis rail! Sending it to the maximum allowed distance (635mm)
- Warning: The set ext position exceeds the maximum distance on the ext axis rail! Sending it to the maximum allowed distance (635mm)

Finally, when all the linear rails reach the final set position, the system sends the following information:

- Linear rails reached the set position!

Furthermore, the user can send the command 'help' to check what else the system can do. It sends the following information when the 'help' command was sent to it:

- Available commands:
- home - Sends the linear rails to the home position
- xSet[float],ySet[float],extSet[float] - Sends the new position to the linear rails in mm (ex: xSet100.5,ySet200,extSet20.8)
- getPosition - Gets the linear rails current position
- newHome,x[float],y[float],ext[float] - Sends the linear rails to the new position and sets that position as the new home (ex: newHome,x100,y200,ext50.8)

Besides setting the new positions for the rails, the user can also re-do the home function whenever it is needed using the 'home' command and can get the current position of each of the rails using the 'getPosition' command. When the current position is requested to the system it will send a message such as the following:

- Current position at X: 0.0mm Y: 0.0mm Ext: 0.0mm

A new home position can also be set by using the 'newHome' command followed by the new positions on each rail. When finished the system will send the following information:

- New home position at X: 0.0mm Y: 0.0mm Ext: 0.0mm

A flow chart of procedure previously explained, from the linear rail axis control system, can be seen in Fig. 4.19.

4.5 Chamber Characterization

The characterization of an anechoic chamber is of the utmost importance. Anechoic chambers are used with the intention to simulate the free space environment, and if there are reflections within the chamber they will introduce errors in the measurement results. To avoid these errors it is necessary to quantify the impact of said reflections if they do indeed exist. An industry standard to characterize anechoic chambers is the Free-Space Voltage Standing Wave Ratio (VSWR) method [65, 72], and that's the method that was performed on the anechoic chamber in order to characterize it.

Free Space VSWR method uses a probe antenna to measure the magnitude of a reflected signal from the chamber walls. The measurement setup consists of 2 antennas, one static and another that moves continuously along one axis (a parallel or perpendicular linear path to the chamber surface), typically the static antenna is referred as the TX while the moving antenna is the probe or the RX. While the probe antenna moves the received signal is measured using a VNA. The signal is a superposition of the direct signal from the TX antenna and the reflections from the side, back walls and other aspects of the anechoic chamber. The interference between the direct signal and the reflection signals are superimposed constructively and destructively so that the measured signal inside the quiet zone can be seen as variation along the scanning axis similar to a standing wave [72]. Each scan provides amplitude vs. linear position data which are sufficient to characterize the level of the signals reflected from the chamber surfaces at various angles. However, it is generally impractical to evaluate the entire area of each chamber surface [73].

The anechoic chamber was characterized in 2 different bands, 1 to 20 GHz and 60 - 90 GHz. The main goal was to characterize it, especially, in the 2 automotive bands, 24 GHz and 76 - 81 GHz. The 76 - 81 GHz band lies within the 60 - 90 GHz, however measurements at 24 GHz were not possible since our VNA has a frequency range of 100 kHz - 20 GHz, and is only able to go up to 60 - 90 GHz band using frequency extenders. A measurement was performed at 20 GHz in order to have an understanding on how the chamber works at those frequencies, at 24 GHz a similar behaviour should be expected since it's only 4 GHz apart. The measurement setups will be explained in detail in the next subsections.

4.5.1 1 to 20 GHz

To characterize the anechoic chamber in the 1 - 20 GHz band the following equipment was used: C4420 VNA and QRH0140 antennas. The C4420 is a high-performance VNA

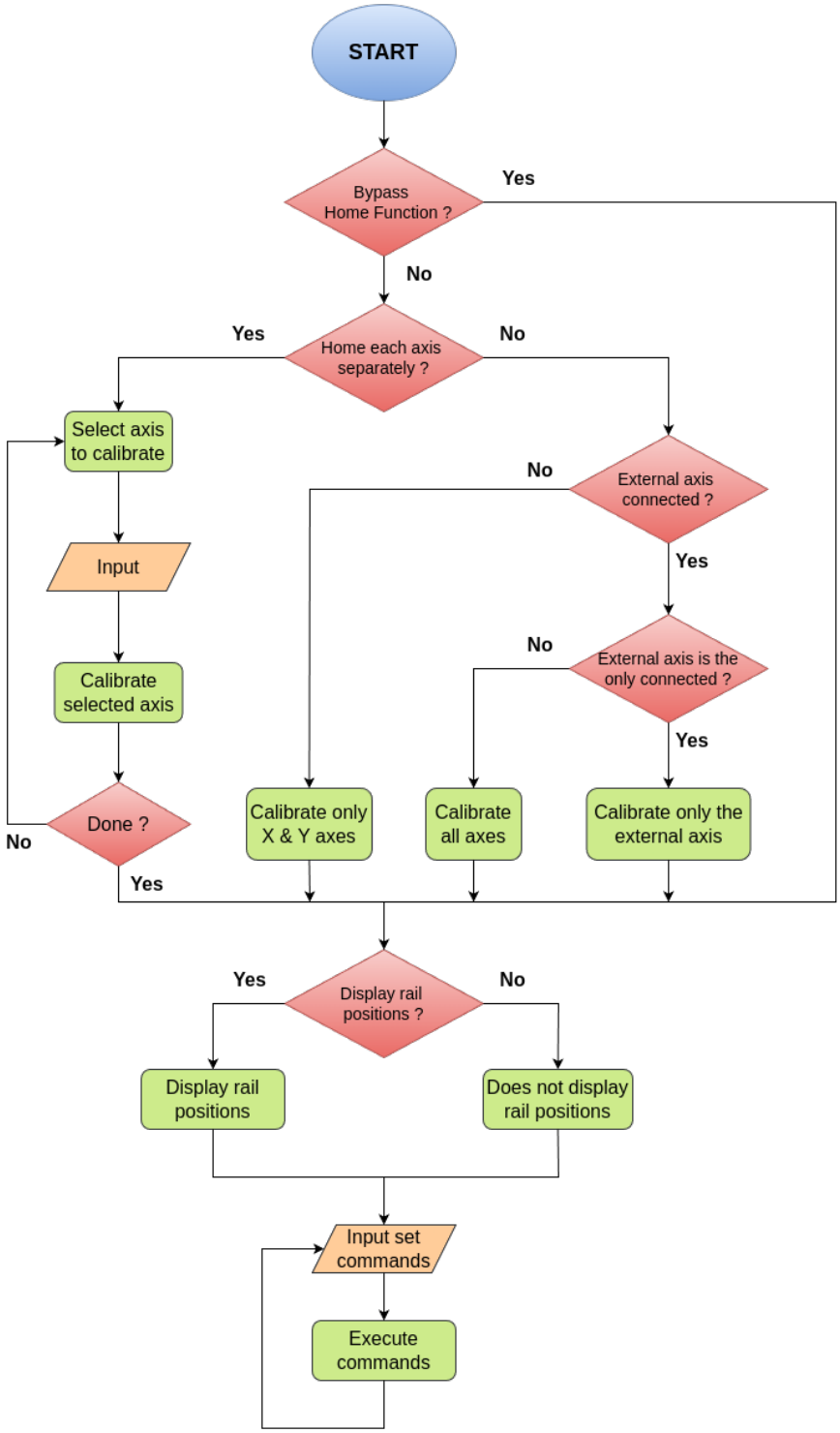
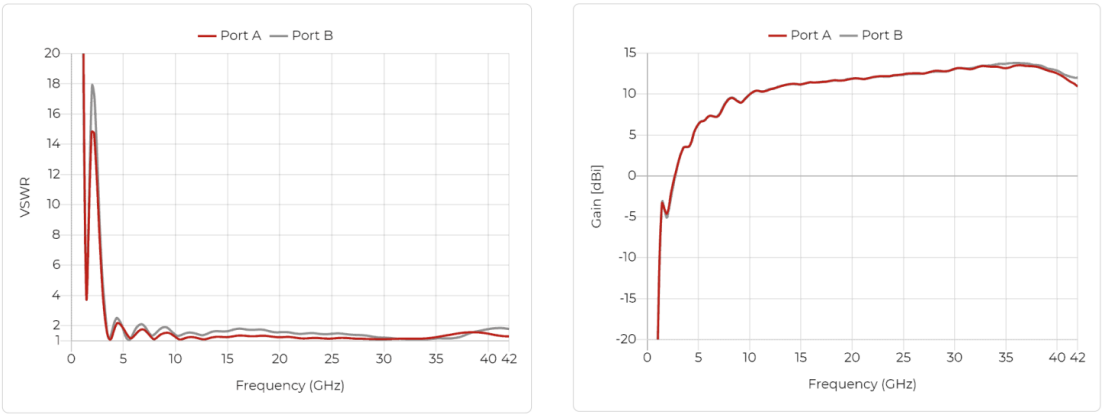


Figure 4.19: Flowchart of the implemented linear rail axis control system.



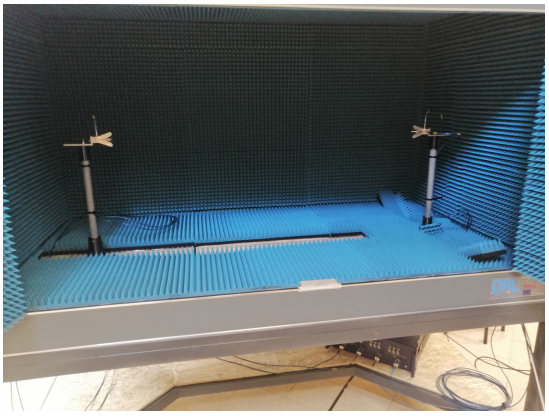
(a) VSWR. (b) Gain.

Figure 4.20: QRH0140 parameters.

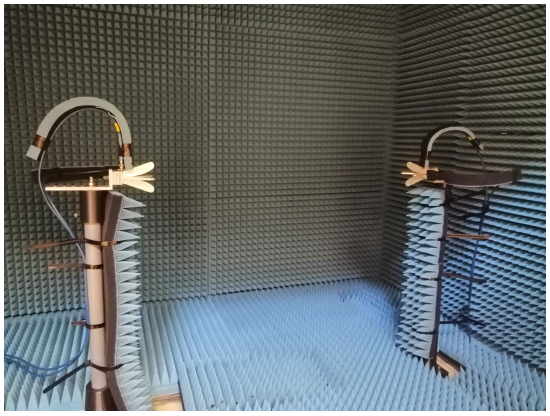
manufactured by Copper Mountain Technologies. It has a frequency range between 100 kHz and 20 GHz, a dynamic range of 135 dB and allows up to 500001 measurement points per frequency sweep, with a typical measurement time per point of 12 μs, as specified in its technical datasheet [74]. The QRH0140 is a quad double ridged horn broadband antenna manufactured by RFspin. It operates from 1 GHz up to 40 GHz with dual polarization, vertical and horizontal, its VSWR and gain (compared to an isotropic radiator) are shown in 4.20, as specified in its technical datasheet [75]. Despite the fact that the manufacturer states in the technical datasheet that the antenna operates from 1 GHz to 40 GHz, it is possible to observe from the VSWR curve, shown in 4.20a, that the VSWR values are way above 2 in frequencies below 4 GHz, which means that the return loss is less than 10 dB for those frequencies. A standard for antenna systems is a return loss of 10 dB or higher, meaning that 90% or more of the input power is effectively transmitted by the antenna. So, this preliminary analysis indicates that the antenna is not well matched for frequencies below 4 GHz, but this will be tested later during the actual measurements.

The setup for these measurements can be seen in in 4.21. The antenna on the right side of both figures is the static antenna, while the antenna on the left side is the moving antenna. The center of both antennas is at 45 cm of height, at the center of the chamber. They are also centered in the width of the chamber, at 45 cm from the lateral walls. At the starting point both antennas are 1.33 m apart, then the moving antenna will travel 1 m over the linear rail whilst the VNA doing measurements after every 1 mm of travelled distance. In Fig. 4.22 the diagram of the setup is shown, the line represents the distance between both antennas while the dotted line represents the distance that the moving antenna will travel. The moving antenna was then connected to the VNA on ports 1 and 2, for horizontal and vertical polarization, respectively. The static antenna was connected to the VNA on ports 3 and 4, once again for horizontal and vertical polarization, respectively. The VNA was configured to do frequency sweeps from 1 to 20 GHz with 5001 measurement points.

From the reflection coefficients (for both antennas on both polarizations), shown in Fig. 4.23, it is possible to conclude that the antennas are not well matched for frequencies below 5 GHz. This can also be observed from the non-linear phase response and from the magnitude response in transmission coefficients, shown in Fig. 4.24, and can be seen from both the horizontal polarization ($|S_{31}|$) and the vertical polarization ($|S_{42}|$). These results were somewhat expected given the preliminary analysis on the VSWR curves provided in the technical



(a) During assembly.



(b) Final assembly.

Figure 4.21: Measurement setup for the 1 - 20 GHz characterization.

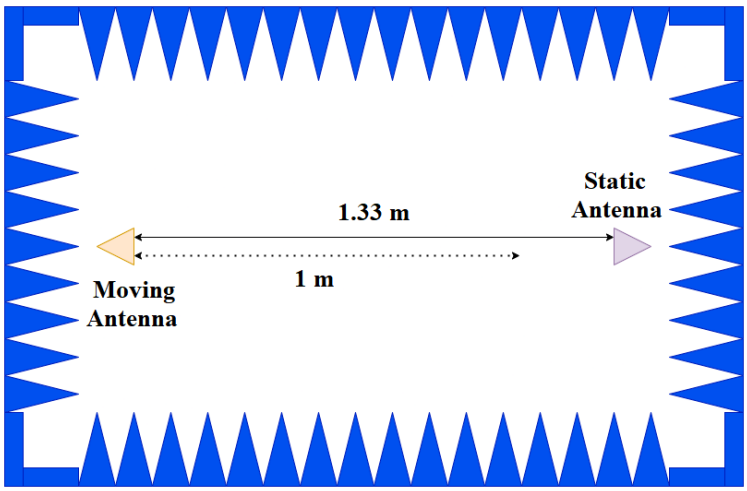


Figure 4.22: Setup diagram (top view).

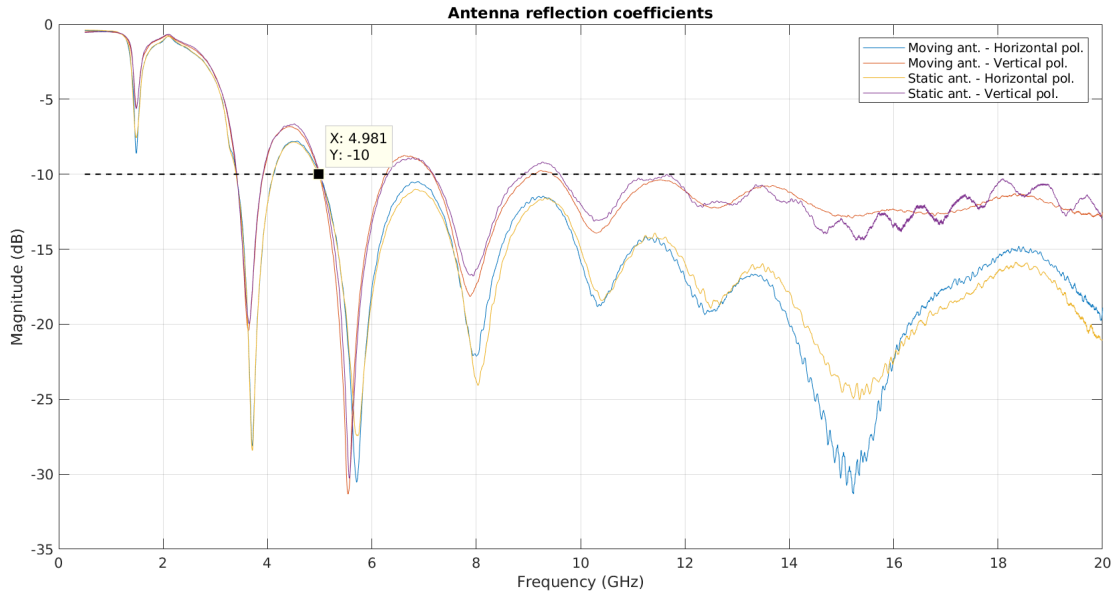


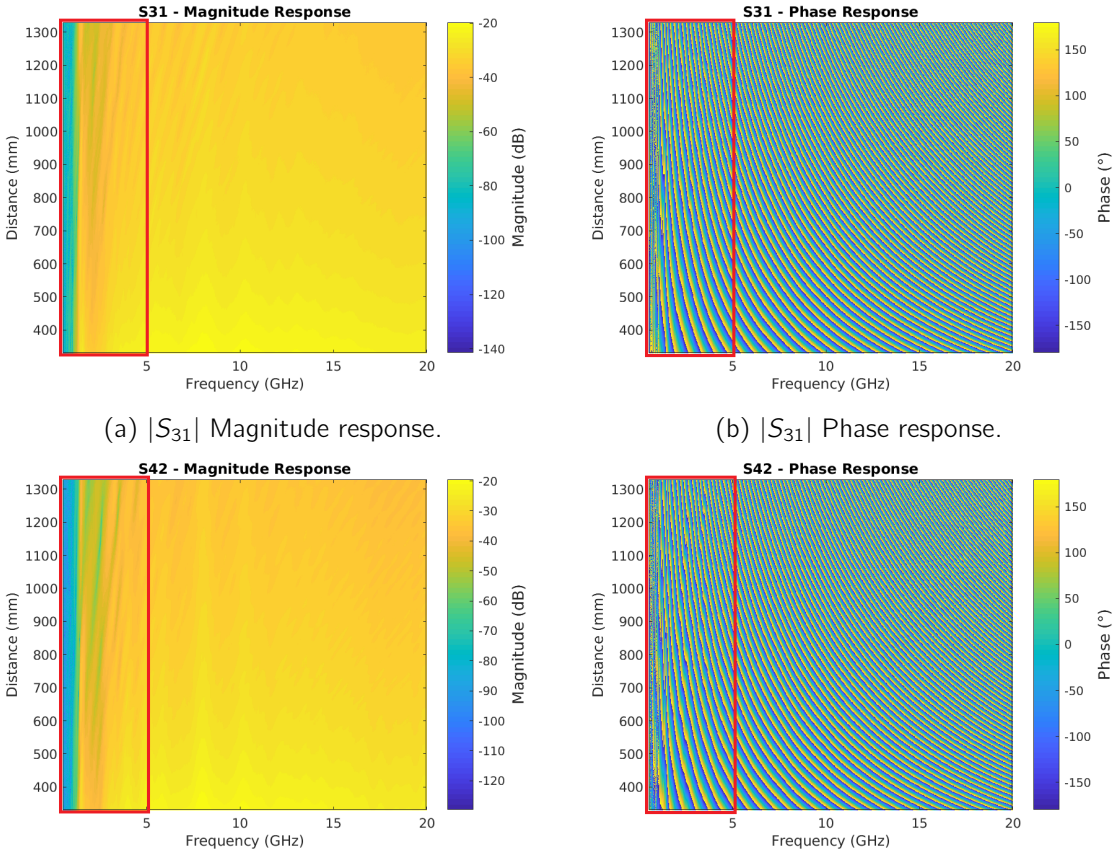
Figure 4.23: QRH0140 antenna reflection coefficients

datasheet. Due to this fact, the following result analysis is truncated from 5 to 20 GHz.

The results were subsequently truncated from 5 to 20 GHz. The transmission coefficients are presented in Fig. 4.25. The magnitude responses were normalized at the first measurement, 330 mm, in order to adjust the magnitude absolute scale into a relative one, which helps to visualize the data better. It is possible to observe in the magnitude response, shown in Fig. 4.25a and 4.25c, that the amplitude of the transmission coefficients presents some ripple at higher separation distances between the static and moving antenna, being more noticeable after 600 mm of travelled distance, and at lower frequencies (<14 GHz). This can be associated with the linear rail actuators, which are metallic, even though in this case, a different pattern in the ripple would be expected between the horizontal polarization ($|S_{31}|$) and the vertical polarization ($|S_{42}|$), which is not the case. Nevertheless, the absolute phase response, shown in Fig. 4.25b and 4.25d, seems to be very linear, despite the ripple in the magnitude.

An analysis of the S-parameters in delay domain has also been performed. The measurement data is initially in the frequency domain, then an Inverse Fast Fourier Transform (IFFT) is applied to it, converting it into the delay domain. Afterwards, the data in the delay domain is transformed to the distance domain, which is based on the time-of-flight (like radar). From the distance domain analysis of the reflection coefficient in the delay domain ($|S_{11}|$), shown in Fig. 4.26, one can observe the following. There are 2 well defined vertical lines around 0.5 m that represent internal reflections in the moving antenna (antenna connected to port 1 and 2). There are also 3 well defined diagonal lines in the plot that represent the reflections of the fixed antenna, and also from the back plane of the anechoic chamber. Note that the diagonal lines are set at roughly twice the separation distance between antennas, as this represents the total wave travel distance (like radar), as delay domain conversion is performed over the $|S_{11}|$ parameter.

Subsequently, if the distance domain analysis is performed this time over the transmission coefficient ($|S_{31}|$), shown in in Fig. 4.27, a similar result is observed. This time however, the internal reflections of the moving antenna (around 0.5 m) are not present. It is also



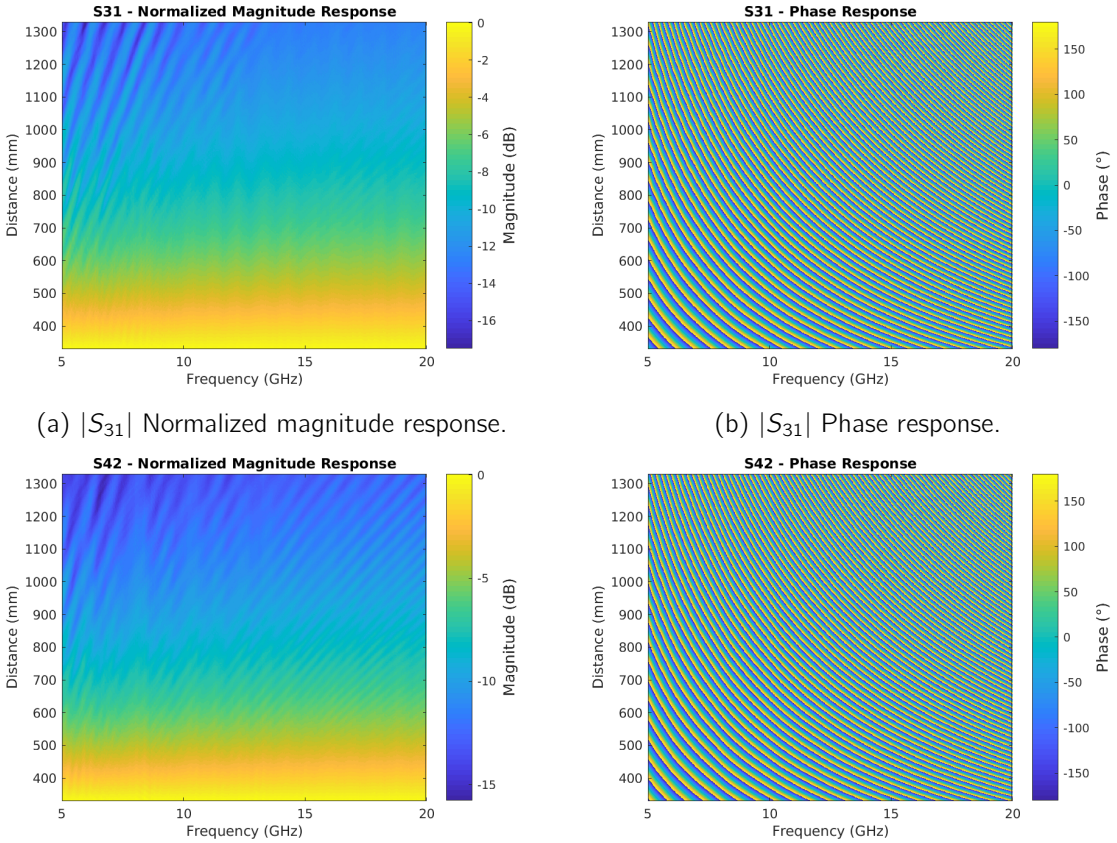
(a) $|S_{31}|$ Magnitude response.

(b) $|S_{31}|$ Phase response.

(c) $|S_{42}|$ Magnitude response.

(d) $|S_{42}|$ Phase response.

Figure 4.24: Transmission coefficients on both polarizations, with $|S_{31}|$ corresponding to the horizontal polarization and the $|S_{42}|$ corresponding to the vertical polarization.



(a) $|S_{31}|$ Normalized magnitude response.

(b) $|S_{31}|$ Phase response.

(c) $|S_{42}|$ Normalized magnitude response.

(d) $|S_{42}|$ Phase response.

Figure 4.25: Transmission coefficients on both polarizations, truncated from 5 to 20 GHz, with $|S_{31}|$ corresponding to the horizontal polarization and the $|S_{42}|$ corresponding to the vertical polarization.

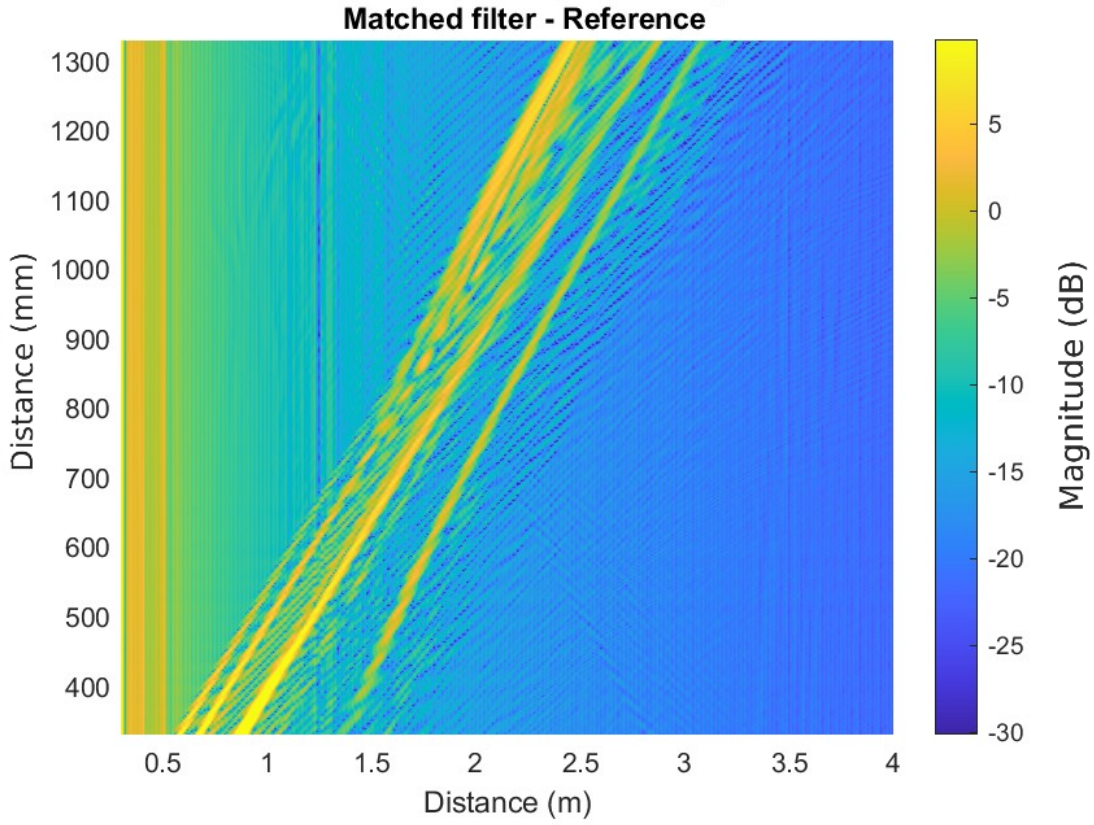


Figure 4.26: $|S_{11}|$ in the distance domain.

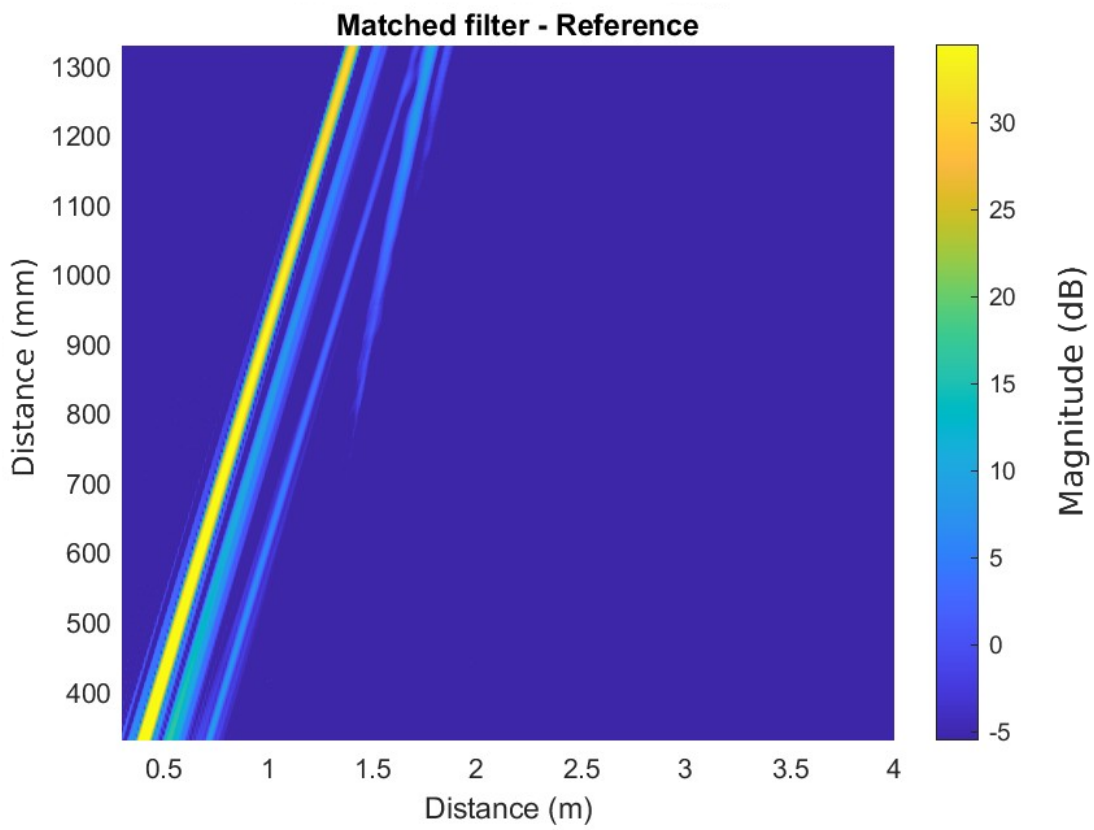


Figure 4.27: $|S_{31}|$ in the distance domain.

possible to observe in the yellow diagonal line, which is the direct component, that the distance reflection distance, on the X-axis, is proportional to the physical separation distance between antennas. The other diagonal lines in light blue are multipath components, internal reflections within the chamber or in the linear rail actuator.

This analysis is also interesting when observing the delay domain conversion of the static antenna ($|S_{33}|$), shown in in Fig. 4.28. The same diagonal lines appear in the plot, as reflections from the moving antenna and support rig, with some vertical lines (blur) at around 3.25 m. This is respective to the opposite back plane of the anechoic chamber, that is always constant throughout the measurements and the $|S_{33}|$ antenna is static. 3.25 m represents twice the distance between the static antenna and the opposite back plane of the chamber.

Lastly, a final analysis on the transmission coefficients was performed, Fig. 4.29 shows the transmission coefficients over a frequency sweep when the antennas are 1 m apart, while Fig. 4.30 shows the transmission coefficients over the distance between antennas at various frequencies, 5, 10, 15 and 20 GHz. In Fig. 4.29 it is possible to observe that the values of the transmission coefficients become stable after a frequency of around 8.5 GHz. Regarding the polarization, the horizontal one gives results with less ripple. It could be something related to the chamber geometry or caused by some reflection in the antenna support rig or in the linear rail actuator. Regarding the results with the distance, shown in Fig. 4.30, we can observe a ripple in the measurements from a certain point. For the highest frequencies it is more pronounced for the vertical polarization. As measurements started from the furthest

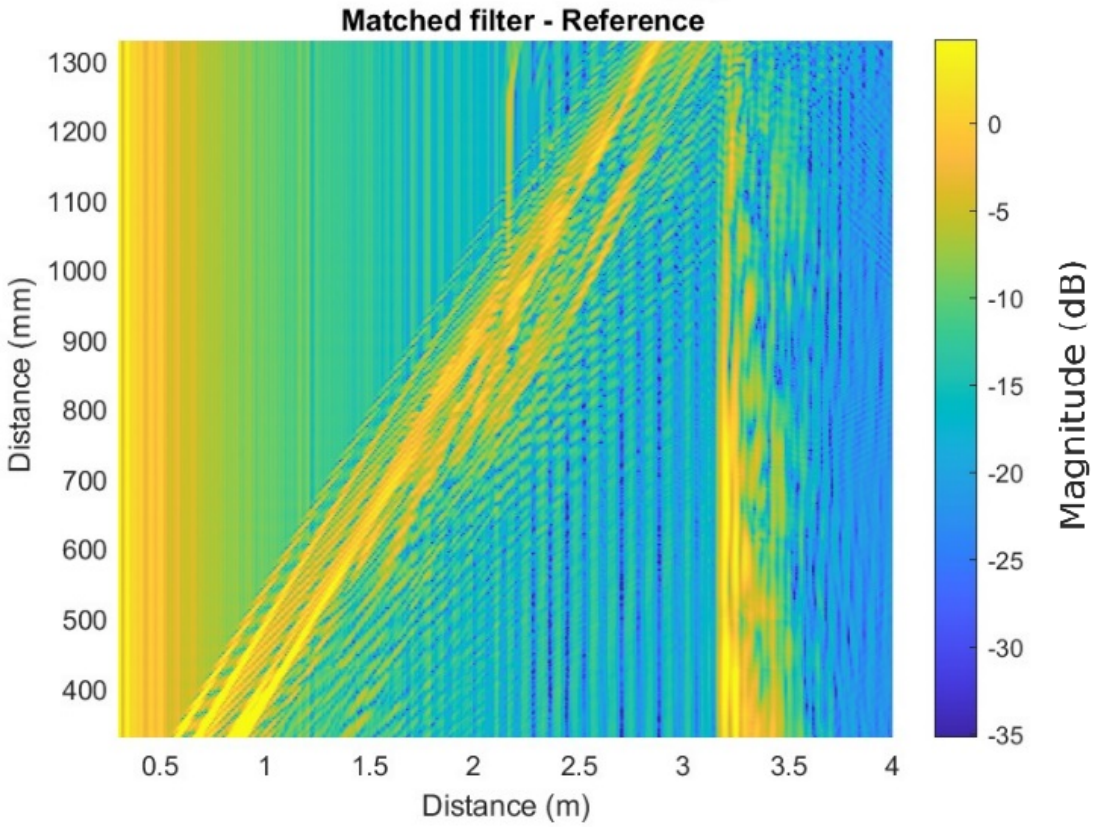


Figure 4.28: $|S_{33}|$ in the distance domain.

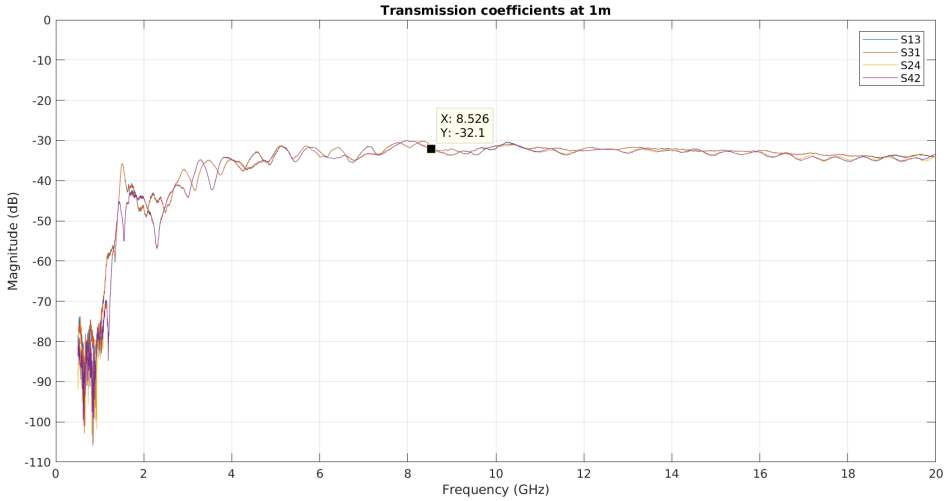


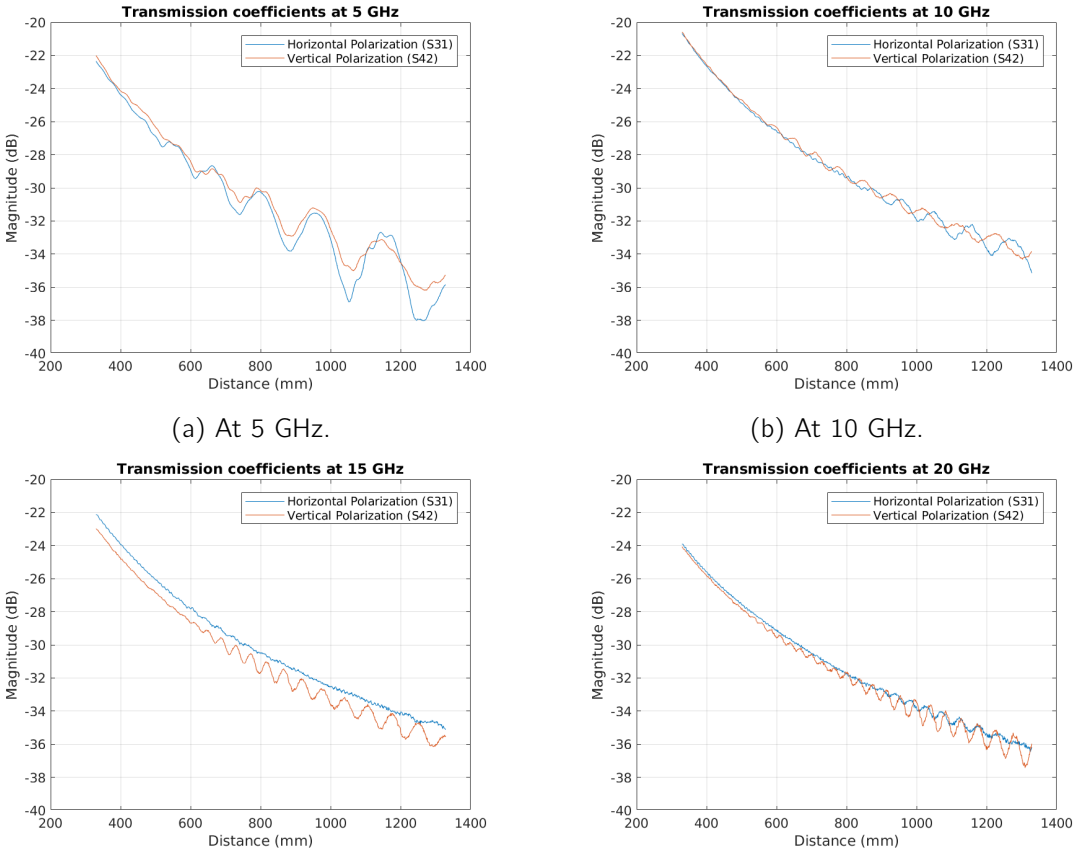
Figure 4.29: Transmission coefficients over a frequency sweep at 1 m of separation between antennas.

distance, we can rule out a problem of calibration, and think that the problem is caused by reflections in the linear rail actuator.

4.5.2 60 to 90 GHz

To characterize the anechoic chamber in the 60 - 90 GHz band the following equipment was used: C4420 VNA (which was presented in the previous subsection), CobaltFx-12 frequency extenders, MD249 Omnidirectional antenna and a WR-12 waveguide probe antenna. CobaltFx-12 is a frequency extender manufactured by Copper Mountain Technologies. It is a mmWave frequency extender that can convert signals from lower frequencies to higher frequencies enabling the testing of high-frequency circuits, in this particular case it converts the input RF frequency of the VNA from 5 to 7.5 GHz to operate from 60 to 90 GHz. The fact that this system works at such high frequencies the RF test port interface happens through a WR-12 waveguide, instead of a typical SMA connector, because waveguides conduct microwave energy at lower loss than coaxial cables. It delivers 2 - 5 dBm of power at the test port and has a dynamic range of 110 dB. The system requires a DC supply of 6 V and consumes 2.2 A of current, as specified in its technical datasheet [76]. It is ideal for antenna range measurements, material characterization, wafer S-parameter measurements, automotive radar, and sensor testing applications. The MD249-AA is a omnidirectional antenna manufactured by Flann Microwave. It has a functional frequency range from 50 to 70 GHz, with a nominal gain of 2 dB, as specified in its technical datasheet [77]. The omnidirectional antenna will be the moving antenna because we are looking for reflections from the chamber's walls, so we need to be able to receive signals from all of the possible angles. The static antenna is WR-12 waveguide probe antenna with 5 dBi of gain and has a working frequency range from 60 to 90 GHz.

The setup for these measurements can be seen in 4.31. The frequency extender on the right side of both pictures is the one with the static antenna, while the frequency extender on the left side is the one with the moving antenna. Just as in the 1 - 20 GHz characterization, the goal is to place both antennas at the center of the anechoic chamber, at 45 cm of height and at 45 cm from the lateral walls. The horn antenna was therefore connected to



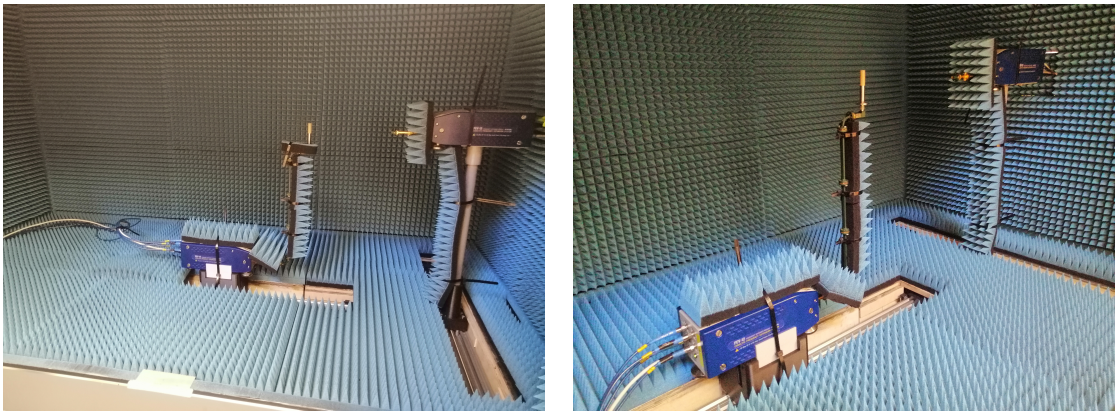
(a) At 5 GHz.

(b) At 10 GHz.

(c) At 15 GHz.

(d) At 20 GHz.

Figure 4.30: Transmission coefficients on both polarizations over distance at various frequencies.



(a) (b)

Figure 4.31: Measurement setup for the 60 - 90 GHz characterization.

the static frequency extender, and it was then placed on top of the same support rig used for the 1 - 20 GHz characterization, using a 3D printed adapter piece. However, for the moving frequency extender the approach needs to be different. Since the frequency extender weights 3.5 kg and has 22 cm in length, placing it on top of a 40 cm support rig would cause to much vibration, and at frequencies from 60 to 90 GHz where the wavelengths vary between 3 and 5 mm, it would led to inaccuracies in the measurements. To solve this issue, the frequency extender was attached, at the bottom, to the moving platform of the linear rail actuator, and waveguides were used to transmit the signals to the MD249-AA antenna. To achieve the 45 cm of height, 3 straight waveguides, each with a length of 12 cm, and 2 90° bend waveguides were used. The final assembly of the moving antenna system can be seen in Fig. 4.32. And since the omnidirectional antenna is in a vertical position it means that there's only going to be a vertical polarization in this measurement.

At the starting point both antennas are 96 cm apart, then the moving antenna will travel 95 cm over the linear rail whilst the VNA doing measurements after every 1 mm of traveled distance, essentially doing the same procedure as in the 1 - 20 GHz characterization, however the distance between antennas is now smaller. This as to due with the fact that the frequency extenders, with 22 cm in length, and also the waveguides, both take some space from the path that the moving antenna is going to be traveling on, thus reducing the effective distance between antennas. In Fig. 4.33 the diagram of the setup is shown, the line represents the distance between both antennas while the dotted line represents the distance that the moving antenna will travel. The static antenna was connected to the VNA on port 1, and the moving antenna was connected to port 2. The VNA was configured to do frequency sweeps from 60 to 90 GHz with 5001 measurement points.

From the reflection coefficients in both antennas, shown in Fig. 4.34, it is possible to conclude that both antennas are well matched for the 60 - 90 GHz frequency band, despite the ripple on frequencies above 75 GHz on the omnidirectional antenna.

The transmission coefficients are presented in Fig. 4.35. The magnitude response was normalized at the first measurement, at 10 mm, in order to adjust the magnitude absolute scale into a relative one, which helps to visualize the data better. It is possible to observe in the magnitude response, shown in Fig. 4.35a, that the amplitude of the transmission coefficients presents some ripple at higher separation distances between the static and moving antenna, being more noticeable after 600 mm of traveled distance. This can again be

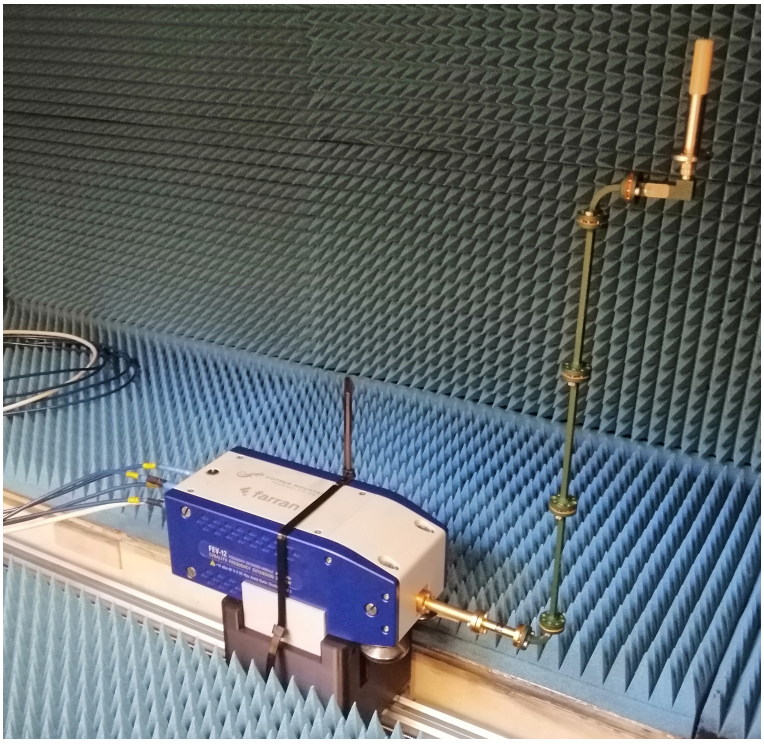


Figure 4.32: Moving antenna system.

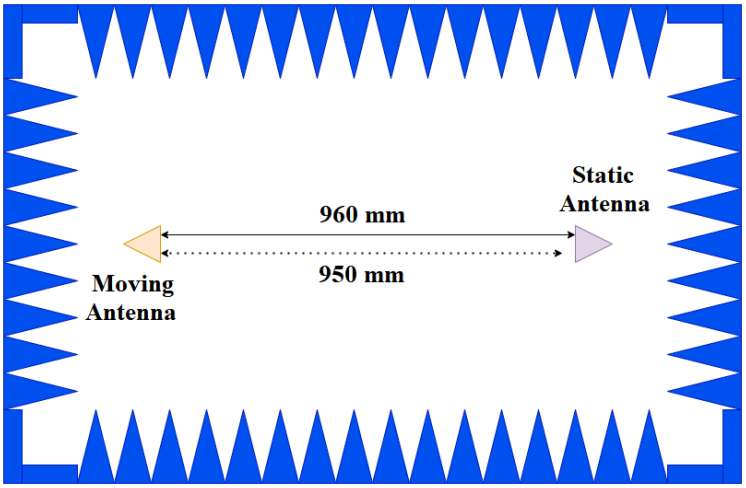


Figure 4.33: Setup diagram (top view).

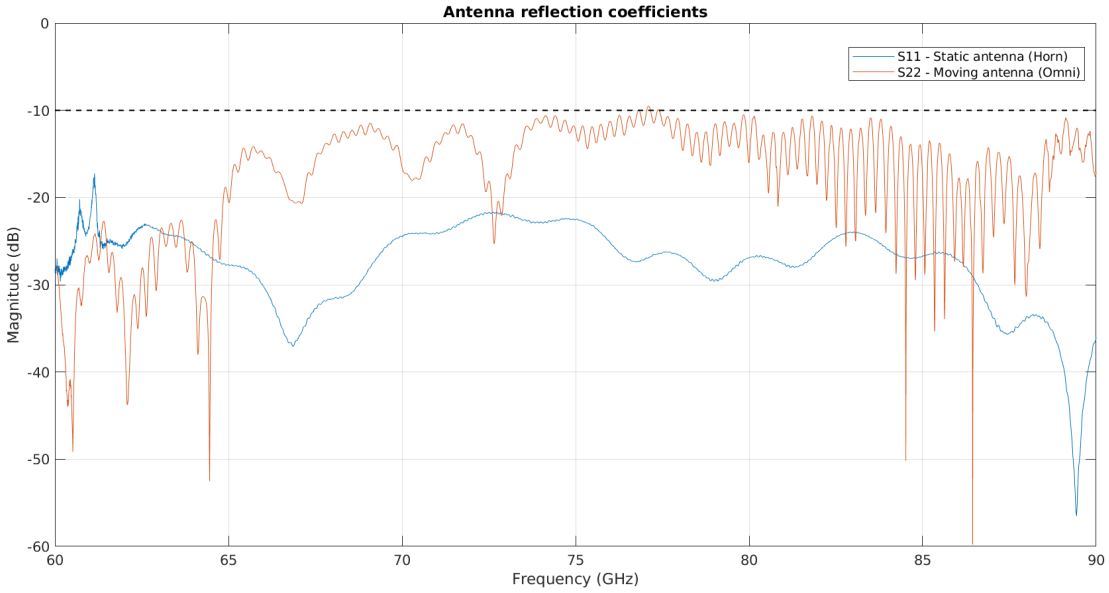
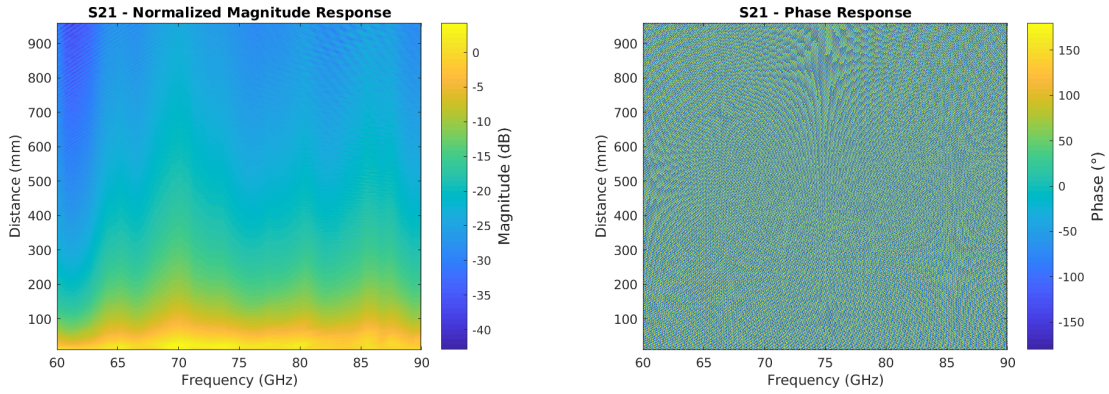


Figure 4.34: MD249-AA and horn antenna reflection coefficients.



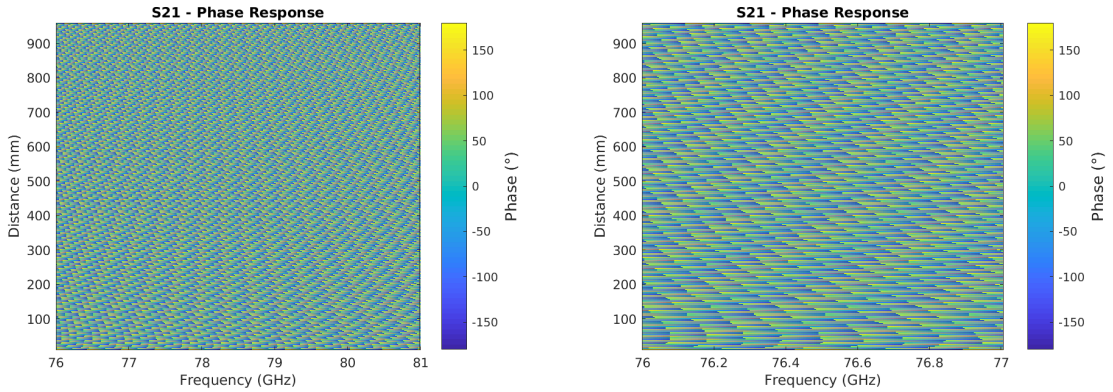
(a) $|S_{21}|$ Normalized magnitude response.

(b) $|S_{21}|$ Phase response.

Figure 4.35: Transmission coefficients

associated with the linear rail actuators, which are metallic, and because of the ripple in the reflection coefficient of the omnidirectional antenna above 75 GHz, which might be caused by internal reflections within the chamber, creating multipath components. The absolute phase response, shown in Fig. 4.35b, presents so much variation in this broad frequency band that it is very difficult to conclude anything about its linearity. The phase response data was then truncated from 76 to 81 GHz, covering the frequency band used for automotive radar applications, and also from 76 to 77 GHz, in order to better visualize its changes and is shown in Fig. 4.36.

However, even still, it is difficult to make viable conclusions regarding the phase response. So, in order to overcome this, it was decided to observe the phase change over a smaller distance, roughly at the center of the anechoic chamber, and at certain frequencies, in this case covering the automotive frequency band, from 76 to 81 GHz. In Fig. 4.37 it is shown the phase response for those frequencies. There is also another possible cause for this issue,



(a) $|S_{21}|$ Phase response from 76 to 81 GHz. (b) $|S_{21}|$ Phase response from 76 to 77 GHz.

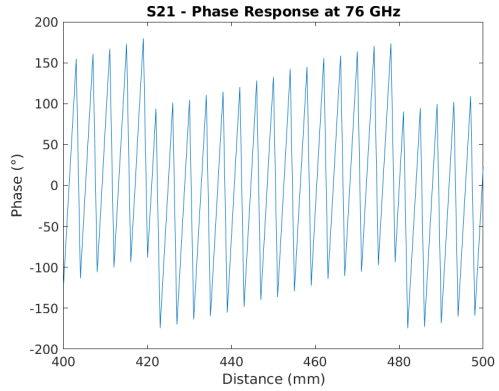
Figure 4.36: Transmission coefficients - truncated phase response.

which is the fact that the spatial resolution is 1 mm. At 75 GHz, for example, the wavelength of the signal is roughly 4mm, which means that by taking measurements from 1 to 1 mm we observe a phase shift of almost 90°. At these frequencies it is, however, very difficult to achieve a higher spatial resolution because of the mechanical oscillations within the linear rails and waveguide extensions.

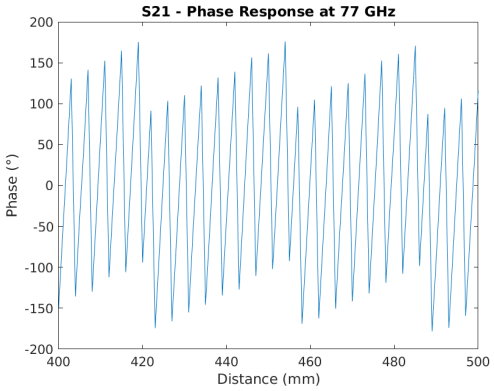
An analysis of the S-parameters in delay domain was also performed for this frequency band. From the distance domain analysis of the reflection coefficient in the delay domain ($|S_{11}|$), shown in Fig. 4.38, one can observe that there is 1 well defined vertical line around 0.1 m that represents internal reflections in the static antenna, while the other vertical lines in lighter blue are reflections in the linear rail as well as in the aluminium shielding. There is also 1 diagonal line in the plot that represents the reflections on the moving antenna. Note, again, that the diagonal line is set at roughly twice the separation distance between antennas, as this represents the total wave travel distance (like radar), as delay domain conversion is performed over the $|S_{11}|$ parameter.

Subsequently, if the distance domain analysis is performed this time over the transmission coefficient ($|S_{21}|$), shown in Fig. 4.39, a similar result is observed. This time however, the internal reflections of the static antenna (around 0.1 m) are not present. It is also possible to observe in the diagonal line, which is the direct component, that the distance reflection distance, on the X-axis, is not proportional to the physical separation distance between antennas, it shows an offset of around 45 cm. These 45 cm of offset are caused by the length of the waveguides used to place the omnidirectional antenna at half of the height of the anechoic chamber, as previously explained. Since the VNA was calibrated at the flange of the frequency extender's waveguide, the external waveguides were not used during the VNA calibration and therefore the time of flight in the waveguides sums up with the time of flight between antennas. This time of flight is proportional to the distance reflection distance showed in the graph. Finally, the other diagonal lines in light blue are multipath components, internal reflections within the chamber or in the linear rail actuator.

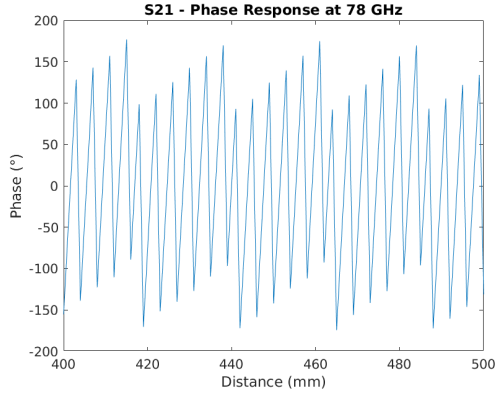
This analysis is also interesting when observing the delay domain conversion of the moving antenna ($|S_{22}|$), shown in in Fig. 4.40. Since this antenna is omnidirectional there are multiple vertical lines that correspond to reflections in the aluminium foil from the shielding in the walls of the anechoic chamber, the most predominant/stronger being around 1.1 m which corresponds roughly to the double of the distance between the moving antenna and



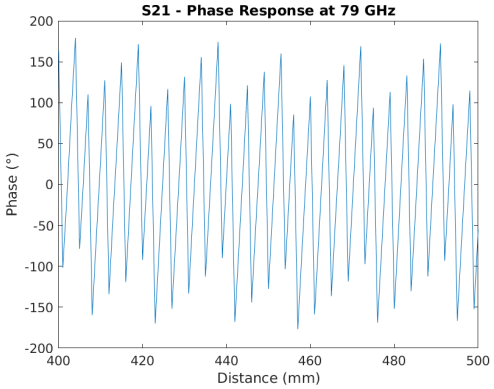
(a) $|S_{21}|$ Phase response at 76 GHz.



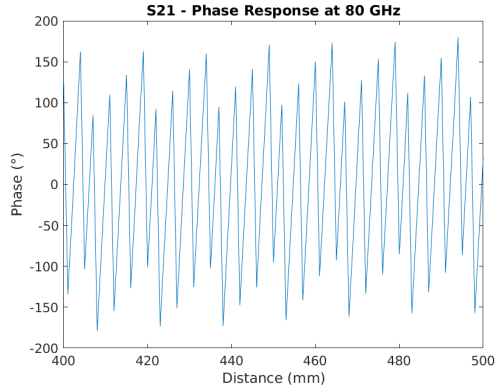
(b) $|S_{21}|$ Phase response at 77 GHz.



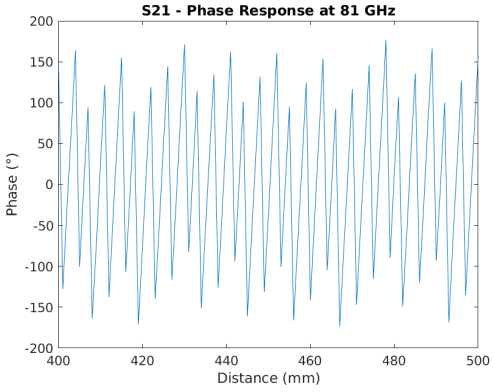
(c) $|S_{21}|$ Phase response at 78 GHz.



(d) $|S_{21}|$ Phase response at 79 GHz.



(e) $|S_{21}|$ Phase response at 80 GHz.



(f) $|S_{21}|$ Phase response at 81 GHz.

Figure 4.37: Transmission coefficients - phase response from 400 to 500 mm.

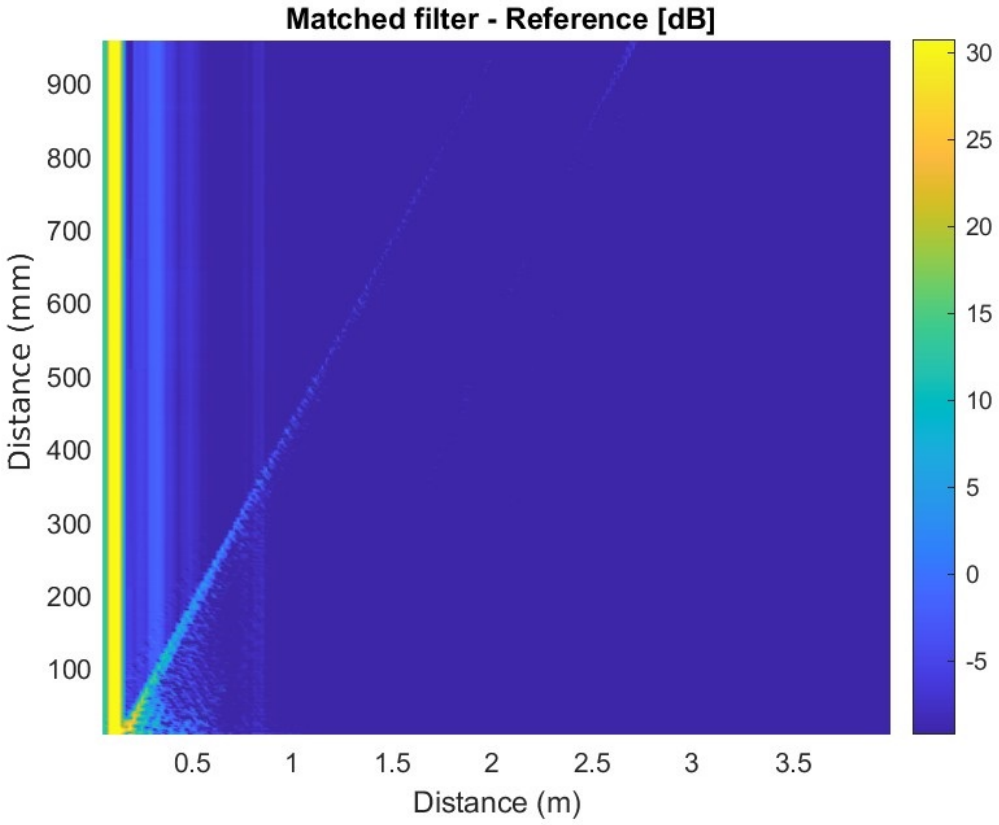


Figure 4.38: $|S_{11}|$ in the distance domain.

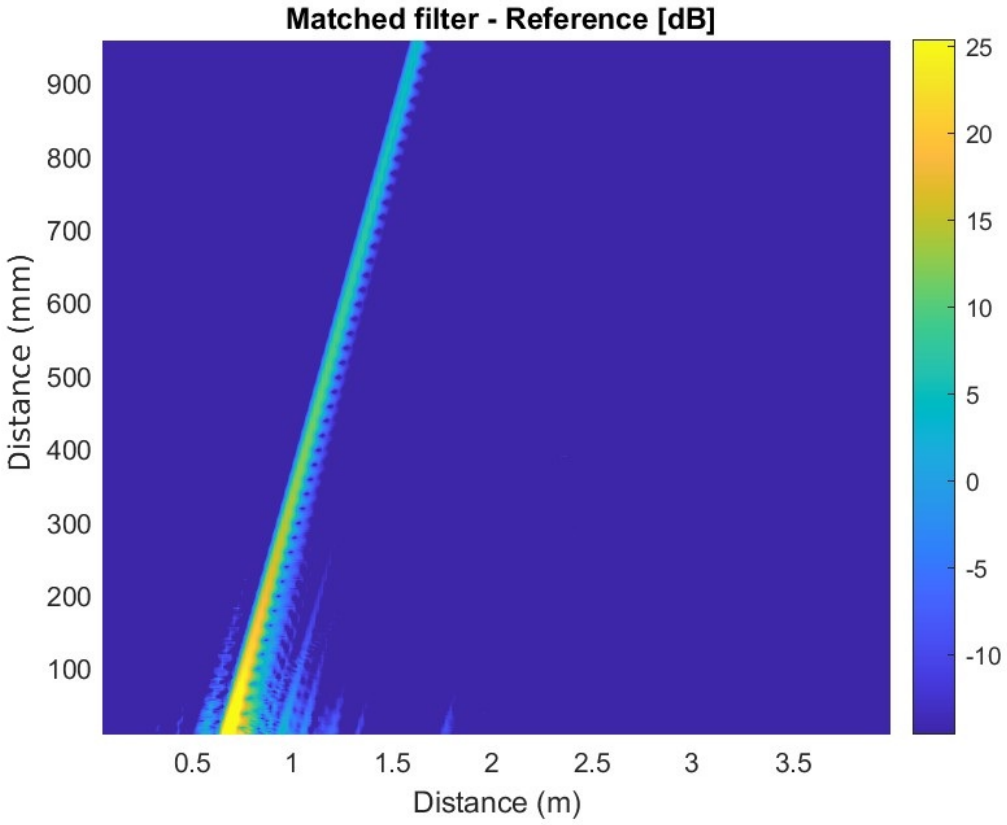


Figure 4.39: $|S_{21}|$ in the distance domain.

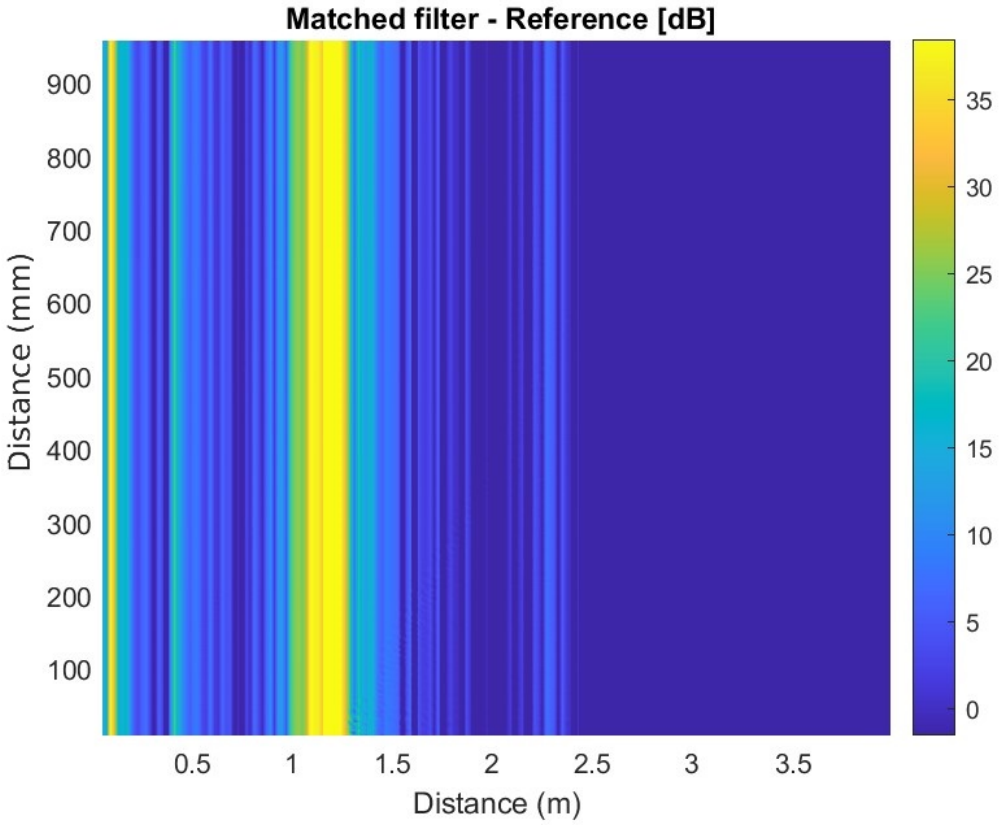
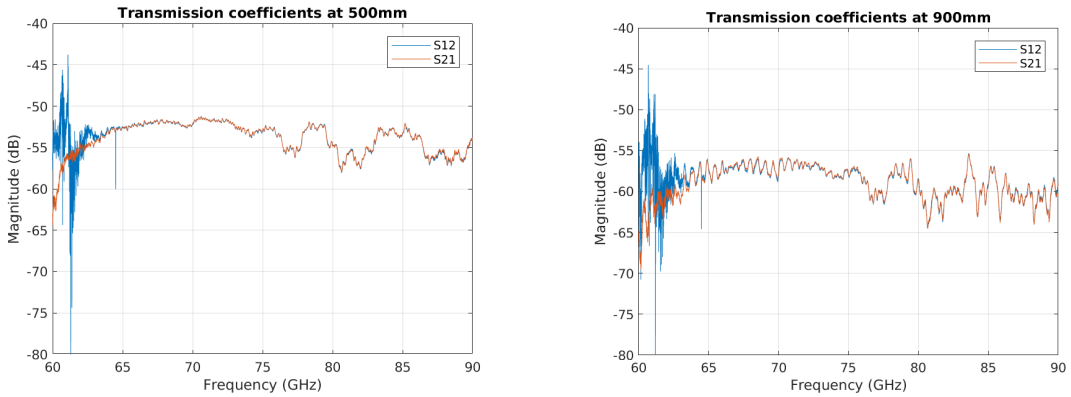


Figure 4.40: $|S_{22}|$ in the distance domain.

the walls that are parallel to the linear rail. These lines at around 1.1 m correspond to the direct reflection in the walls, i. e. when the waves travel from the antenna to the wall and back covering the smallest distance possible. Then the weaker vertical lines correspond to the "diagonal" reflections, where the waves are reflecting in the walls at an angle, covering more distance and consequently having a weaker amplitude. Besides that, there is a vertical line around 0.1 m that represents internal reflections in the moving antenna, and there is also a vertical line around 0.4 m that probably corresponds to the aluminium linear rail.

Lastly, a final analysis on the transmission coefficients was performed, Fig. 4.41 shows the transmission coefficients over a frequency sweep when the antennas are 500 and 900 mm apart, while Fig. 4.42 shows the transmission coefficients over the distance between antennas at various frequencies, 65, 70, 75, 80, 85 and 90 GHz. In Fig. 4.41 it is possible to observe that the values of the transmission coefficients are relatively stable from 65 to 75 GHz, however above 75 GHz there's a lot of ripple which can be somewhat explained by the ripple in the reflection coefficient of the omnidirectional antenna. Below 65 GHz we found, through multiple measurements, that the frequency extenders perform rather poorly, which we see once more in these measurements. Also, there is more ripple present at 900 mm of separation between antennas, which can be caused by multipath components that are, somehow, more noticeable at that distance. Regarding the results with the distance, shown in Fig. 4.42, we can observe a ripple in the measurements from a certain point, at around 600 mm. The problem might be once again caused by multipath components, caused by reflections in the linear rail actuator and in the aluminium shielding.



(a) At 500 mm.

(b) At 900 mm.

Figure 4.41: Transmission coefficients over a frequency sweep at 500 and 900 mm of separation between antennas.

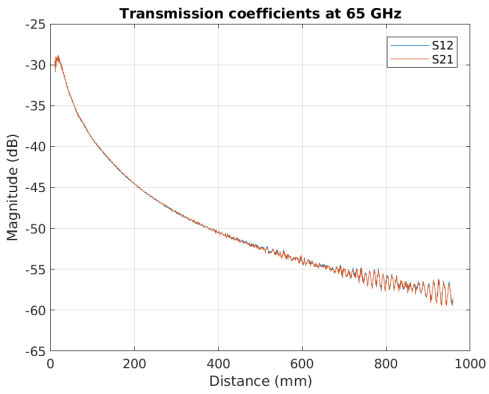
4.6 Radar Applications and Measurements Results

The anechoic chamber was used, so far, for 3 distinct radar measurements, the first being for its calibration, the second being a characterization of polymer properties for bumpers and the third being a SAR imaging measurement. This section will present those measurements.

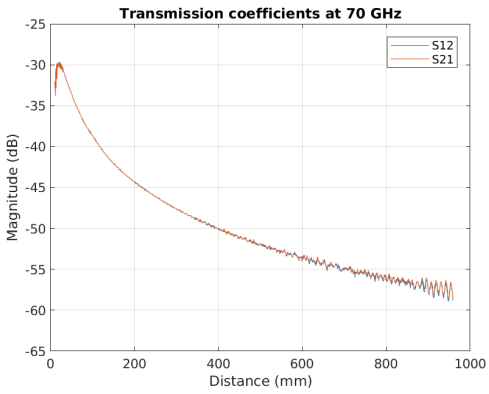
4.6.1 360° Radar Calibration

This subsection presents the calibration of the 360° radar inside the CATR. Radar calibration is of the utmost important, as it ensures that the performance of the radar front end is maintained across temperature and process variations [78] and allows for repeatability and accuracy in target detection. If the user wants to calibrate the radar he needs to enable the calibration measurement via the "measureRangeBiasAndRxChanPhase" command in the configuration file. This command is explained in full detail in 3.2.2, and the calibration in 3.2.4. The calibration process starts with placing a strong reflector in front of the radar sensor at a know range and then enable the calibration measurement in the "measureRangeBiasAndRxChanPhase" command as well as adding the target range and search window to the command. The value for the search window was chosen as 15 cm, which is 4 times the resolution of the radar, giving it a narrow window for search, from 92.5 cm to 107.5 cm. Therefore the command sent for calibration is "measureRangeBiasAndRxChanPhase 1 1.0 0.15". In Fig. 4.43 it is shown the setup and the setup diagram for the radar calibration.

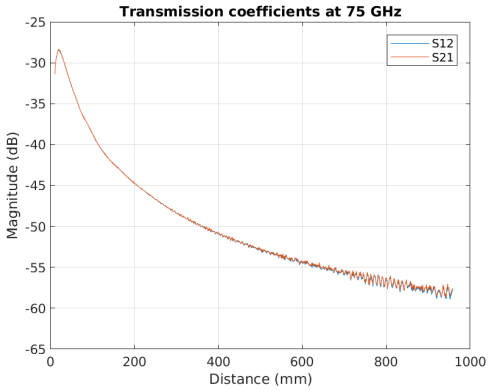
The calibration measurement was done for the 3 radars in the 360° radar prototype, where the 360° radar was rotated 120° between each measurement, in order for each radar to be facing the corner reflector. The range bias for each radar is presented in Table 4.1, while the gain and phase compensation coefficients are shown in Fig. 4.44. Finally, the compensation values were included in the configuration file, effectively calibrating the radars, and the calibration measurement was disabled in the configuration file, to avoid a new calibration on the radar startup.



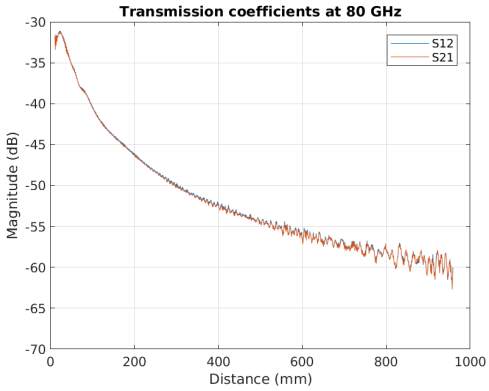
(a) At 65 GHz.



(b) At 70 GHz.



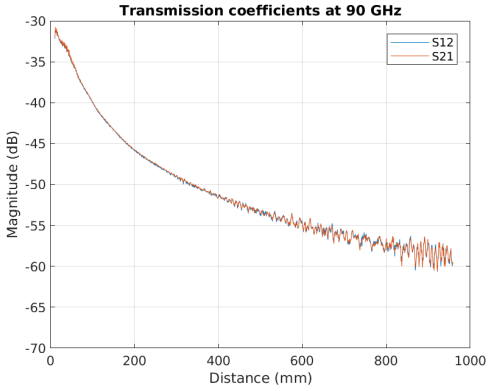
(c) At 75 GHz.



(d) At 80 GHz.

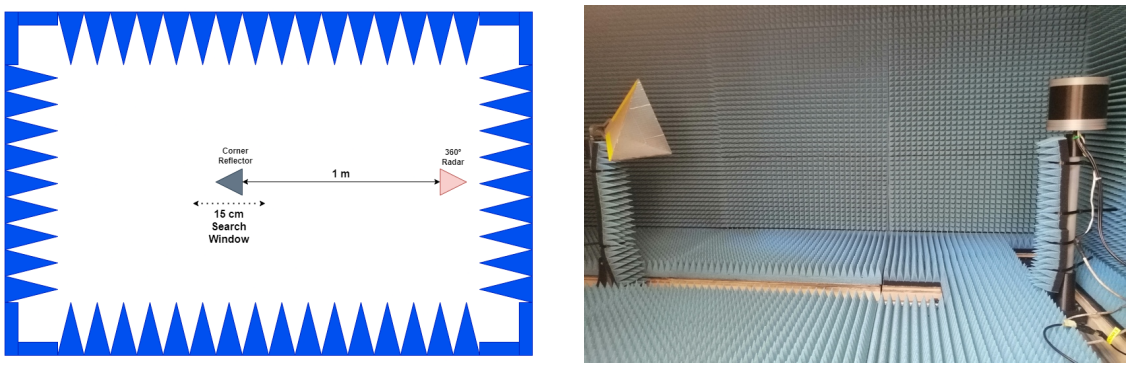


(e) At 85 GHz.



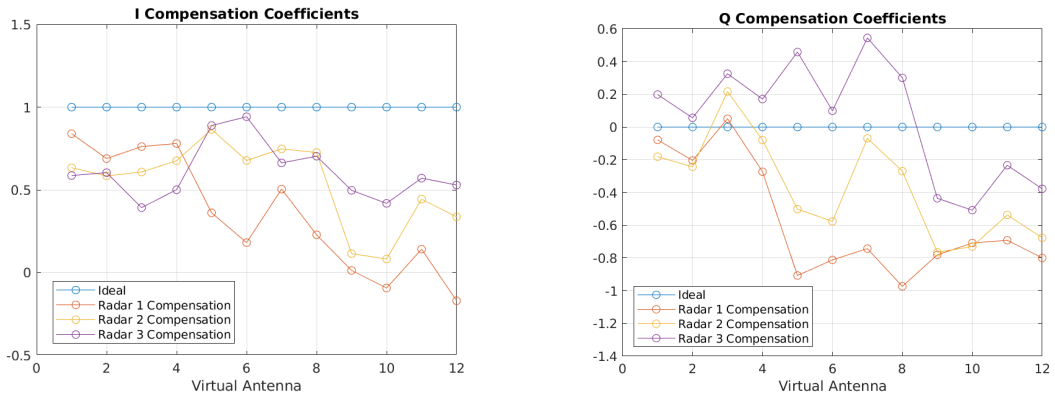
(f) At 90 GHz.

Figure 4.42: Transmission coefficients over distance at various frequencies.



(a) Calibration setup diagram. (b) Calibration setup.

Figure 4.43: Setup for the 360º radar calibration.

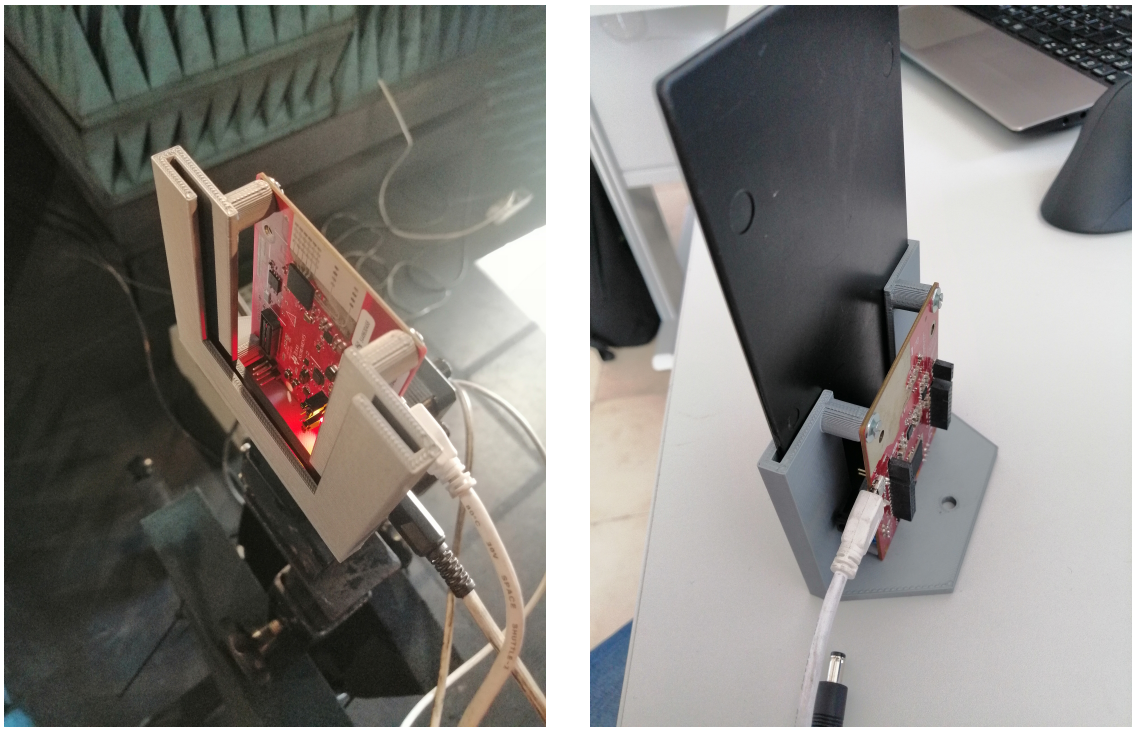


(a) I compensation coefficients. (b) Q compensation coefficients.

Figure 4.44: Compensation coefficients obtained in the calibration measurement.

Radar 1	Radar 2	Radar 3
0.0643150	0.0594789	0.0603995

Table 4.1: Range bias from each radar (in meters).



(a) Support rig with no sample. (b) Support rig with a polymer sample.

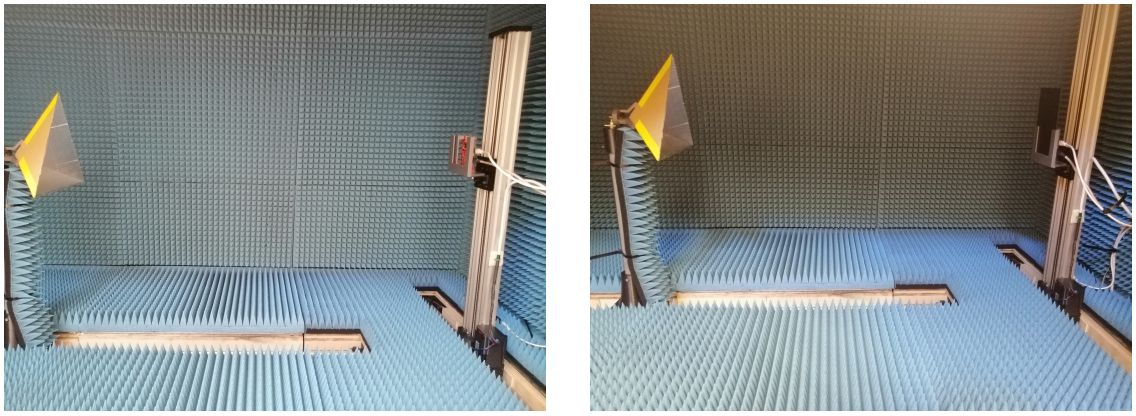
Figure 4.45: Radar support rig for the samples.

4.6.2 Characterization of polymer properties for bumpers

This subsection presents the characterization of bumper polymers in order to optimize radar transparency. The bumper characterization was conducted using a radar rather than a VNA, as the focus of this work was on radar system development and the design and construction of the anechoic chamber. Additionally, another researcher involved in PAC project was responsible for characterizing these polymers using a VNA. While we collaborated, this task was outside of the scope of my work.

A thermoplastic injection moulding company, with main activity in the automotive industry, also involved in PAC project, sent us 6 different polymer samples of which bumpers can be made of, in order to evaluate the impact that the bumper has on target detection when a radar is located behind it. These polymer samples are named BMU139, Compound8500, ED113EAU, PPC7810B, PPT10 and XM1T11. In order to test them a 3D printed support rig with a sample slot was designed, as it is shown in Fig. 4.45. With this rig it is possible to easily slide in and out the polymer samples, making it very simple to test a lot of different samples in a short time.

Several measurements were conducted in order to characterize the impact that a bumper polymer has in the detection of a target. The results are then presented in a range profile graph. Radar range profiles are obtained by transmitting a radar signal that comprises a wide



(a) Without polymer sample. (b) With polymer sample.

Figure 4.46: Setup for the radar characterization of polymer samples.

range in frequency, using either a single pulse (a chirp), or a series of pulses with increasing frequency. A range profile is defined as the squared magnitude of the coherent complex radar returns, after optional processing [79].

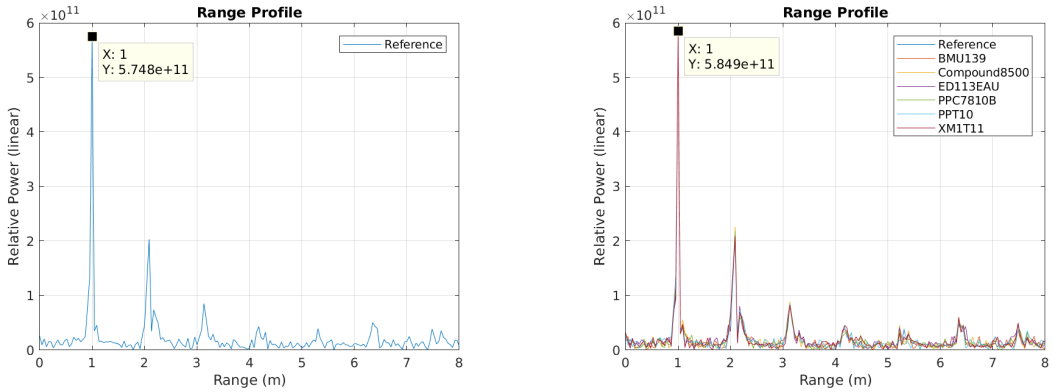
These measurements were conducted using the setup shown in Fig. 4.46, which is a fixed system setup, were both the radar and the target, a aluminium trihedral corner reflector, are static 1 m apart.

The reference measurement consists of the radar and the target 1 m apart with no obstructions in between. Ten radar acquisitions were then obtained and its values averaged in order to create the range profile graph shown in Fig. 4.47a. It is possible to observe that the radar makes the correct detection of the corner reflector at 1 m, the highest peak of the graph. The others peaks seen in the graph, at ranges close to multiples of 1 m, are multiple reflections caused by the signals that are reflected on the corner reflector, then reflected on the aluminium linear rail and then again on the corner reflector until they are finally received by the radar, causing multiple "ghost targets".

Afterwards, the same type of measurement was conducted, this time adding a polymer sample in front of the radar to see its impact on the detection. 6 different polymer samples, provided by a company working on PAC project as well, were tested to measure its impact on the detection. The results are shown in Fig. 4.47b as a graph with overlapped range profiles, each corresponding to a different polymer sample. It is possible to observe that the all of the range profiles overlap almost perfectly with one another, which leads us to conclude that the polymers have no significant impact on the correct detection of the target.

4.6.3 SAR Imaging

In this subsection a SAR imaging measurement inside the CATR is going to be presented. In recent years, the demand for high resolution imaging in ADAS lead to the use of SAR imaging in automotive vehicles, some of these works [80–83] present approaches, methodologies and experimentation using SAR imaging in automotive applications. Since SAR is not the scope of this work, it will only be explained briefly and not in full theoretical detail, for that the following works [84–88] provide exceptional information on the subject. The SAR imaging technique is a technique used to create 2D images or 3D reconstructions of objects [89]. SAR is an imaging radar mounted on a moving platform, typically with movement over 2 or



(a) Reference measurement. (b) Polymer measurement results overlapped.

Figure 4.47: Range profiles of the reference and sample polymers.

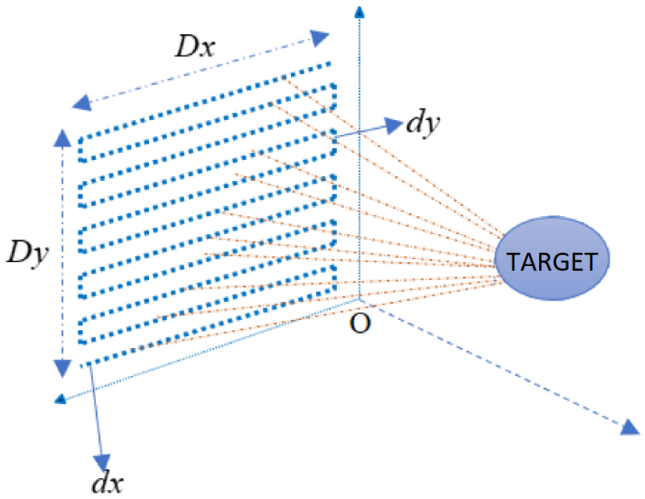


Figure 4.48: Geometry of the SAR imaging configuration.

more axis, on which the motion of the radar antenna over the target region provides a finer spatial resolution than conventional stationary radars. Similar to a conventional radar, EM waves are sequentially transmitted and the backscattered echoes are collected by the radar antenna. In SAR the consecutive time of transmission/reception translates into different positions due to the platform movement [90]. The distance that the radar travels over a target creates the large synthetic antenna aperture. Typically, the larger the aperture, the higher the image resolution will be. This allows SAR to create high-resolution images with comparatively small physical antennas. In Fig. 4.48 it is possible to observe the geometry concept of the SAR imaging configuration, where Dx and Dy correspond to the width and height, respectively, of the synthetic aperture, while dx and dy correspond to the spatial resolution of width and height, respectively. The radar antenna will travel through that scanning trajectory while taking measurements. This will result in a (Dx/dx) x (Dy/dy) matrix where in each position a radar range profile is stored, effectively creating a 3D, or multidimensional, data matrix. This data matrix is shown in Fig. 4.49, where the horizontal points correspond to Dx/dx, the vertical points correspond to Dy/dy and the delay domain samples to the radar range profiles.

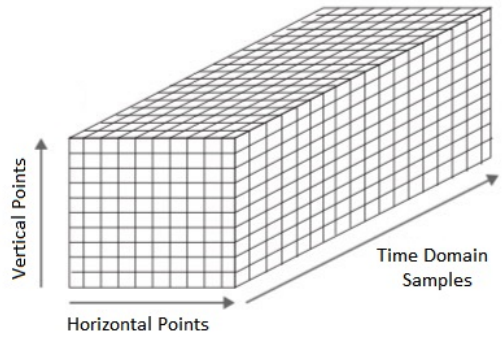
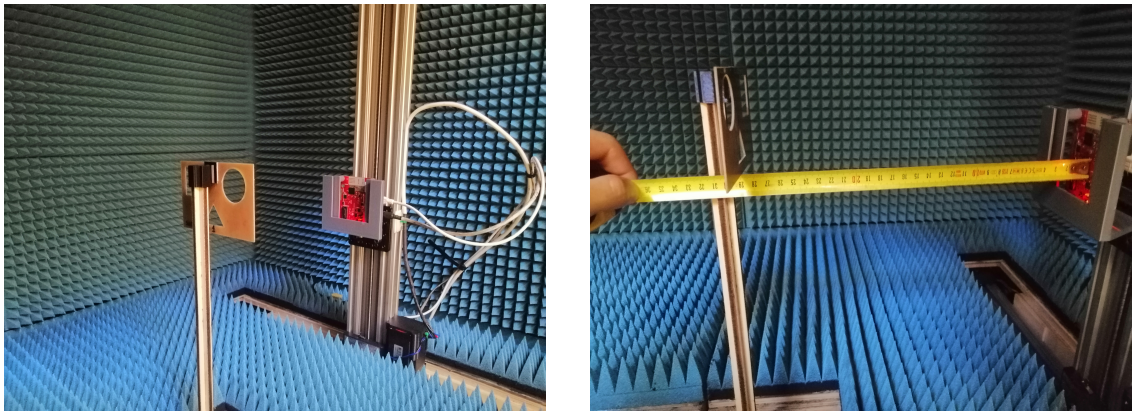


Figure 4.49: SAR imaging radar 3D data matrix.

Remarkably, in [91] the authors explore the virtual antenna array concept of 4D MIMO radar sensors and present near-field SAR working testbeds, using low-cost radar sensors, such as the AWR1443BOOST from TI. The authors from [91] even provide a full tutorial [92] with acquisition and processing code scripts for their testbeds in the main author's GitHub profile [2].

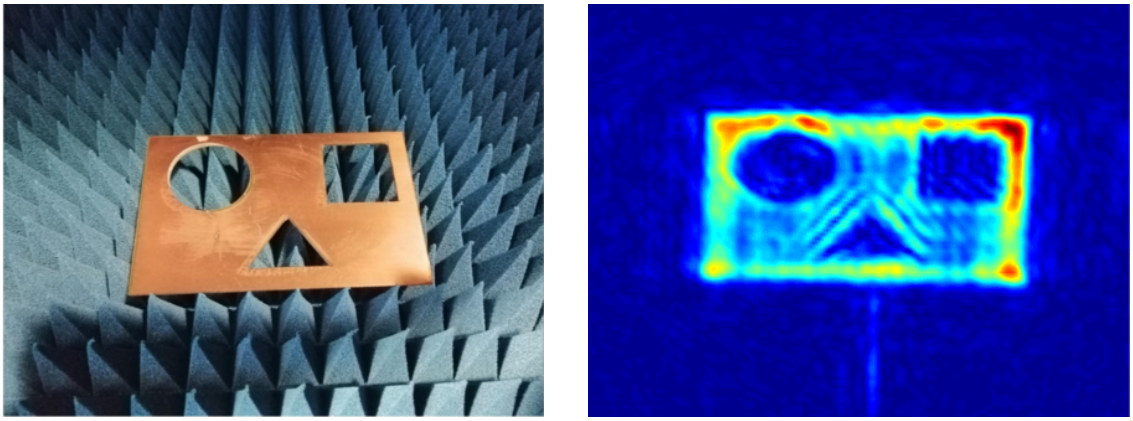
In order to recreate the results presented in [91], a script for radar acquisition and positioning control was created, in order to work with our specific systems such as, the anechoic controlling system (for the linear rail actuators) and the IWR1642BOOST radar sensor from TI. Both the radar sensor and the anechoic controlling system were connected to a computer via USB and the acquisition and positioning script was running on MATLAB. Once the measurement is finished a SAR imaging 3D data matrix, such as the one shown in Fig. 4.49, is stored in the workplace. This data matrix then serves as the input for the main SAR function provided by the [91] article's author. However this function needed to be slightly altered given the fact that the author used the TSW14J56EVM, which is a high-speed raw data capture board, in order to capture the complex signals from the radar itself. This raw data capture board is, however, very expensive and is not as easy to get as a simple radar sensor such as the IWR1642BOOST. The main goal is to try to achieve the same result using only the radar sensor, which is capable of outputting a range profile via USB. This range profile is transmitted as an array of I and Q 16-bit samples, and the length of this array is equal to the chosen number of ADC samples during radar configuration. The modification on the main SAR function was on how the object was detected in the data. The author's method was to find the object's corresponding peak in the FFT of the beat frequency by calculating it based on some parameters that were used to configure the TSW14J56EVM capture board, such as the sampling rate, sampling period, frequency slope and instrument delay for range calibration. The modification was to simply scan the radar data matrix to find the peaks in the beat frequency FFT's and just estimate the object range. Regarding the setup used for the signal acquisition, a linear rail actuator was placed on top of one of the anechoic chamber's linear rail actuators in order to achieve horizontal and vertical movement. The radar was attached to the vertical linear rail actuator using a 3D printed support rig. The target object, a 80 x 120 mm PCB sample with some holes in the form of basic geometry shapes, was placed at the center of the chamber, at roughly 29 cm from the radar. The radar will then scan an area of 200 x 200 mm, aligned with the center of the

[2] `https://github.com/meminyanik/MIMO-SAR-mmWave-Imaging-Toolbox` [Accessed on the 23rd of October of 2023]



(a) (b)

Figure 4.50: SAR imaging setup.



(a) SAR PCB sample.

(b) SAR image reconstruction of the PCB sample.

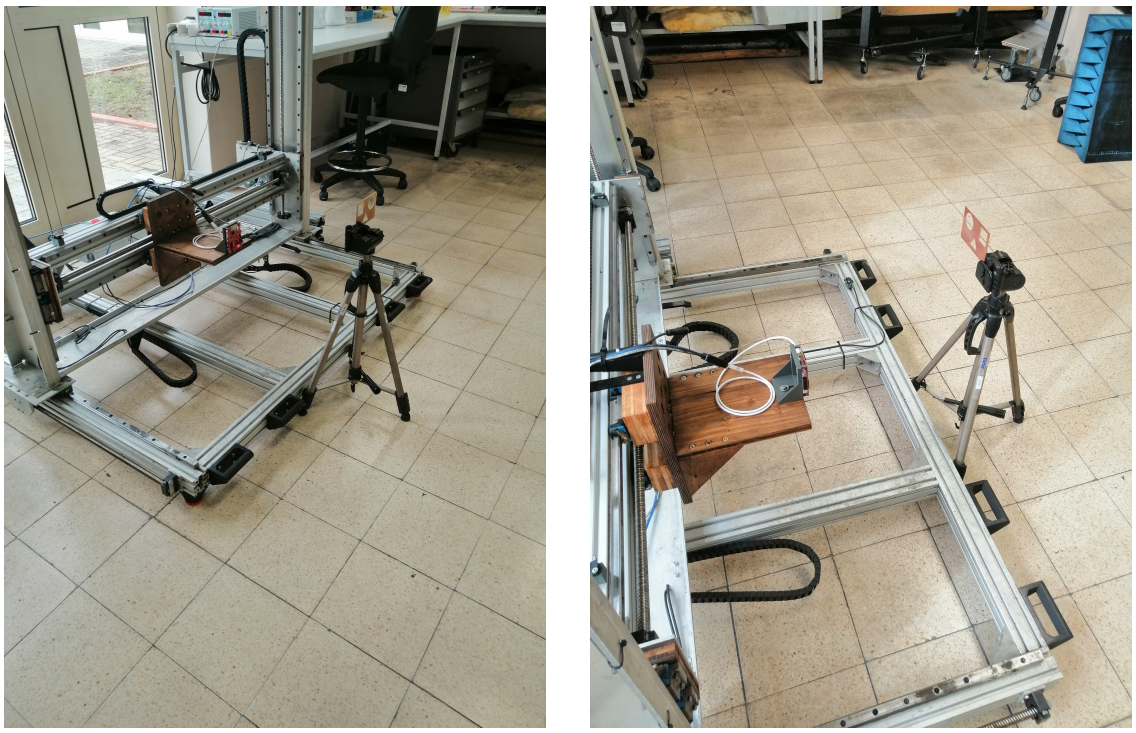
Figure 4.51: SAR measurement sample and image reconstruction result.

target object, with a spatial resolution, dx and dy, of 1 and 2 mm respectively. The setup can be seen in Fig. 4.50.

After the acquisition, the 3D data matrix was stored and served as the input for the SAR image reconstruction main function. In Fig. 4.51a it is possible to see the PCB sample used in this measurement and in Fig. 4.51b it is shown its reconstruction.

The same PCB sample was used in another SAR measurement, this time performed on a robust 3D antenna positioner, which serves for comparison. This measurement setup can be seen in Fig. 4.52 and the resulting image reconstruction can be seen in Fig. 4.53.

As it can be observed, both reconstructed images display a very good resolution and the PCB sample can be seen in detail, not only proving that this technique is really impressive when it comes to high-resolution radar imaging, but also that the linear rail actuators from the anechoic chamber can provide millimetric precision and a steady movement to fulfill the needs of a SAR measurement. Overall, this technique shows impressive results and is very promising for automotive radar imaging applications.



(a) (b)

Figure 4.52: SAR imaging setup using a 3D antenna positioner.

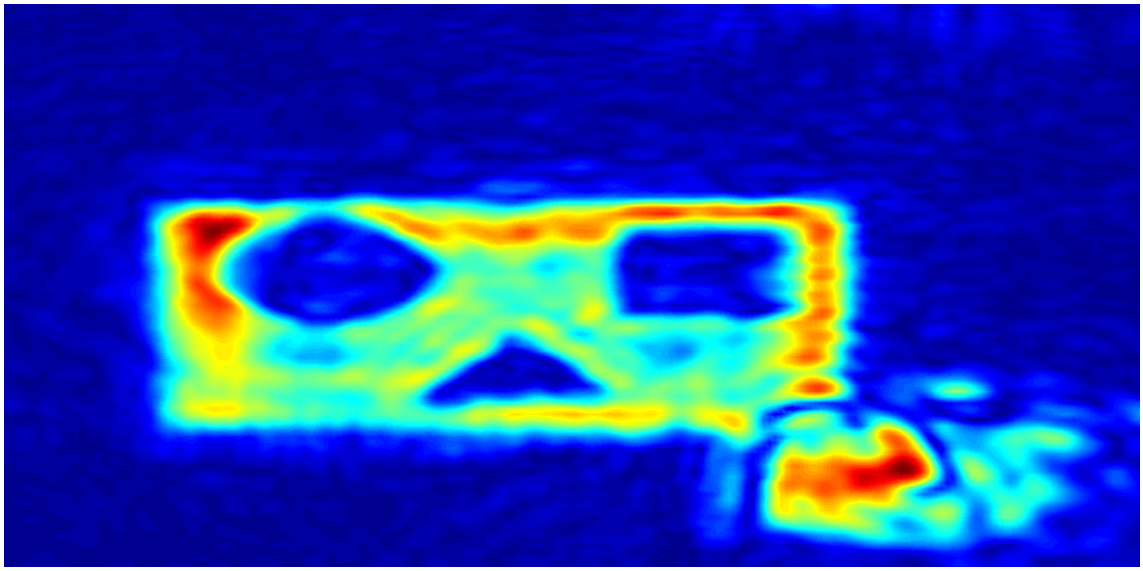


Figure 4.53: SAR image reconstruction.

4.7 Conclusions

This chapter presented the design and construction process of a CATR anechoic chamber, as well as its EM characterization. The characterization in the 1-20 GHz band provided significant insights into the performance and limitations of both the antennas and the chamber. The analysis revealed that the antennas are not well-matched for frequencies below 5 GHz, as showed by the elevated VSWR values and non-linear phase and magnitude responses at lower frequencies. Consequently, the focus of the characterization was adjusted to the 5-20 GHz range. The transmission coefficients, particularly at higher frequencies and greater separation distances, exhibited ripples likely caused by reflections within the chamber, including those from the metallic components of the linear rail actuators. Despite these effects, the phase response remained linear across the frequency range, suggesting that the setup is still reliable within the truncated band. Time-domain analysis further confirmed the presence of internal reflections and multipath components, both from the linear rail actuators and the chamber's structure. Similarly, the characterization in the 60 - 90 GHz frequency band also provided valuable insights into the performance of the chamber at mmWave. The setup's sensitivity to mechanical oscillations and the ripple in transmission coefficients, especially at higher frequencies, also highlighted multipath components and internal reflections within the chamber. The analysis of the transmission coefficients, particularly in the delay domain, revealed the presence of multipath effects and internal reflections, which were most pronounced at specific distances and frequencies. These observations are crucial in order to optimize future measurements and understanding the chamber's behavior and its limitations. Overall, the characterization was successful in identifying key aspects of the chamber, and ultimately, these findings serve as a foundation for future measurements. Subsequent work on the anechoic chamber was performed using the TI radars and the developed 360° radar, presented in section 3.3, which included a radar calibration, a bumper radar characterization and a SAR measurement. The 360° radar calibration ensured precise and repeatable performance by adjusting the range bias and phase discrepancies across the radar sensors. The characterization of bumper polymers provided valuable understanding into the transparency of different materials, confirming that these polymers do not significantly impact radar detection, which is critical for automotive applications. Finally, the SAR imaging measurement demonstrated the capability of high-resolution radar imaging within the anechoic chamber. Together, these experiments illustrate the versatility and importance of the CATR anechoic chamber in radar research and development for automotive applications.

Chapter 5

Conclusions and Future Work

5.1 Summary and Main Conclusions

This work began with a review on automotive radar systems, followed by a display of different state-of-the-art automotive radar systems, with an emphasis on FMCW systems. Furthermore, the fundamental theory and operation behind FMCW radar systems was addressed. Afterwards, the main focus of this work was introduced, a 360° 4D radar prototype, along with its implementation and validation. The architecture behind the 360° 4D radar was presented and discussed, followed by 2 different approaches for data processing and visualization. The development of MATLAB scripts and a user-friendly GUI was integral to the operation and real-time management of the 360° radar, enhancing both the setup and visualization processes. The 360° radar was tested in a controlled environment, i.e. anechoic chamber, with static and moving objects. The practical tests conducted, though revealing some limitations, have demonstrated the radar's capability in detecting and mapping objects in various scenarios outputting a high-resolution point-cloud with an error contained to a few centimeters. While further improvement is needed to address detection inaccuracies and errors in dynamic environments, the 360° radar prototype has shown significant potential for real-world applications. Lastly, a mmWave CATR anechoic chamber was designed and constructed to be used for measurements across both automotive frequency bands, 24 and 77 GHz. To accommodate those, the anechoic chamber was designed taking in consideration the far-field condition at both frequencies, which led to a length of 1.83 m and a width and height of 91.5 cm. Additionally, the chamber includes an automated linear rail system that allows several measurement setups with millimetric precision. Furthermore, its EM characterization was done for both the 1 - 20 GHz and the 60 - 90 GHz frequency bands, offering crucial information about its performance across various frequencies. Being specially designed for frequencies above 45 GHz, the chamber also performed well for frequencies around 20 GHz, which, in addition, allows for tests and measurements using 24 GHz automotive radars. The characterization also highlighted some minor limitations, particularly related to internal reflections/multipath components and phase response. Despite these limitations, the chamber demonstrated reliability within the automotive frequency bands and proved effective for radar calibration, bumper characterization and SAR measurements, which were performed inside of it and delivered good results, as it was demonstrated. Together, these developments highlight significant progress in radar technology and the critical role of the CATR anechoic chamber in advancing radar technology for automotive applications.

5.2 Future Work

5.2.1 Radar

Additional work regarding the 360° 4D radar might include extending the measurements in multiple, and also more complex, scenarios to expand the datasets and also to see how the system behaves in different environments and how well it handles different target's construction materials. Regarding the GUI, it could also be improved by turning it into an executable program, which requires less processing capacity in comparison with MATLAB. On the visual/graphical level it can also be improved, to make it more appealing/with better aesthetics. The version using the raspberry Pi also has some work to do. It might only be necessary to migrate it to another, more powerful, hardware, or doing some more work at the OS level. Another interesting task for the future might be the exploration of radar beamforming, which offers many advantages, such as increased SNR, improved coverage, lower power consumption and many more.

5.2.2 Anechoic chamber

The characterization of the CATR anechoic chamber needs to be expanded. With the available equipment it was only possible to perform the measurements in one rail, covering only the center of the chamber along its length. A full characterization should be performed to ensure that most of the volume is radio-scanned, in order to find the quiet-zones of this chamber. Also, the linear rail step resolution for the 60 - 90 GHz frequency band measurements should be, ideally, less than 0.5 mm in order to fully capture the phase variations properly. The mechanical oscillations in the moving platforms of the linear rails are also a drawback to the precise measurements,which should also be improved.

5.3 Contribution to Literature

The work presented in this dissertation, particularly the validation of the 360° radar detection and the EM characterization in the 5 - 20 GHz band, has contributed to one conference paper and one journal paper:

- **Conference Paper:** S. Viegas, J. R. Reis, T. R. Fernandes and R. F. S. Caldeirinha, "4D MIMO Radar with 360º field of view: a practical validation," 2023 International Wireless Communications and Mobile Computing (IWCMC), Marrakesh, Morocco, 2023, pp. 757-762, doi: 10.1109/IWCMC58020.2023.10182690.
- **Journal Paper:** I. Expósito, J. R. Reis, S. Viegas, R. F. S. Caldeirinha, I. Cuiñas, M. G. Sánchez, "Analysis of Selective Surfaces Characterization Using Free-Space Technique", IEEE Transactions on Antennas and Propagation, 2024. (Under review R4)

5.4 Live Demonstrators

Additionally, the work presented in this dissertation was demonstrated live in the following events:

- **TECH4INNOV:** Technological exhibition of Research and Development (R&D) projects from national entities. Hosted at Europarque in Santa Maria da Feira on the 29th of March of 2023.
- **PAC Open Day:** Final session of PAC project, showcasing the contributions of all the parties involved. Hosted at Simoldes group headquarters in Oliveira de Azeméis on the 23rd of June of 2023.

Bibliography

[1] World Health Organization. “Global Status Report on Road Safety”. In: (2018).

[2] Karel Brookhuis, Dick Waard, and Wiel Janssen. “Behavioural impacts of Advanced Driver Assistance Systems-an overview”. In: *European Journal of Transport and Infrastructure Research* 1 (Jan. 2001). DOI: 10.18757/ejtir.2001.1.3.3667.

[3] James Jeffs. *Automotive Radar 2024-2044: Forecasts, Technologies, Applications*. Tech. rep. IDTechEx, 2023. URL: https://www.idtechex.com/en/research-report/automotive-radar-2024-2044-forecasts-technologies-applications/966.

[4] Marco Galvani. “History and Future of Driver Assistance”. In: *IEEE Instrumentation Measurement Magazine* 22 (Feb. 2019), pp. 11–16. DOI: 10.1109/MIM.2019.8633345.

[5] Wenhao Zong et al. “Architecture Design and Implementation of an Autonomous Vehicle”. In: *IEEE Access* PP (Apr. 2018), pp. 1–1. DOI: 10.1109/ACCESS.2018.2828260.

[6] Seongwook Lee et al. “Human–Vehicle Classification Using Feature-Based Svm in 77-Ghz Automotive Fmcw Radar”. In: *IET Radar, Sonar Navigation* 11 (July 2017). DOI: 10.1049/iet-rsn.2017.0126.

[7] C. C. Chen. “Attenuation of Electromagnetic Radiation by Haze, Fog, Clouds, and Rain”. In: (1975).

[8] Rui Song et al. “Weather Effects on Obstacle Detection for Autonomous Car”. In: (Jan. 2020), pp. 331–341. DOI: 10.5220/0009354503310341.

[9] Keisuke Yoneda et al. “Automated Driving Recognition Technologies for Adverse Weather Conditions”. In: *IATSS Research* 43 (Nov. 2019). DOI: 10.1016/j.iatssr.2019.11.005.

[10] Shizhe Zang et al. “The Impact of Adverse Weather Conditions on Autonomous Vehicles: Examining How Rain, Snow, Fog, and Hail Affect the Performance of a Self-Driving Car”. In: *IEEE Vehicular Technology Magazine* PP (Mar. 2019), pp. 1–1. DOI: 10.1109/MVT.2019.2892497.

[11] Yuxiao Zhang et al. “Perception and Sensing for Autonomous Vehicles under Adverse Weather Conditions: A Survey”. In: *ISPRS Journal of Photogrammetry and Remote Sensing* (2021).

[12] Wolfgang" "Menzel. *"Antennas in Automobile Radar"*. Ed. by Zhi Ning" "Chen. "Springer Singapore", 2021, "1–22". ISBN: "978-981-4560-75-7". DOI: "10.1007/978-981-4560-75-7_96-1". URL: https://doi.org/10.1007/978-981-4560-75-7_96-1.

[13] Christian Waldschmidt, Juergen Hasch, and Wolfgang Menzel. “Automotive Radar — From First Efforts to Future Systems”. In: *IEEE Journal of Microwaves* 1.1 (2021), pp. 135–148. DOI: 10.1109/JMW.2020.3033616.

[14] Holger H. "Meinel and Wolfgang" Bosch. *"Radar Sensors in Cars"*. Ed. by Daniel "Watzenig and Martin" Horn. "Springer International Publishing", 2017, "245–261".

ISBN: "978-3-319-31895-0". DOI: "10.1007/978-3-319-31895-0_10". URL: https://doi.org/10.1007/978-3-319-31895-0_10.

[15] Holger H. Meinel and Juergen Dickmann. "Automotive Radar: From Its Origins to Future Directions". In: *Microwave Journal* (Sept. 2013). URL: https://www.microwavejournal.com/articles/20469-automotive-radar-from-its-origins-to-future-directions.

[16] I. Gresham et al. "A compact manufacturable 76-77-GHz radar module for commercial ACC applications". In: *Microwave Theory and Techniques, IEEE Transactions on* 49 (Feb. 2001), pp. 44–58. DOI: 10.1109/22.899961.

[17] Wolfgang Menzel, Dietmar Pilz, and Ralf Leberer. "A 77 GHz FM/CW radar frontend with a low-profile, low-loss printed antenna". In: *1999 IEEE MTT-S International Microwave Symposium Digest (Cat. No.99CH36282)* 4 (1999), 1485–1488 vol.4. URL: https://api.semanticscholar.org/CorpusID:32528991.

[18] Marc Camiade et al. "Full MMIC millimeter-wave front end for a 76.5 GHz adaptive cruise control car radar". In: *1999 IEEE MTT-S International Microwave Symposium Digest (Cat. No.99CH36282)* 4 (1999), 1489–1492 vol.4. URL: https://api.semanticscholar.org/CorpusID:29656360.

[19] ETSI. *ETSI TR 103 593 - Technical characteristics for radiodetermination equipment for ground based vehicular applications within the frequency range 77 GHz to 81 GHz*. Tech. rep. 2020. URL: https://www.etsi.org/deliver/etsi_tr/103500_103599/103593/01.01.01_60/tr_103593v010101p.pdf.

[20] FCC. *FCC 47 CFR Parts 1, 2, 15, 90, 95 and 97 - Permitting Radar Services in the 76-81 GHz Band*. Tech. rep. 2017. URL: https://www.govinfo.gov/content/pkg/FR-2017-09-20/pdf/2017-18463.pdf.

[21] ECC. *ECC Decision (04)10 - The frequency bands to be designated for the temporary introduction of Automotive Short Range Radars (SRR)*. Tech. rep. 2005. URL: https://docdb.cept.org/download/2788.

[22] ITU. *Recommendation ITU-R M.2057-1 - Systems characteristics of automotive radars operating in the frequency band 76-81 GHz for intelligent transport systems applications*. Tech. rep. 2018. URL: https://www.itu.int/dms_pubrec/itu-r/rec/m/R-REC-M.2057-1-201801-I!!PDF-E.pdf.

[23] Texas Instruments. *Moving from legacy 24 GHz to state-of-the-art 77 GHz radar, Ref. SPRY312*. Tech. rep. 2017. URL: https://www.ti.com/lit/wp/spry312/spry312.pdf?ts=1706309436947&ref_url=https%253A%252F%252Fwww.google.com%252F.

[24] Brett Borden and Margaret Cheney. "Radar imaging". In: *Inverse Problems* 29 (), p. 050301. DOI: 10.1088/0266-5611/29/5/050301.

[25] James A. Scheer Mark A. Richards and William A. Holm. *Principles of Modern Radar: Basic Principles*. Scitech Publishing, 2010. ISBN: 9781891121524. DOI: 10.1049/SBRA021E.

[26] Texas Instruments. *AWR2243 Single-Chip 76- to 81-GHz FMCW Transceiver*. Tech. rep. Texas Instruments, 2020. URL: https://www.ti.com/lit/ds/symlink/awr2243.pdf?ts=1689018968820&ref_url=https%253A%252F%252Fdev.ti.com%252F.

[27] Texas Instruments. *Imaging Radar Using Cascaded mmWave Sensor Reference Design*. Tech. rep. Texas Instruments, 2020. URL: https://www.ti.com/lit/ug/tiduen5a/tiduen5a.pdf?ts=1689076010623&ref_url=https%253A%252F%252Fwww.google.com%252F.

[28] Continental. *ARS430 Technical Overview*. Tech. rep. Continental. URL: https://conti-engineering.com/components/ars430/.

[29] Continental. *ARS408 Technical Overview*. Tech. rep. Continental, 2017. URL: https://conti-engineering.com/wp-content/uploads/2020/02/ARS-408-21_EN_HS-1.pdf.

[30] Smartmicro. *UMRR-11 Type 132 Automotive Sensor Product Information*. Tech. rep. Smartmicro, 2021. URL: https://www.smartmicro.com/fileadmin/media/Downloads/Automotive_Radar/Sensor_Data_Sheets_76-81GHz/UMRR-11_Type_132_Automotive_Data_Sheet.pdf.

[31] Smartmicro. *UMRR-96 Type 153 Automotive Sensor Product Information*. Tech. rep. Smartmicro, 2020. URL: https://www.smartmicro.com/fileadmin/media/Downloads/Automotive_Radar/Sensor_Data_Sheets_76-81GHz/UMRR_Automotive_Type_153_Data_Sheet.pdf.

[32] Ainstein. *mmWave Imaging Radar*. Tech. rep. Ainstein. URL: https://pdf.aeroexpo.online/pdf/ainstein/o-79/187738-21761.html.

[33] Bosch. *Corner Radar*. Tech. rep. Bosch. URL: https://www.bosch-mobility.com/media/global/products-and-services/passenger-cars-and-light-commercial-vehicles/driver-assistance-systems/predictive-emergency-braking-system/corner-radar-sensor/onepager_corner-radar_en_200608.pdf.

[34] Bosch. *Front Radar*. Tech. rep. Bosch. URL: https://www.bosch-mobility.com/media/global/products-and-services/passenger-cars-and-light-commercial-vehicles/driver-assistance-systems/multi-camera-system/front-radar-plus/onepager_front-radar_en_200608.pdf.

[35] Bosch. *Front Radar Premium*. Tech. rep. Bosch. URL: https://www.bosch-mobility.com/media/global/products-and-services/passenger-cars-and-light-commercial-vehicles/driver-assistance-systems/multi-camera-system/front-radar-plus/onepager_front-radar_en-premium.pdf.

[36] Yuwei Cheng et al. "A New Automotive Radar 4D Point Clouds Detector by Using Deep Learning". In: (2021), pp. 8398–8402. DOI: 10.1109/ICASSP39728.2021.9413682.

[37] Jie Bai et al. "Radar Transformer: An Object Classification Network Based on 4D MMW Imaging Radar". In: *Sensors* 21 (June 2021), p. 3854. DOI: 10.3390/s21113854.

[38] Xiangyu Gao et al. "RAMP-CNN: A Novel Neural Network for Enhanced Automotive Radar Object Recognition". In: (Oct. 2020).

[39] Gang Li et al. "Pioneer Study on Near-Range Sensing with 4D MIMO-FMCW Automotive Radars". In: (2019), pp. 1–10. DOI: 10.23919/IRS.2019.8768170.

[40] Dominik Schwarz et al. "System Performance of a 79 GHz High-Resolution 4D Imaging MIMO Radar With 1728 Virtual Channels". In: *IEEE Journal of Microwaves* 2.4 (2022), pp. 637–647. DOI: 10.1109/JMW.2022.3196454.

[41] Vladimir Milovanović. "On fundamental operating principles and range-doppler estimation in monolithic frequency-modulated continuous-wave radar sensors". In: *Facta universitatis - series: Electronics and Energetics* 31 (Jan. 2018), pp. 547–570. DOI: 10.2298/FUEE1804547M.

[42] M.A. Richards. *Fundamentals Of Radar Signal Processing*. McGraw-Hill Education (India) Pvt Limited, 2005. ISBN: 9780070607378. URL: https://books.google.pt/books?id=qizdSv8MEngC.

[43] Ammar. Shehabi. "Radar Detection for Drones". Université de Liège, Liège, Belgique, 2022. URL: https://matheo.uliege.be/handle/2268.2/14447.

[44] Texas Instruments. *AWR1843 Single-Chip 77- to 79-GHz FMCW Radar Sensor*. Tech. rep. Texas Instruments, 2020. URL: https://www.ti.com/lit/ds/symlink/awr1843.pdf?ts=1689084645400&ref_url=https%253A%252F%252Fwww.ti.com%252Fproduct%252FAWR1843.

[45] Jürgen Hasch et al. "Millimeter-Wave Technology for Automotive Radar Sensors in the 77 GHz Frequency Band". In: *IEEE Transactions on Microwave Theory and Techniques* 60.3 (2012), pp. 845–860. DOI: 10.1109/TMTT.2011.2178427.

[46] David Werbunat et al. "OFDM-Based Radar Network Providing Phase Coherent DOA Estimation". In: *IEEE Transactions on Microwave Theory and Techniques* 69.1 (2021), pp. 325–336. DOI: 10.1109/TMTT.2020.3026041.

[47] Texas Instruments. *Mimo Radar - Application Report, Ref. Swra554a*. Tech. rep. 2017. URL: https://www.ti.com/lit/an/swra554a/swra554a.pdf.

[48] Texas Instruments. *xWR1843 Evaluation Module (xWR1843BOOST) Single-Chip mmWave Sensing Solution*. Tech. rep. Texas Instruments, 2020. URL: https://www.ti.com/lit/ug/spruim4b/spruim4b.pdf?ts=1689024943984.

[49] Richard Tanski and Jay Lee. "Optimized Virtual Antenna Array of Wideband Narrow Beam Mimo System for Overlapped Virtual Elements". In: (Aug. 2020), pp. 1–3. DOI: 10.23919/URSIGASS49373.2020.9232368.

[50] Haythem Abdullah et al. "High-Resolution and Large-Detection-Range Virtual Antenna Array for Automotive Radar Applications". In: *Sensors* 21.5 (2021). ISSN: 1424-8220. DOI: 10.3390/s21051702. URL: https://www.mdpi.com/1424-8220/21/5/1702.

[51] Shunqiao Sun, Athina P. Petropulu, and H. Vincent Poor. "MIMO Radar for Advanced Driver-Assistance Systems and Autonomous Driving: Advantages and Challenges". In: *IEEE Signal Processing Magazine* 37.4 (2020), pp. 98–117. DOI: 10.1109/MSP.2020.2978507.

[52] Eunhee Kim, Ilkyu Kim, and Wansik Kim. "Non-Uniform MIMO Array Design for Radar Systems Using Multi-Channel Transceivers". In: *Remote Sensing* 15.1 (2023). ISSN: 2072-4292. DOI: 10.3390/rs15010078. URL: https://www.mdpi.com/2072-4292/15/1/78.

[53] Markus Wintermantel. "Radar system with improved angle formation". 0074621 A1. Mar. 2011. URL: https://patentimages.storage.googleapis.com/bc/7a/2e/bf21ac097928c1/US20110074621A1.pdf.

[54] James F. Searey Stephen W. Alland. "Radar system and method of digital beamforming". 0085800 A1. Apr. 2009. URL: https://patentimages.storage.googleapis.com/a5/c8/85/a72584e74bbd19/US20090085800A1.pdf.

[55] Killian Rambach Michael Schoor Goetz Kuehnle and Benedikt Loesch. "Method for operating a MIMO radar". 9448302 B2. Sept. 2016. URL: https://patentimages.storage.googleapis.com/76/fb/8f/2a1a8499b4f5e9/US9448302.pdf.

[56] Y. Morales. "Proactive Driving Modeling in Blind Intersections Based on Expert Driver Data". In: (June 2017). DOI: 10.1109/IVS.2017.7995830.

[57] Leonardo Santana et al. "A comparative study between PETG and PLA for 3D printing through thermal, chemical and mechanical characterization". In: *Matéria (Rio de Janeiro)* 23.4 (2018), e12267. ISSN: 1517-7076. DOI: 10.1590/S1517-707620180004.0601. URL: https://doi.org/10.1590/S1517-707620180004.0601.

[58] David W." "Wragg. *"A Dictionary of Aviation"*. "F. Fell Publishers, New York", 1974, p. 220. ISBN: "9780811902366".

[59] H. U. R. Mohammed C. Kumar and G. Peake. *mmWave Radar Radome Design Guide, Ref. SWRA705*. Tech. rep. Texas Instruments, 2021. URL: https://www.ti.com/lit/an/swra705/swra705.pdf?ts=1707555080498.

[60] Noah Gregory. "Measuring the Electrical Properties of 3D Printed Plastics in the W-band". University of Arkansas, Fayetteville, 2022. URL: https://scholarworks.uark.edu/eleguht/85/.

[61] "Lauri Kasanen". ""Into the Core: A look at Tiny Core Linux"". In: (2010), p. 164.

[62] Pedro Pinho, Hugo Santos, and Henrique Salgado. "Design of an Anechoic Chamber for W-Band and mmWave". In: *Electronics* 9 (May 2020), p. 804. DOI: 10.3390/electronics9050804.

[63] Emerson Cuming. *WAVASORB VHP - Advanced Broadband Pyramidal Absorber*. Tech. rep. Emerson Cuming Anechoic Chambers, 2022. URL: https://www.ecanechoicchambers.com/pdf/WAVASORB%20-%20VHP.pdf.

[64] Emerson Cuming. *WAVASORB AN - Laminated Broadband Flexible Flat Foam Absorber*. Tech. rep. Emerson Cuming Anechoic Chambers, 2022. URL: https://www.ecanechoicchambers.com/pdf/WAVASORB%20-%20AN.pdf.

[65] Leland H. Hemming. *Electromagnetic Anechoic Chambers : A Fundamental Design and Specification Guide*. IEEE Press ; Wiley Interscience, Piscataway, NJ, New York, 2002. URL: https://worldcat.org/title/557451433.

[66] N. M. Alam Chowdhury et al. "Low cost indoor environment for antenna measurement". In: (2008), pp. 001353–001356. DOI: 10.1109/CCECE.2008.4564761.

[67] Vicente Rodriguez. "Basic Rules for Indoor Anechoic Chamber Design [Measurements Corner]". In: *IEEE Antennas and Propagation Magazine* 58.6 (2016), pp. 82–93. DOI: 10.1109/MAP.2016.2609821.

[68] Microchip. *ATMEGA328P datasheet*. Tech. rep. Microchip, 2015. URL: https://ww1.microchip.com/downloads/en/DeviceDoc/Atmel-7810-Automotive-Microcontrollers-ATmega328P_Datasheet.pdf.

[69] Stepperonline. *DM556T datasheet*. Tech. rep. Stepperonline, 2017. URL: https://www.omc-stepperonline.com/download/DM556T.pdf.

[70] Stepperonline. *Nema 23 datasheet*. Tech. rep. Stepperonline, 2017. URL: https://www.omc-stepperonline.com/download/23HE30-2804S.pdf.

[71] Meanwell. *LRS-350-24 datasheet*. Tech. rep. Meanwell, 2023. URL: https://www.meanwell.com/Upload/PDF/LRS-350/LRS-350-SPEC.PDF.

[72] J. Appel-Hansen. "Reflectivity level of radio anechoic chambers". In: *IEEE Transactions on Antennas and Propagation* 21.4 (1973), pp. 490–498. DOI: 10.1109/TAP.1973.1140524.

[73] Carl W. Sirles et al. *Anechoic chamber performance characterization using Spherical Near-Field Imaging techniques*. 2009, pp. 1734–1738.

[74] Copper Mountain Technologies. *C4420 datasheet*. Tech. rep. Copper Mountain Technologies, 2022. URL: https://coppermountaintech.com/wp-content/uploads/2022/10/CMT21-DATA-SHEET_COBALT-20_FA.pdf.

[75] RFSpin. *QRH0140 datasheet*. Tech. rep. RFSpin, 2021. URL: https://www.rfspin.com/wp-content/uploads/2021/06/QRH0140-%E2%80%93-RF-SPIN.pdf.

[76] Copper Mountain Technologies. *CobaltFx-12 datasheet*. Tech. rep. Copper Mountain Technologies, 2018. URL: https://coppermountaintech.com/wp-content/uploads/2023/06/CobaltFx-FEV-Abbreviated-Specifications.pdf.

[77] Flann microwave. *MD249-AA datasheet*. Tech. rep. Flann microwave, 2022. URL: https://flann.com/wp-content/uploads/2022/08/MD249-Datasheet-Draft-No-inc-1.pdf.

[78] Texas Instruments. *Self-Calibration in TI's mmWave Radar Devices*. Tech. rep. Texas Instruments, 2018. URL: https://www.ti.com/lit/an/spracf4c/spracf4c.pdf?ts=1698014462964&ref_url=https%253A%252F%252Fwww.google.com%252F#:~:text=Calibration%20ensures%20that%20the%20performance,the%20detection%20of%20potential%20failures..

[79] Academisch Proefschrift et al. "Aircraft Recognition from Features Extracted from Measured and Simulated Radar Range Profiles". In: (Nov. 2003).

[80] Shahzad Gishkori et al. "Imaging for a Forward Scanning Automotive Synthetic Aperture Radar". In: *IEEE Transactions on Aerospace and Electronic Systems* 55.3 (2019), pp. 1420–1434. DOI: 10.1109/TAES.2018.2871436.

[81] Reinhard Feger, Andreas Haderer, and Andreas Stelzer. "Experimental verification of a 77-GHz synthetic aperture radar system for automotive applications". In: (2017), pp. 111–114. DOI: 10.1109/ICMIM.2017.7918869.

[82] Florian Fembacher et al. "Real-Time Synthetic Aperture Radar for Automotive Embedded Systems". In: (2018), pp. 517–520. DOI: 10.23919/EuRAD.2018.8546620.

[83] Thomas Gisder, Marc-Michael Meinecke, and Erwin Biebl. "Synthetic Aperture Radar Towards Automotive Applications". In: (2019), pp. 1–10. DOI: 10.23919/IRS.2019.8768173.

[84] K. Tomiyasu. "Tutorial review of synthetic-aperture radar (SAR) with applications to imaging of the ocean surface". In: *Proceedings of the IEEE* 66.5 (1978), pp. 563–583. DOI: 10.1109/PROC.1978.10961.

[85] Curlander JC McDonough RN. *Synthetic Aperture Radar : Systems and Signal Processing*. J. Wiley, New York", 1991.

[86] C. Oliver and S. Quegan. *Understanding Synthetic Aperture Radar Images*. EngineeringPro collection. SciTech Publ., 2004. ISBN: 9781891121319. URL: https://books.google.pt/books?id=IeGKe40S77AC.

[87] R.A. Ryerson et al. *Manual of Remote Sensing: Principles and applications of imaging radar*. Manual of Remote Sensing vol. 1-6. J. Wiley, 1998. ISBN: 9780471294061. URL: https://books.google.pt/books?id=E9AsAQAAMAAJ.

[88] G. Franceschetti and Riccardo Lanari. *Synthetic Aperture Radar Processing*. Feb. 2018, pp. 1–307. ISBN: 9780203737484. DOI: 10.1201/9780203737484.

[89] Martin Kirscht and Carsten Rinke. "3D Reconstruction of Buildings and Vegetation from Synthetic Aperture Radar (SAR) Images". In: (1998). URL: https://api.semanticscholar.org/CorpusID:14564803.

[90] Alberto Moreira et al. "A tutorial on synthetic aperture radar". In: *IEEE Geoscience and Remote Sensing Magazine* 1.1 (2013), pp. 6–43. DOI: 10.1109/MGRS.2013.2248301.

[91] Muhammet Yanik, Dan Wang, and Murat Torlak. "Development and Demonstration of MIMO-SAR mmWave Imaging Testbeds". In: *IEEE Access* 8 (July 2020), pp. 126019–126038. DOI: 10.1109/ACCESS.2020.3007877.

[92] Murat Torlak Muhammet Emin Yanik. *SAR Imaging Tutorial*. Tech. rep. The University of Texas at Dallas, 2018. URL: https://sigport.org/sites/default/files/docs/SAR_Imaging_Tutorial_0.pdf.

Appendix A

Radar Configuration Commands

This section presents in finer detail each command used during the radar configuration.

- **sensorStop** - Stops the sensor. If the sensor is running, it will stop the mmWave front end and the processing chain;
- **flushCfg** - This command flushes the old configuration and provide a new one. It should be issued after 'sensorStop' command;
- **dfeDataOutputMode** - This command configure the mode of frame/chirp operation. Set to 1 for frame based chirps (default/legacy frame), 2 for continuous chirping and 3 for advanced frame configuration;
- **channelCfg** - The values in this command configure the channel message to RadarSS and datapath. The order of appearance and description of the values is as following:
  1. rxChannelEn - Number of RX antennas to use. For 4 antennas it is 0x1111b = 15;
  2. txChannelEn - Number of TX antennas to use. For 3 antennas it is 0x111b = 7;
  3. cascading - It is only applicable when the system uses several radar-on-chip, otherwise it is set to 0;
- **adcCfg** - The values in this command configure the ADC message to RadarSS and datapath. The order of appearance and description of the values is as following:
  1. numADCBits - Number of ADC bits to use. Set to 0 for 12 bits, 1 for 14 bits and 2 for 16 bits;
  2. adcOuputFmt - Output format of the ADC. Set to 0 for real, 1 for complex 1x (image band filtered) and 2 for complex 2x (image band visible);
- **adcbufCfg** - The values in this command configure the ADCBuf hardware. The order of appearance and description of the values is as following:
  1. subFrameIdx - It is used when working in advanced frame mode. To apply the same configuration to all subframes set to -1, otherwise set to the intended subframe number;
  2. adcOuputFmt - Output format of the ADCBuf. Set to 0 for complex and 1 for real;

3. sampleSwap - In-Phase (I) and Quadrature (Q) swap selection. Set to 0 for I in Least Significant Bit (LSB) and Q in Most Significant Bit (MSB) and 1 for Q in LSB and I in MSB;
4. chanInterleave - ADCBuf channel interleave configuration. Set to 0 for interleaved and 1 for non-interleaved;
5. chirpThreshold - Chirp threshold configuration used for ADCBuf buffer to trigger ping/pong buffer switch. Set 1 for xWR18xx,xWR64xx and xWR68xx radar-on-chip and 0-8 for xWR16xx radar-on-chip;

- **lowPower** - Enables the low power ADC mode. First value set to 0 (don't care). Second value is the ADC mode, set to 0 for regular ADC mode and 1 for Low power ADC mode;
- **profileCfg** - The values in this command configure the profile message to RadarSS and datapath. The order of appearance and description of the values is as following:
  1. profileId - Profile identifier. Set to 1 for default/legacy frame mode and 3 for advanced frame mode;
  2. startFreq - Chirp start frequency in GHz (float values allowed);
  3. idleTime - Idle time in μs (float values allowed);
  4. adcStartTime - ADC start time in μs (float values allowed);
  5. rampEndTime - Ramp end time in μs (float values allowed);
  6. txOutPower - TX output power back-off code for antennas. Set to 0 for general purpose applications, otherwise consult the information provided by TI in their official radar-on-chip documentation;
  7. txPhaseShifter - Phase shifter for TX antennas. Set to 0 for general purpose applications, otherwise consult the information provided by TI in their official radar-on-chip documentation;
  8. freqSlopeConst - Frequency slope for the chirp in MHz/μs (float values allowed);
  9. txStartTime - TX start time in μs (float values allowed);
  10. numAdcSamples - Number of ADC samples collected during the ADC sampling time;
  11. digOutSampleRate - ADC sampling frequency in ksps (kilosamples per second);
  12. hpfCornerFreq1 - Cutoff frequency of the first high pass filter. Set to 0 for 175 kHz, 1 for 235 kHz, 2 for 350 kHz and 3 for 700 kHz;
  13. hpfCornerFreq2 - Cutoff frequency of the second high pass filter. Set to 0 for 350 kHz, 1 for 700 kHz, 2 for 1.4 MHz and 3 for 2.8 MHz;
  14. rxGain - RX chain and RF gain target in dB;
- **chirpCfg** - The values in this command configure the chirp message to RadarSS and datapath. The order of appearance and description of the values is as following:
  1. chirp start index;

2. chirp end index;
3. profile identifier;
4. start frequency variation in Hz (float values allowed);
5. frequency slope variation in kHz/μs (float values allowed);
6. idle time variation in μs (float values allowed);
7. ADC start time variation in μs (float values allowed);
8. TX antenna enable mask;

- **frameCfg** - The values in this command configure the frame message to RadarSS and datapath. The order of appearance and description of the values is as following:
  1. chirp start index (valid range is 0-511);
  2. chirp end index (valid range is chirp start index-511);
  3. number of loops (valid range is 1 to 255);
  4. number of frames (valid range is 0 - 65535, 0 meaning infinite);
  5. frame periodicity in *m*s (float values allowed);
  6. trigger select. Set to 1 for software trigger and 2 for hardware trigger;
  7. frame trigger delay in *m*s (float values allowed);
- **guiMonitor** - This command allows the user to choose which data is sent from the radar. The order of appearance and description of the values is as following:
  1. subFrameIdx;
  2. detected objects. Set to 0 to disable, 1 to enable the export of point cloud (x, y, z, Doppler) and side info (SNR, noise) and 2 to enable only the export of point cloud (x, y, z, Doppler);
  3. log magnitude range profile. Set to 0 to disable and 1 to enable the export of log magnitude range profile at zero Doppler;
  4. noise profile. Set to 0 to disable and 1 to enable the export of log magnitude noise profile;
  5. range-azimuth and range-azimuth-elevation heatmaps. Set to 0 to disable and 1 to enable the export of zero Doppler radar cube matrix, all range bins, all azimuth virtual antennas to calculate and display azimuth heatmap;
  6. range-Doppler heatmap. Set to 0 to disable and 1 to enable the export of the whole detection matrix;
  7. statistics (CPU load, margins, device temperature readings, etc). Set to 0 to disable and 1 to enable the export of stats data;
- **cfarCfg** - The values in this command are used to configure the CFAR in range or Doppler direction and to choose the CFAR averaging mode. The order of appearance and description of the values is as following:
  1. subFrameIdx;

2. procDirection - Processing direction. Seto to 0 for CFAR detection in range direction and 1 for CFAR detection in Doppler direction;
3. mode - CFAR averaging mode. Set to 0 for CFAR-CA (cell averaging), 1 for CFAR-CAGO (cell averaging greatest of) and 2 for CFAR-CASO (cell averaging smallest of);
4. noiseWin - Noise averaging window length;
5. guardLen - One sided guard length in samples;
6. divShift - Cumulative noise sum divisor expressed as a shift;
7. cyclic mode or wrapped around mode. Set to 0 to disable and 1 to enable;
8. threshold scale in dB using float representation;
9. peak grouping. Set to 0 to disable and 1 to enable;

- **multiObjBeamForming** - When enabled, this feature allows the radar to separate reflections from multiple objects originating from the same range/Doppler detection. The order of appearance and description of the values is as following:
  1. subFrameIdx;
  2. feature enabled. Set to 0 to disable and 1 to enable;
  3. threshold scale for the second peak detection in azimuth FFT output (valid range is 0-1);
- **calibDcRangeSig** - When this feature is enabled, the antenna coupling signature, that dominates the range bins close to the radar (located around DC), is estimated during the first N chirps and then it is subtracted during the subsequent chirps. The order of appearance and description of the values is as following:
  1. subFrameIdx;
  2. enable dc removal using first few chirps. Set to 0 to disable and 1 to enable;
  3. negativeBinIdx - Removes DC from the farthest range bins;
  4. positiveBinIdx - Removes DC from the closest range bins;
  5. numAvg - Number of chirps to average to collect DC signature;
- **clutterRemoval** - Enables the implementation of a static clutter removal algorithm that subtracts from the samples the mean value of the input samples to the 2D-FFT;
- **compRangeBiasAndRxChanPhase** - Command for datapath to compensate for bias in the range estimation and receive channel gain and phase imperfections. The order of appearance and description of the values is as following:
  1. rangeBias - Compensation for range estimation bias in meters;
  2. targetDistance - Set of complex value pairs (I and Q) representing compensation for virtual RX channel phase bias. The number of pairs depends on the number of virtual antennas a radar system has. In the case of AWR1843BOOST is 12 virtual antennas, thus 12 pairs of complex values;

- **measureRangeBiasAndRxChanPhase** - Command for datapath to enable the measurement of the range bias and receive channel gain and phase imperfections. The order of appearance and description of the values is as following:
  1. enabled - Set to 0 to disable and 1 to enable;
  2. targetDistance - Distance in meters where a strong reflector is located to be used as test object for measurement;
  3. searchWin - Distance in meters of the search window around 'targetDistance', where the peak will be searched;
- **aoaFovCfg** - Command for datapath to filter out detected points outside the specified range in azimuth or elevation plane. The order of appearance and description of the values is as following:
  1. subFrameIdx;
  2. minAzimuthDeg - Minimum angle in the azimuth plane (in degrees);
  3. maxAzimuthDeg - Maximum angle in the azimuth plane (in degrees);
  4. minElevationDeg - Minimum angle in the elevation plane (in degrees);
  5. maxElevationDeg - Maximum angle in the elevation plane (in degrees);
- **cfarFovCfg** - Command for datapath to filter out detected points outside the specified limits in the range or Doppler direction. The order of appearance and description of the values is as following:
  1. subFrameIdx;
  2. procDirection - Set to 0 for point filtering in range direction and 1 for point filtering in Doppler direction;
  3. minimum limits for the range or Doppler. Set in m for range direction and m/s for Doppler direction;
  4. maximum limits for the range or Doppler. Set in m for range direction and m/s for Doppler direction;
- **extendedMaxVelocity** - Enables the implementation of a simple technique for velocity disambiguation. It corrects target velocities up to (2*v_{max});
- **CQRxSatMonitor** - Rx Saturation Monitoring configuration message forChirp quality to RadarSS and datapath;
- **CQSigImgMonitor** - Signal and image band energy Monitoring configuration message for Chirp quality to RadarSS and datapath;
- **analogMonitor** - Enables the supported monitoring features, CQRxSatMonitor and CQSigImgMonitor;
- **lvdsStreamCfg** - Enables the streaming of various data streams over LVDS lanes;
- **calibData** - Provides user to either save the boot time RF calibration performed by the RadarSS onto the FLASH or to restore the previously saved RF calibration data from the FLASH and instruct RadarSS to not re-perform the boot-time calibration;

- **sensorStart** - Starts the sensor. This function triggers the transmission of the frames as per the frame and chirp configuration. It also sends the configuration to the mmWave front end and processing chain.